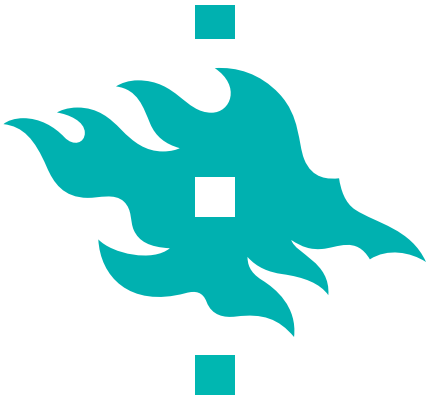

DISSERTATIONES SCHOLAE DOCTORALIS AD SANITATEM INVESTIGANDAM
UNIVERSITATIS HELSINKIENSIS

PATRÍCIA ISABEL TAVARES FIGUEIREDO

DEVELOPMENT OF LIGNIN-BASED NANOPARTICLES FOR CANCER THERAPY

DIVISION OF PHARMACEUTICAL CHEMISTRY AND TECHNOLOGY
FACULTY OF PHARMACY
DOCTORAL PROGRAMME IN DRUG RESEARCH
UNIVERSITY OF HELSINKI

Division of Pharmaceutical Chemistry and Technology
Faculty of Pharmacy
University of Helsinki
Finland

Development of Lignin-based Nanoparticles for Cancer Therapy

by

Patrícia Figueiredo

ACADEMIC DISSERTATION

To be presented, with the permission of the Faculty of Pharmacy of the University of Helsinki, for public examination in room P674 at Porthania (Yliopistonkatu 3, Helsinki) on July 24th, 2020, at 12.00 noon.

Helsinki 2020

Main supervisor Professor Dr. Hélder A. Santos
Drug Research Program
Division of Pharmaceutical Chemistry and Technology
Faculty of Pharmacy
and
Helsinki Institute of Life Science (HiLIFE)
University of Helsinki
Finland

Co-supervisors Professor and Dean Dr. Jouni Hirvonen
Drug Research Program
Division of Pharmaceutical Chemistry and Technology
Faculty of Pharmacy
University of Helsinki
Finland

Associate Professor Dr. Mauri A. Kostiainen
Biohybrid Materials Group
Department of Biotechnology and Chemical Technology
Aalto University
Finland

Reviewers Associate Professor Nunzio Denora
Department of Pharmacy – Drug Sciences
University of Bari Aldo Moro
Italy

Dr. José das Neves
Instituto de Investigação e Inovação em Saúde (i3S)
University of Porto
Portugal

Opponent Associate Professor Manuel Arruebo
Department of Chemical Engineering
Aragon Institute of Nanoscience (INA)
University of Zaragoza
Spain

ISBN 978-951-51-6093-5 (paperback)
ISBN 978-951-51-6094-2 (PDF)
ISSN 2342-3161 (print), 2342-317X (online)

Helsinki University Printing House
Helsinki 2020

The faculty of Pharmacy uses the Urkund system (plagiarism recognition) to examine all doctoral dissertations.

Abstract

Figueiredo P., 2020. **Development of Lignin-based Nanoparticles for Cancer Therapy**

Lignin is part of the lignocellulosic biomass and represents the second most abundant biopolymer after cellulose. However, only about 2% of the annually isolated lignin is used for low-value applications, mainly due to its complex structure. The fabrication of lignin nanoparticles offers a structural and morphological control of the lignin polymer, which enables lignin to be used for high-value products in biomedical applications like drug delivery and tissue engineering. Therefore, the main aim of this thesis was to exploit the potential of the under-investigated lignin-based nanoparticles as vehicles to deliver different therapeutic compounds for improved cancer therapy. Although multiple treatment options are available to treat cancer diseases, they still represent illnesses with very high incidence and mortality worldwide. Nanotechnology has opened doors to improve the limitations of current therapeutic modalities, such as chemotherapy or administration of immunomodulatory agents, by improving the solubility, stability and circulating half-life of the therapeutics, and by minimizing the systemic side effects. Firstly, different lignin-based nanoparticles were prepared and characterized, and their cytocompatibility investigated towards several cell lines. The ability of lignin nanoparticles to load different chemotherapeutic compounds was assessed, and drug release profiles were evaluated in two different buffers (pH 5.5 and 7.4). Secondly, after a carboxylation reaction of the original lignin polymer, the carboxylated lignin nanoparticles were surface modified with a polymer/peptide, as a proof-of-concept of the nanoparticles' functionalization. The release profile of a poorly-water soluble cytotoxic compound (benzazulene) from the lignin nanoparticles was evaluated, and the *in vitro* antiproliferative effect investigated against several cell lines. Next, lignin polymers with different degrees of carboxylation were prepared in order to investigate the long-term stability of the resulting lignin nanoparticles at physiological conditions. After finding the optimal conditions in terms of stability, the lignin nanoparticles were further functionalized with a cell-penetrating peptide, and the cellular interactions of the resulting nanosystem were evaluated and compared with internalizing arginine-glycine-aspartic acid peptide-functionalized lignin nanoparticles, using two- and three-dimensional cell culture models. Finally, the lignin nanoparticles were loaded with resiquimod, an agonist of the toll-like receptors 7 and 8 that can induce the re-education of M2 to M1-like macrophages, and further functionalized with a peptide that targets the mannose receptor expressed by the M2 macrophages. Afterwards, the homing ability of these nanoparticles was investigated *in vivo*, using an orthotopic 4T1 triple-negative breast cancer model. The therapeutic effect of these nanosystems was studied in combination with a chemotherapeutic compound (vinblastine), and the immunological profile of the cells isolated from the tumors was compared. Overall, this thesis provides new insights on the use of lignin polymer as a novel starting material to develop lignin-based nanocarriers, in particular for cancer therapeutics.

Acknowledgements

And now comes the time and place to thank everyone that contributed to this incredible PhD adventure, in which I encountered plenty of failures and problems, along with some successes. I am sure that the outcome of these beautiful journey compensated the white hairs I got during the last four years of such learning process.

First of all, I acknowledge the Doctoral Program in Drug Research of the University of Helsinki for allowing me to pursue my doctoral studies at the Division of Pharmaceutical Chemistry and Technology, Faculty of Pharmacy. I also acknowledge the funding from the Finnish Cultural Foundation that was crucial to conclude this work, and also other funding sources that supported this work, such as the Orion Research Foundation and the NordForsk for the Nordic University Hub project.

I am deeply thankful to my opponent, Prof. Manuel Arruebo, who accepted the invitation, and I am looking forward to the (remote) discussion.

I would also like to thank the pre-examiners, Prof. Nunzio Denora and Dr. José das Neves, who revised this work and provided constructive comments and suggestions to improve this thesis.

I am extremely grateful to my supervisor Prof. Hélder Santos for accepting me to join his group initially for a period of 7 months, which turned out to be 5 years. Many thanks for the opportunity to start my PhD studies and for your constant support and guidance. I really admire your ambition and passion for doing great science, and also your capacity to handle million things at same time, while answering to emails after 5 minutes.

I also thank Prof. Jouni Hirvonen for your support during this journey, in particular for sending the recommendation letters for my grant applications, and also for your scientific input in this thesis and related manuscripts.

I would like to thank Prof. Mauri Kostiainen, who contributed with his constructive comments and suggestions in all the manuscripts. I extend my gratitude to Dr. Kalle Lintinen, who was the lignin “dealer”, for all the discussions when I was full of problems with lignin.

I am also thankful to Prof. Tambet Teesalu for allowing me to visit his research group at University of Tartu, and perform the animal experiments for the last manuscript. This was a very short but intensive research visit, in which I had the opportunity to learn a lot of different techniques. I extend my gratitude to Dr. Pablo Scodeller for the guidance and fruitful discussions during the last months (one bottle of Porto wine is not enough to thank you). I also want to acknowledge Anni Lepland for the hard work on finalizing the last experiments to answer the reviewers’ comments.

Then I would like to thank all the members of Santos’ Lab, in particular to Alexandra Correia, Dr. Bárbara Herranz-Blanco, Eloy Ginestar, Dr. Flavia Fontana, João Pedro Martins, Dr. Mohammad-Ali Shahbazi, Dr. Mónica Ferreira, Dr. Neha Shrestha, Dr. Patrick Almeida, Dr. Tomás Ramos, Dr. Vimalkumar Balasubramanian and Dr. Wei Li, for their help when I arrived to Finland and for providing the best working environment and sharing their knowledge. I would like to extend my gratitude to my other colleagues and friends Agne, Antti, Ariella, Caramelo (what is your name?), Cheng, Francesca, Gabriela, Giorgia, Giulia, Giuseppina, Ilaria, Jiachen (aka Che-che), Mattia, Marlene, Nazanin, Palminha, Serena, Shiqi, Sofia, Tiago, Voitto, Zehua, and many others. You guys made all these years in Finland much more smooth. Thank you for the lunches, the “productive” coffee breaks, funny dinners, billiard games, and many other good memories! Even though most of you are not here anymore, you certainly got a place in my heart, and I will never forget you. Alexandra, chefinha, thanks for your guidance during the

first months and for your friendship, even after you have waited for me one hour to have lunch when I got lost in my first day. Giulinha, you are such an amazing person, very hard worker and super intelligent, you should believe more in yourself. Grazie fofinha for all the good (and less good) moments we spent together! Zizi (Zehua) and Flavia, I will never forget your advices last Autumn, when I saw two years of work going to the waste bin. Your positive attitude and encouragement made me see “the light in the end of the tunnel”. 謝謝! Grazie mille! Jiachen, meu chinesinho, thanks for being a good friend, for listening me and for your motivating words during the last year. See you again soon! Many thanks to Antti, the official translator in Santos’ Lab, for the hard task to translate this abstract. During this project, I had the opportunity to supervise two master students who helped me a lot in many different ways. Cláudio, many thanks for the hours you spent in front of Zetasizer doing those stability tests (your favorite ones, I know!), while I was attending courses. Mattia, you came to help me in two different times of our lives, and your wise advices and suggestions were always pertinent. We finally manage to conclude our work after these years! Thanks for your friendship, and hopefully we don’t need to launch our “planting potato” business!

I also want to mention here some people I had the opportunity to meet, which were very important to lower down my insanity levels. Or maybe not! Joana, I want to thank you for being there every time I needed to speak out something. You have been always there to listen me. Inês “Patience”, you are the best host we could have in Porto. Thanks for all the funny adventures we have every time we meet. I can’t wait for the next (now, more than ever before!). Chacha, Oxy, we started by collaborating on some animal experiments, which unfortunately did not go well. I am glad that you are still around despite our working collaboration failure. Thanks for being such a crazy friend, because being normal is boring!

Now I want to extend my deepest gratitude to my Portuguese friends that I had the privilege to meet in different stages of my life. To my roommates from the students’ residence, in particular to Sandra, Marina, Flor, Inês and Lena (out of 22!), for all those dinners in the iron tables during those 6 years. I just noticed how lucky we were for sharing the balcony with the best view in Porto, over Douro River, where we had our guitar and karaoke sessions. RUCAII forever! To my friends from masters, as Sacaninhas da presidente, in particular to Bela, Chica, Ro and Ju. Meeting you eight years ago was one of the best things that happened to me. Supercalifragilisticexpialidocious is not enough to describe the moments we had during those two years in Porto. We are now in different parts of Europe, but I am glad we could manage to meet up in person once in a while, like in Amsterdam, London, Bali, or even Matosinhos beach! I really hope we can reschedule the next one soon. I am deeply thankful to my lifelong friends Danielas, Flávia and Sónia for being always there since kindergarten, and for the uncountable and amazing moments we had so far (#énoismigas!).

Finally, I want to deeply thank my family for the constant support and unconditional love since I can remember. Mãe, Pai, não tenho palavras para vos agredecer tudo o que fizeram por mim ao longo da minha vida. Obrigada pelos valores e a educacão que recebi, e que fez de mim o que sou hoje. Maninha Sara, é com muito orgulho que tenho acompanhado o teu crescimento (a todos os níveis). Sabes que podes continuar a contar comigo para tudo. Agradeço também aos meu avós, em particular á minha avó Maria(zinha), pelo exemplo de garra e determinaçao para ultrapassar todos os difíceis obstáculos que a vida lhe colocou.

Helsinki, July 2020

Patrícia Figueiredo

“*Stay hungry. Stay foolish.”*

-Steve Jobs

“You learn more from failure than from success. Don’t let it stop you. Failure builds character.”

-Unknown

Table of contents

List of original publications

This thesis is based on the following publications, which are referred to in the text by their respective roman numerals (**I-IV**).

I **Figueiredo P.**, Lintinen K., Kiriazis A., Hynninen V., Liu Z., Bauleth-Ramos T., Rahikkala A., Correia A., Kohout T., Sarmento B., Yli-Kauhaluoma J., Hirvonen J., Ikkala O., Kostiainen M.A., Santos H.A., *In vitro* evaluation of biodegradable lignin-based nanoparticles for drug delivery and enhanced antiproliferation effect in cancer cells, Biomaterials, 2017, 121, 97–108.

II **Figueiredo P.**, Ferro C., Kemell M., Liu Z., Kiriazis A., Lintinen K., Florindo H.F., Yli-Kauhaluoma J., Hirvonen J., Kostiainen M.A., Santos H.A., Functionalization of carboxylated lignin nanoparticles for targeted and pH-responsive delivery of anticancer drugs, Nanomedicine (*Lond.*), 2017, 12(21), 2581–2596.

III **Figueiredo P.**, Sipponen M.H., Lintinen K., Correia A., Kiriazis A., Yli-Kauhaluoma J., Österberg M., George A., Hirvonen J., Kostiainen M.A., Santos H.A., Preparation and characterization of dentin phosphophoryn-derived peptide-functionalized lignin nanoparticles for enhanced cellular uptake, Small, 2019, 15(24), 1901427.

IV **Figueiredo P.**, Lepland A., Scodeller P., Fontana F., Torrieri G., Tiboni M., Shahbazi M.-A., Casettari L., Hirvonen J., Kostiainen M. A., Teesalu T., Santos H. A., Peptide-guided resiquimod-loaded lignin nanoparticles convert tumor-associated macrophages from M2 to M1 phenotype for enhanced chemotherapy (submitted).

The publications are referred to in the text by their respective roman numerals (**I-IV**). The papers are reprinted with kind permission from Elsevier B.V. (**I**), Future Science Group (**II**) and John Wiley & Sons, Inc (**III**).

Abbreviations and symbols

ACK	Ammonium-chloride-potassium
APCs	Antigen-presenting cells
ATR	Attenuated total reflectance
BMDMs	Bone marrow derived macrophages
BSA	Bovine serum albumin
BZL	1-methyl-8-(propan-2-yl)-4-(trifluoromethyl)-3*H*-benzo[*cd*]azulen-3-one (Benzazulene)
CAP	Capecitabine
CD	Cluster of differentiation
CLPs	Colloidal lignin particles
CPP	Cell-penetrating peptide
CO_2	Carbon dioxide
CTLs	Cytotoxic T cells
CTLA-4	Cytotoxic T-lymphocyte–associated antigen 4
DAPI	4’,6-Diamidino-2-phenylindole
DCF	2’,7’-Dichlorofluorescein
$DCFH_2$-DA	2’,7’-Dichlorodihydrofluorescein diacetate
DiA	4-[4-(Dihexadecylamino)styryl]-N-methylpyridinium iodide
DLS	Dynamic light scattering
DMAP	4-Dimethylaminopyridine
DMEM	Dulbecco's Modified Eagle’s Medium
DMF	Dimethylformamide
DSS	Dentin phosphophoryn-derived peptide
EDC	1-Ethyl-3-(3-dimethylaminopropyl)carbodiimide
EDTA	Ethylenediamine tetraacetic acid
EE	Encapsulation efficiency
ELS	Electrophoretic light scattering
EPR	Enhanced permeation and retention
EtOH	Ethanol
FAM	5(6)-Carboxyfluorescein
Fe	Iron
Fe-LNPs	Iron(III)-complexed lignin nanoparticles
Fe_3O_4 NPs	Iron oxide nanoparticles
Fe_3O_4-LNPs	Iron oxide-infused lignin nanoparticles
FTIR	Fourier-transform infrared
HBSS	Hanks’ balanced salt solution
HEPES	4-(2-Hydroxyethyl)-1-piperazineethanesulfonic acid
HIFBS	Heat inactivated fetal bovine serum
HPLC	High-pressure liquid chromatography
H_2O_2	Hydrogen peroxide
IFN-γ	Interferon gama
IL	Interleukin
iNOS	inducible nitric oxide synthase
iRGD	Internalizing arginine-glycine-aspartic acid peptide
LD	Loading degree
LPS	Lipopolysaccharides

LNPs	Lignin nanoparticles
LNPs-P-FAM	LNPs-PEG-FAM
LNPs-P-F-mUNO	LNPs-PEG-FAM-mUNO
M-CSF	Macrophage colony-stimulating factor
MES	2-(*N*-Morpholino)ethanesulfonic acid
MPS	Mononuclear phagocytic system
mUNO	CSPGAK
NEAA	Non-essential amino acids
NHS	*N*-Hydroxysuccinimide
NPs	Nanoparticles
PBS	Phosphate buffered saline
PBS-T	PBS + 0.05% (v/v) Tween-20
PD-1	Programmed cell death protein 1
PDI	Polydispersity index
PEG	Polyethylene glycol
PFA	Paraformaldehyde
PHIS	Poly(histidine)
pLNPs	Pure lignin nanoparticles
PNIPAAm	Poly(N-isopropylacrylamide)
R848	Resiquimod
RBCs	Red blood cells
ROS	Reactive oxygen species
RPMI	Roswell Park Memorial Institute
RT	Room temperature
SFN	Sorafenib
SPECT/CT	Single photon emission computed tomography
TAMs	Tumor-associated macrophages
TB	Trypan Blue
TEM	Transmission electron microscopy
TGF-β	Transforming growth factor beta
THF	Tetrahydrofuran
TILs	Tumor-infiltrating lymphocytes
TME	Tumor microenvironment
TNBC	Triple-negative breast cancer
UV	Ultraviolet
Vin	Vinblastine sulfate
WHO	World Health Organization
ζ	Zeta

1 Introduction

Lignin is the second most abundant polymer, after cellulose, that can be obtained from renewable sources, and it comprises about 30% of the lignocellulosic biomass.[1] Despite of its abundance, only 2% of the annually extracted lignin is used in low-value applications, such as polymer synthesis, and are used as dispersants, adhesives and fillers, and the remaining 98% is used for energy production and recovery of pulping chemicals.[2–4] This is mainly due to the high polydispersity and complex structure of lignin that limits its use for other high-value applications. However, some chemical modifications in the lignin can be done to improve its properties. In addition, transforming raw lignin into lignin nanoparticles (LNPs) also allows the control of the morphology and structure of lignin.[4–6] The preparation of LNPs may open an avenue for the development of different lignin-based materials even for high-value applications, such as drug delivery and tissue engineering.[7]

Cancer is still one of the diseases with the highest incidence and mortality worldwide,[8] and despite all the improvements in the cancer treatment during the past years, the conventional chemotherapeutic drugs suffer from some limitations, including poor tumor-specific drug delivery, low water solubility and adverse side effects upon repeated administration.[9–11] To overcome these limitations, nanomedicines have emerged as a promising alternative to the conventional therapies, by improving the stability, solubility and circulation half-life of the therapeutic compounds, thus providing new tools for early detection, diagnosis, and superior treatment of cancer.[9,12–15] The physicochemical properties of nanoparticles (NPs), such as size, shape, charge, and surface chemistry and functionalization, can be fine-tuned to alter the biodistribution and *in vivo* biological interactions of the NPs upon administration.[16]

Besides the fact that NPs can benefit from the enhanced permeability and retention (EPR) effect, they can also be functionalized with several types of ligands that bind specifically to a certain target, enhancing their cellular internalization and delivery of their payloads, while minimizing their systemic side effects.[9,17,18] Additionally, NPs can also be used for immunotherapy applications due to their ability to carry antigens and adjuvants, in order to increase their immunogenicity, and also enhance the NPs' uptake by the antigen presenting cells (APCs), ultimately leading to an increased cross presentation of antigens to the cytotoxic T cells (CTLs).[19] Moreover, tumor associated macrophages (TAMs) have also appeared as a promising target for cancer immunotherapy due to the dominant presence of immunosuppressive TAMs in the tumor microenvironment (TME) of certain tumors, and their phenotypic plasticity enables the re-education into an anti-tumor phenotype, also known as M1-like macrophages.[20,21]

This thesis work started with the preparation and characterization of different lignin-based NPs, and further evaluation of their cytocompatibility properties towards several cell lines. Then, the ability of LNPs to load different chemotherapeutic compounds was evaluated, and drug release profiles were investigated in two different buffers (pH 5.5 and 7.4). Next, a carboxylation reaction of the original lignin polymer was performed in order to increase the amount of functional groups for consequent surface modifications. As a proof-of-concept study, the carboxylated LNPs were functionalized with a polymer and/or peptide, and release profiles of a poorly-water soluble cytotoxic compound (benzazulene) loaded into the LNPs were evaluated. Also, the *in vitro* antiproliferative effect of benzazulene was measured towards several cancer cell lines. In order to investigate the long-term stability of the LNPs at physiological conditions, different lignin polymers with several degrees of carboxylation were

prepared. After finding the optimal conditions in terms of stability, the LNPs were further functionalized with a cell-penetrating peptide (DSS), and the cellular internalization of the resulting DSS-modified LNPs was evaluated and compared with internalizing arginine-glycine-aspartic acid (iRGD)-functionalized LNPs, using two- and three-dimensional cell culture models. In the last study, the potential of the LNPs to load resiquimod was evaluated. Resiquimod is a compound that can induce the repolarization of M2- towards M1-like macrophages. The resiquimod-loaded LNPs were further functionalized with “mUNO”, a short peptide that targets the mannose receptor that is overexpressed in M2 macrophages. Homing ability of these LNPs to the macrophages in the TME was assessed, and the therapeutic effect of the resiquimod-loaded LNPs was studied in combination with a chemotherapeutic compound (vinblastine), by evaluating the immunological profile of the cells isolated from the tumors.

2 Literature overview

2.1 Lignin-based materials

Biorenewable polymers extracted from different sources have shown great potential as alternatives to commonly used metallic and organic materials for a variety of applications. They have attracted an increased attention from the research community due to their key advantages, which include biocompatibility, biodegradability, minimization of the environmental effects related with their usage, and low production cost.[22–25] Lignocellulosic biomass is one example of biopolymers that is derived from plant and wood sources, and represents the most promising renewable carbon-containing resource on Earth.[26,27] The composition of the lignocellulosic materials varies according to their origin and species (*e.g.*, softwood, hardwood, and grass), and they are constituted by 30–50% of cellulose, a polymer composed by glucose units, 20–35% of hemicellulose, a heteropolymer containing different polysaccharides, and 15–30% of lignin.[24,28]

Although lignin is a very abundant raw material, only about 2% of the annually extracted lignin from the woody biomass is used for low-value applications, including the synthesis of environmentally friendly polymers, typically used as dispersants, adhesives and fillers, while *ca.* 98% is burned in recovery incinerators for energy production and recovery of pulping chemicals.[2–4] This low utilization might be ascribed to the complex and variable lignin structure, high polydispersity, and non-miscibility with host polymer matrix.[3,27,29] To overcome these limitations, different procedures to chemically improve its properties and transform the original lignin into value-added fuels and chemicals can be done, as well as preparing LNPs that will improve the blending ability with host matrix and offer a morphological and structural control of the lignin.[4–6] Furthermore, the fabrication of lignin nanostructures also open up doors for the development of lignin-based materials for other high-value applications, including tissue engineering materials and drug delivery systems.[7] According to the statistics given by PubMed, studies related to the preparation of LNPs started to be published in 2006, and few reports have been published until now; while publications about the use of lignin polymer have been done since 1980 (**Figure 1A**). Moreover, among other kind of applications, only *ca.* 10% of the publications with LNPs are related to the nanotechnology and biomaterials field (data from Web of Science, **Figure 1B**). This means that the use of lignin as starting material for the production of NPs started recently, and there are many parameters that should be studied when considering LNPs for biomedical applications.

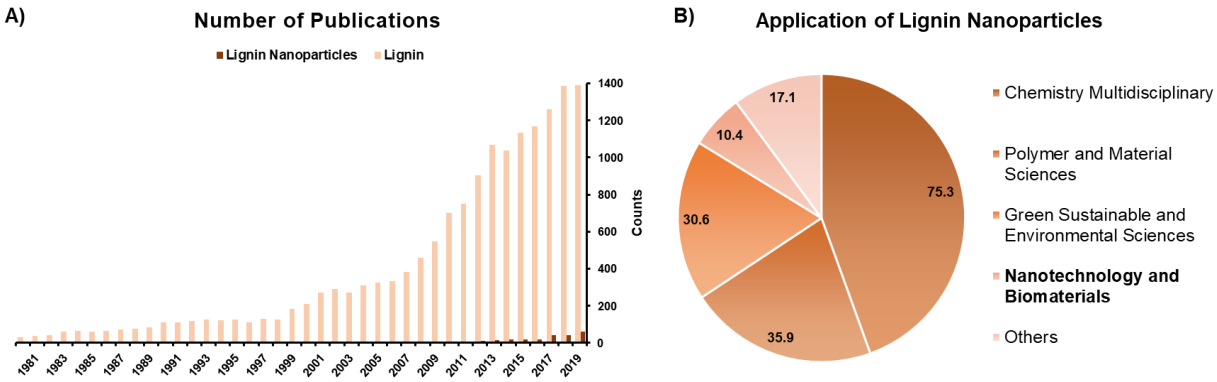

Figure 1. A) Number of publications searching keywords 'Lignin' and 'Lignin nanoparticles', until October 2019 (Source: PubMed). **B)** Percentage of publications with LNPs, according to their field of application (Source: Web of Science).

2.1.1 Introduction to lignin

Lignin comprises about 30% of the lignocellulosic biomass, and it is usually covalently bonded to the hemicellulose/cellulose structures, as represented in **Figure 2A**.[1] The primary function of lignin is to give strength and rigidity to the primary and secondary cell walls, acting as a structural component. Additionally, it is also responsible for the transport of water/solutes in the vasculature system of the plants, and for protection against environmental stresses, such as invasions by phytopathogens.[1,30,31]

Structurally, lignin is a highly branched biomacromolecule that comprises three units, so-called p-hydroxyphenyl (H), guaiacyl (G) and syringyl (S) units, which are originated from their respective monomers (monolignols) p-coumaryl, coniferyl and sinapyl alcohols (**Figure 2B**).[32,33] The synthesis of the monomers initiates by the deamination of the aromatic phenylalanine and further polymerization by a cascade of peroxidases and oxidases. Then, the lignin biosynthesis continues with a sequence of hydroxylation, methylation and reduction reactions by certain enzymes, resulting in the formation of the abovementioned three basic units.[27,34] Afterwards, the produced monolignols are transported to the apoplast through the plasma membrane, which are then activated to form the monolignol radicals that will polymerize to produce the lignin polymers, a process that is intermediated by enzymes like peroxidases, laccases and other polyphenol oxidases.[34,35] Regarding the bonds between monomers in the lignin structure, more than 50% corresponds to β-O-4′ ether linkages, which are the main target for most of the degradation mechanisms. Additionally, a smaller proportion of other types of linkages can be found in the lignin structure, including β-5 phenylcoumaran, β-β′ resinol, α-O-4′ ether, 4-O-5′ diphenyl ether, 5-5 biphenyl and β-1′ diphenyl methane, but these are more difficult to degrade during the traditional processing methods due to the carbon-carbon bond formation (**Figure 2C**).[28,36,37] Both chemical linkages and proportion of the monolignols affects the rigidity of the lignin structure, and vary according to the source of the lignocellulosic biomass.[24,27] For example, lignin obtained from softwoods is mainly composed by guaiacyl units connected by carbon-carbon and ether bonds, while lignin extracted from hardwoods presents equal amounts of syringyl and guaiacyl units, and grass lignin possesses the three monolignols in its structure.[30,33]

After acid or alkali treatment, the colorless lignin in the native state becomes of brown or dark brown color.[38] As a biorenewable polymer, the main advantages and properties of lignin polymers include their availability in large amounts at low prices, antifungal, antimicrobial and antioxidant properties, biodegradability, fire-retardant properties, and ability to absorb UV-radiation.[2,24,39–42] Other physicochemical properties make lignin an attractive polymer for the renewable energy industry and fabrication of other lignin-based products. Depending on the extraction process, the hydrophilic or hydrophobic nature of lignin can offer good rheological and viscoelastic properties, film-forming ability, and also compatibility with several industrial chemicals.[27] Additionally, the presence of reactive functional groups on its structure allows the conjugation with targeting moieties, such as peptides or antibodies, or the production of graft copolymers.[7,27] Moreover, due to its content in phenolic, hydroxyl, carboxyl and sulfonate functional groups, which vary according to the extraction process, the lignin polymer can be chemically modified using different approaches, allowing the lignin valorization and its use in the preparation of value-added products for a variety of applications (**Figure 2D**).[26,43]

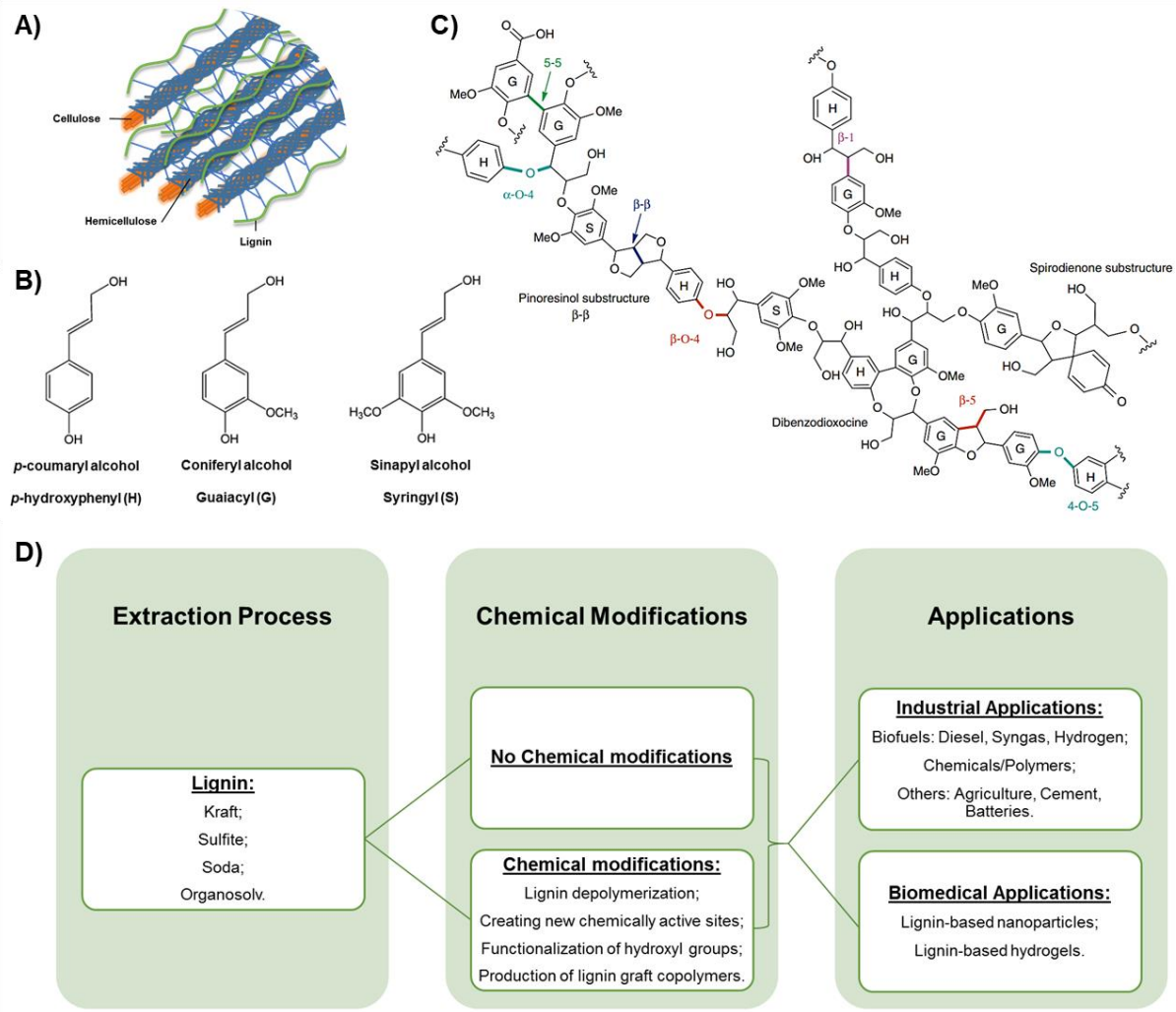

Figure 2. Schematic representation of **A)** lignin distribution in lignocellulosic biomass; **B)** monolignol monomers species present in lignin, and **C)** main linkages present in the lignin structure. **D)** Summary of the main industrial processes for lignin extraction, possible chemical modifications on the lignin structures and main applications. Copyright © 2018 Elsevier B.V. Adapted and reprinted with permission from ref.[7]

Processing methods for lignin extraction and chemical modifications

Generally, the extraction of lignin from lignocellulosic biomass is a process where the lignin is broken down into lower molecular weight compounds, whose physicochemical properties are influenced by the source and extraction method of lignin.[26–28] The most commonly used processes to extract lignin are kraft, sulfite, and organosolv processes.[44,45] These methods are different in several key parameters that influence the extraction process, including the ability of the chosen solvent/solute to participate in the lignin fragmentation process, to dissolve lignin molecules and to prevent the lignin recondensation, as well as the effects of temperature, pH and pressure on the system.[28,44] Consequently, the extracted lignin presents distinctive features and properties that vary according to the applied extraction method, affecting mainly the lignin solubility and molecular weight, and also the amount of functional groups on the lignin structure.[2,7,27]

Kraft process is the most commonly used method to process lignocellulosic materials, being responsible for *ca.* 85% of the extracted lignin.[46] Conventionally, the delignification process using the Kraft methodology initiates with the lignin dissolution after cleaving the ether linkages, in sodium hydroxide and sodium sulfide (white liquor) at high temperature (*ca.* 170 °C) and pH values ranging from 13 to 14.[44,45,47,48] Under these high pH values the phenolic hydroxyl groups will ionize, allowing the solubilization of the lignin that is consequently isolated from the remaining alkaline solution (black liquor) after lowering the pH to 5–7.5, by acid-mediated precipitation (*e.g.*, sulfuric acid).[27,49,50] The isolated kraft (also called alkali) lignin is hydrophobic, usually soluble in alkali or organic solvents, and it possesses an average molecular weight of 1000–3000 Da, but it can go up to 15000 Da.[2,45,51] In terms of functional groups, kraft lignin exhibits some amount of sulfur groups (1–2 wt-%) on its structure, in addition to the typical carboxyl, phenolic hydroxyl and methoxy groups.[27] The LignoBoost Technology has been used to commercially produce high quality softwood kraft lignin.[52] In 2013, Domtar's Plymouth (North Carolina Mill, USA) was the first industry to commercialize high-quality lignin as a by-product of their pulping process, which is now market as BioChoice® Lignin.[53] In 2015, the second commercially available softwood kraft lignin using the LignoBoost technology was started at the Stora Enso (Sunila Mill, Kotka, Finland), which is now called Lineo™.[54] More recently, UPM Biochemicals (Finland) have also started to produce UPM BioPiva™ softwood kraft lignin.[55]

The sulfite process is another extraction method that is commonly used in the pulp and paper industry, allowing to obtain lignosulfonates.[44] In this method, the pH of the system can vary from 2 to 12, according to the pulping chemicals mix and its dosage, and the reaction occurs at temperatures that can range between 120 and 180 °C.[7,44] This pulping process starts with the reaction between lignin and a sulfite, where the lignin and free sulfurous acid react to form lignosulfonic acid. Then, the presence of calcium, sodium, ammonium or magnesium as counter ions leads to the formation of water-soluble lignosulfonates, which are further fragmentated.[27,44] The hydrolysis and dissolution of the lignin is due to the incorporation of polar sulfonic groups in its backbone, whereas the cellulose remains as solid.[45,47] Consequently, the sulfur content of the lignosulfonates can vary between 4 and 8 wt-%, and they also exhibit higher average molecular weights (1000–50000 Da) than kraft lignin, as a result from the incorporation of sulfonate groups into the lignin structure.[44,45,47] Nevertheless, the sulfite method has some disadvantages, including the modification of the lignin structure due to the formation of new CC bonds, and also the presence of high content of ash and other impurities after the extraction process.[45]

Other extraction processes have emerged as promising alternatives to the conventional kraft and sulfite pulping methodologies. For example, the organosolv process involves the use of organic solvents (*e.g.*, ethanol, methanol, acetic and formic acid), usually mixed with water, as the delignifying agents on the treatment of lignocellulosic biomass, and at temperatures ranging from 170 to 190 °C.[45,56–58] Under this treatment, the lignin and hemicellulose are partially dissolved, and the recovery and separation of these two components are further carried out by adjusting the temperature, pH and concentration of the organic solvent, leading to the precipitation of lignin or the evaporation of the organic solvent.[58,59] With this process, the obtained lignin is sulfur-free, preserves its native structure and presents lower molecular weights (500–5000 Da) and ash-content.[45,47,56,60] Moreover, the organosolv pulping is a more environmentally friendly method and less aggressive compared to abovementioned processes, and the organosolv lignin is more suitable for further conversion and valorization.[7,45]

Although lignin can be used without any chemical modification, by incorporating the original lignin into a polymeric matrix to reduce production costs and improve the properties of

the end product (*e.g.*, as UV-light stabilizer, additive, filler, or antioxidant), the phenolic and aliphatic hydroxyl groups in the chemical structure can be modified in order to develop new lignin-based materials.[2,61–64] For that, different strategies can be done, such as: (i) lignin depolymerization or fragmentation, using processes like pyrolysis, hydrogenolysis, oxidation, hydrolysis and gasification, in which the lignin is cleaved and converted into valorized small fragments containing aromatic rings that are further used as fuels and basic chemicals or oligomers;[65,66] (ii) creating new chemically active sites on the original lignin polymer (*e.g.*, using hydroxyalkylation, amination, nitration, sulfomethylation and sulfonation reactions);[2] (iii) chemically modifying the hydroxyl groups on the original lignin structure (such as, alkylation, esterification, etherification, phenolation and urethanization);[2] and (iv) production of graft copolymers, in which the polymer chains are connected to the hydroxyl groups on the lignin backbone.[29] Both the reactivity of the functional groups and the structural characteristics of the lignin to be used will influence the efficacy of these chemical modifications and, consequently, the end-use application(s) of the produced lignin-based materials.[7]

2.1.2 Preparation of lignin-based materials

Although lignin is still an underexploited natural biomaterial, its potential as a starting material to develop more sophisticated nanomaterials has been recently emerging. Despite the high availability of lignin, its applications are restricted by the complex macromolecular structure that depends on the source and extraction method applied to isolate the lignin. However, this issue can be circumvented when the raw lignin is transformed into NPs with uniform size and shape.[67] In this way, different lignin-based nanomaterials have been prepared, including NPs, nanotubes, nanofibers, and hydrogels.[3,24,68] The presence of several functional groups on the lignin structure has been exploited to chemically modify the lignin and, therefore, increase the potential for a variety of applications, such as the preparation of nanocomposites, and also for biomedical applications (*e.g.*, drug delivery and tissue engineering).[7] For these purposes, different methods have been used to prepare a variety of lignin-based nanostructures, with different shapes and properties, such as anti-solvent precipitation, solvent exchange, interfacial crosslinking, sonication, and polymerization (**Figure 3**).[3,7]

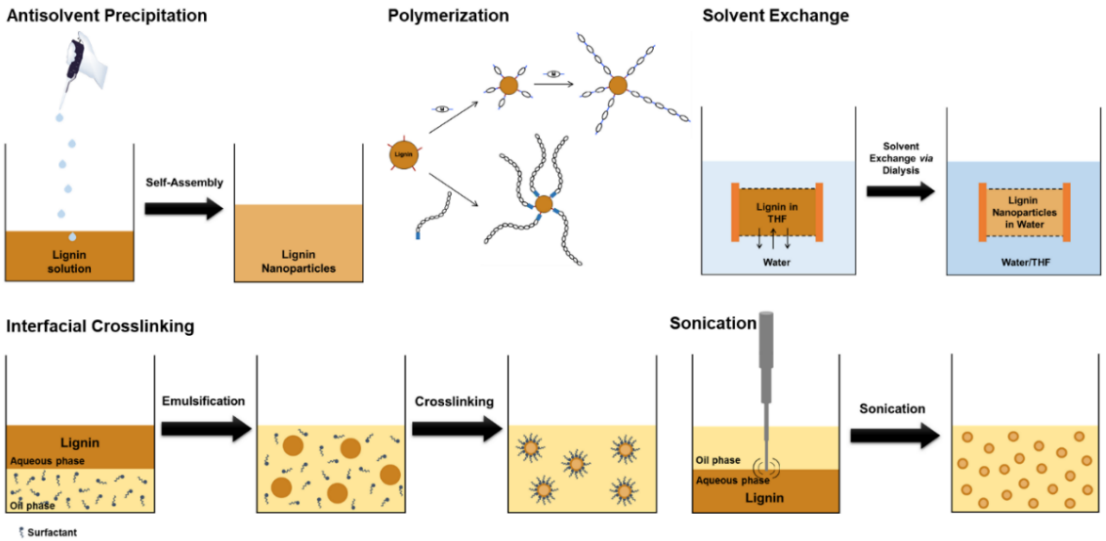

Figure 3. Representation of the different methodologies to produce LNPs. Copyright © 2018 Elsevier B.V. Reprinted with permission from ref.[7]

In addition to NPs, lignin has also been used in the preparation of hydrogels, mainly due to its intrinsic properties, such as biodegradability, biocompatibility, low toxicity, predisposition to undergo enzymatic degradation, and environmentally friendly properties as a natural polymers.[24] For this, lignin has been incorporated into different types of hydrogels in order to facilitate their formation and also to enhance their properties, which can also be used for drug delivery and tissue engineering applications.[24]

Anti-solvent precipitation

Generally, the anti-solvent precipitation approach to prepare LNPs relies on the self-assembly of the lignin, in which water or compressed liquid carbon dioxide (CO_2) can be used as anti-solvent, and a variety of different solvents are used to dissolve lignin, including tetrahydrofuran (THF), *N,N*-dimethylformamide (DMF), ethanol (EtOH), water/acetone, or water/THF/EtOH.[69–74] Besides the composition of the anti-solvent/solvents used in this method, other parameters can be changed in order to fine-tune the size and shape of the resulting NPs, including temperature, injection rate of the solution, pressure, initial concentration of the lignin solution, among others.[70] For example, Li *et al.* (2016) studied the effect of the dropping speed of water on the size of the lignin nanocapsules, after adding the water into a solution containing kraft lignin in EtOH at the initial concentration of 2.285 mg/mL, until the water content of the resulting solution reached 90%.[73] They found out that the average size of the nanocapsules was decreased when the dropping speed of water was increased from 0.0076 to 0.2 mL/s, reaching a plateau where the size no longer decreased even when the dropping speed was increased (0.4 mL/s). This trend was probably due to the fact that the self-assembly process of the lignin micellization and its aggregation morphology were driven by kinetics and thermodynamics. Therefore, when the dropping speed of the water was too fast, the nanocapsules could not reach a thermodynamically stable structure, because there was not enough time to grow.[73] Additionally, Xiong *et al.* (2017) also observed the same tendency for the effect of the dropping speed of water in the size of lignin nanospheres.[75] After adding the water at dropping speeds ranging from 2 to 8 mL/min into an enzymatic hydrolysis lignin solution in THF at initial concentration of 0.5 mg/ml, the size of the nanospheres decreased from *ca.* 315 nm to 190 nm, respectively.

In another study, Myint *et al.* (2016) studied the influence of temperature and pressure on the size and morphology of the NPs, using compressed liquid CO_2 as the anti-solvent, and DMF to dissolve the kraft (alkali) lignin.[70] When the pressure was constant, they noticed that the particle size and polydispersity index (PDI) were increased as the temperature applied in the system was increased, because aggregation/coalescence phenomena were observed to a higher extent. Also, the NP morphology was affected by the operating pressure. While keeping the temperature constant, the NPs were more aggregated and fused at low pressure (7.5 MPa) than the NPs fabricated at high pressures (15.0 MPa).

Using an industrially scalable method, Lintinen *et al.* (2018) assembled a closed cycle process for the production of colloidal lignin particles (CLPs), where a concentrated solution of softwood kraft lignin was dissolved in a mixture of THF/EtOH/water and added into the anti-solvent water, leading to the instantaneous self-assembling of lignin to form spherical CLPs with an average size of 200 nm and surface charge of −40 mV.[74] Additionally, this closed cycle system allowed full recovery of the solvents, with a low energy consumption.

Solvent exchange

In the solvent exchange method, or dialysis process, the lignin dissolved in an organic solvent (*e.g.*, THF or THF/methanol) is introduced into a dialysis membrane, which is further immersed in deionized water during 24 h, to allow the precipitation of the lignin upon the replacement of the organic solvent with water, possibly through a nucleation-growth mechanism.[76,77] In this method, the pre-dialysis concentration of the lignin solution seems to play an important role on the size of the LNPs. Lievonen *et al.* (2016) studied the effect of lignin concentrations ranging from 1 to 20 mg/mL on the particle size and PDI.[76] A minimum particle size (*ca.* 200 nm) and PDI (0.15) was obtained when the pre-dialysis lignin concentration was 1 mg/mL, while the particle size and PDI increased to 2000 nm and 0.56, respectively, when the initial concentration was 20 mg/mL. This effect might be ascribed by the fact that when higher concentrations of lignin are used, there is more lignin available for the growth of the NPs, and the nucleation-growth phenomenon is so fast that NPs with different sizes are formed, explaining the higher size- and PDI-values obtained. When lower concentrations of lignin are introduced into the dialysis membrane, there is a lower probability of nucleus formation, decreasing the chance to form larger particles and, therefore, the average size of the NPs and the PDI-values were decreased.

Lintinen *et al.* (2016) also prepared LNPs with different morphologies *via* solvent exchange, after pre-modification of the pre-dialysis lignin.[78] For that, the lignin was mixed with different ratios of iron(III) isopropoxide [$Fe(OiPr)_3$] in THF, and further submitted to a condensation reaction, where the condensation of the OH groups occurred to form Fe–O–C lignin bonds. This was followed by a hydrolysis step, in which water was added to allow the hydrolysis of the isopropoxy-groups and the condensation of adjacent Fe(OiPr)-moieties. For example, fishnet-type open network structures were obtained upon fast hydrolysis of equimolar ratios of –OH groups on the lignin and $Fe(OiPr)_3$. However, a controlled hydrolysis prevents the Fe:LNPs from fusing together, leading to the formation of small solid particles. When the ratio of OH_{lignin}:$Fe(OiPr)_3$ was increased to 3:1, lignin clusters were partially covered with the Fe(OiPr) moieties, and upon a rapid or controlled condensation, they can fuse together to form larger solid particles or hollow spheres, respectively.

Interfacial crosslinking and ultrasonication

The interfacial crosslinking technique requires the mixture of an aqueous and oil phases, with or without the use of surfactants and crosslinking agents, leading to the formation of precursor microemulsions to generate particles after crosslinking of the dispersed materials.[79,80] Ultrasonication can also be used to assist and generate the microemulsions.[80,81] Using this approach, Yiamsawas *et al.* (2014) synthesized lignin hollow nanocapsules with an average diameter of 150–200 nm and an aqueous core that allowed the encapsulation of different hydrophilic compounds,[81] overcoming the limitation of the abovementioned anti-solvent precipitation and solvent exchange methods that generally allow the encapsulation of hydrophobic molecules. For that, lignosulfonic acid sodium salt or kraft lignin was dissolved with MilliQ-water, mixed with cyclohexane containing polyglycerol polyricinoleate as surfactant, and then ultrasonicated to create a stable microemulsion. Posteriorly, an overnight polyaddition reaction was conducted at the interface of the microemulsion droplets after adding toluene diisocyanate in cyclodextran to the previously prepared emulsion. A water-soluble lignin (lignosulfonate) was also used by Chen *et al.* (2016) to generate oil-in-water

microemulsions and preparing pH-sensitive nanocapsules for encapsulation of hydrophobic molecules.[82] In this case, the lignosulfonate was previously grafted with allyl groups *via* etherification, and the microemulsion was then conducted by ultrasonication, in which the modified lignosulfonate and the surfactant (sodium dodecyl sulfate) were dissolved in the water phase, while the oil phase contained butyl acetate, co-stabilizer (hexadecane), an initiator and the cross-linker. Both lignosulfonate and cross-linker contacted at the water and oil interface, and reacted by free radical induced thiol–ene crosslinking reaction.

Ultrasonication is a process based on a phenomenon called cavitation, in which occurs the formation of cavities and further creation of radicals. Different parameters can affect the formation of radicals, including the type of solution, temperature and pressure of the system, and ultrasound settings (*e.g.*, duration and power).[83–85] When using lignin solutions, the nature of the lignin polymer can also affect the composition and structural changes of the obtained LNPs.[85] For example, Kim *et al.* (2013) prepared ionically crosslinked chitosan–lignosulfonate NPs with antibacterial properties *via* ultrasonication.[86] After selecting the best conditions for the several parameters tested, including the pH-value (4.5, 5 and 6), sonication time (2, 5, 8 and 10 min), non-ionic surfactants (poloxamer 407 or Tween 80) and concentration of both chitosan and lignosulfonate, the preparation of the NPs was successful. The lignosulfonate in water exhibited sulfonate groups (SO^{3-}), which are anionic polyelectrolytes acting as counter ions to prepare chitosan NPs with increased stability. The best conditions to prepare the smallest NPs with low PDI were found after adjusting the pH of the chitosan to 5, the sonication time was set to 8 min, using 1% (v/v) of poloxamer as surfactant, and a chitosan/lignosulfonate mass ratio set as 2:1. Besides the abovementioned parameters, the effect of the ultrasonic intensity on the preparation of LNPs was evaluated by Wang *et al.* (2019) using the antisolvent precipitation method assisted by ultrasonic sonication, with ultrasonic intensities of 0, 100, and 200 W, after dropping of water into the acetylated alkali lignin/THF solution at the final concentration of 2.0 mg/mL.[87] Different sizes and shapes of the LNPs were observed when using different ultrasonic intensities: (i) without ultrasonic treatment (0 W), the prepared LNPs presented large average size, irregular shape, and broad size distribution; (ii) a mild ultrasonic treatment (100 W) allowed the preparation of more regular and well-separated LNPs, but still with a broad diameter distribution (*ca.* 200−800 nm); and (iii) with a high ultrasonic intensity (200 W), the LNPs exhibited good sphericity and proper size distribution.

Polymerization and electrospinning

Polymerization technique can be employed to produce advanced lignin-based materials, in which lignin is previously grafted with other polymers, for example, either *via* atom transfer radical polymerization (ATRP), or ring-opening polymerization.[88,89]

Using an ATRP approach, Liu *et al.* (2015) grafted 2-(dimethylamino)ethyl methacrylate (DMAEMA) onto the lignin-based macroinitiators, resulting in a hyperbranched structure composed of a hydrophobic lignin backbone and multiple cationic hydrophilic arms of the DMAEMA polymer that efficiently compacted DNA into this structure, for potential gene delivery applications.[88] In another study, Kai *et al.* (2015) fabricated a series of poly(methyl methacrylate) (PMMA) grafted lignin copolymers through ATRP, using different lignin:PMMA mass ratios (5.6% to 46.1%), rendering copolymers with different PMMA chain lengths and properties.[89] Posteriorly, these copolymers were blended with poly(ε-caprolactone) (PCL) to form nanofibrous composites *via* electrospinning, improving the tensile strength and Young's modulus of the as-prepared nanofibrous composites, with good biocompatibility and improved

attachment, interactions and proliferation of human dermal fibroblasts for biomedical applications.

A ring-opening polymerization methodology can also be used to prepare lignin-based composites. For example, Kai *et al.* (2017) fabricated lignin–poly(ε-caprolactone-*co*-lactide) (lignin–PCLLA) copolymers, with different mass ratios of the lignin, PCL and ι-lactide polymers, *via* solvent-free ring-opening polymerization.[90] Posteriorly, these copolymers were blended with PCL or poly(ι-lactic acid) (PLLA) by electrospinning, resulting in the formation of nanofibers with sizes ranging from 300 to 500 nm. The incorporation of the lignin polymer in both PCL/lignin−PCLLA and PLLA/lignin−PCLLA nanofibers resulted in the improvement of mechanical properties, as well as *in vitro* biocompatibility and antioxidant activity, suggesting that these copolymers and nanofibers could be used for biomedical or other healthcare applications. In another study conducted by the same research group, poly(lactic acid) (PLA)–lignin composites were engineered using the same approach, in which the content of alkylated lignin in the composites varied from 10 and 50%, and the grafted PLA chain length ranged from 5 to 38.[91] The resulting copolymers were blended with PLLA and engineered into PLLA/PLA-lignin nanofibrous composites through electrospinning. It was observed that the copolymers comprising a higher content of lignin resulted in the production of thinner nanofibers, which can be ascribed to the low molecular weight of this copolymer and, therefore, a decreased viscosity of the spinning solution. Furthermore, the higher lignin content copolymer also showed the highest antioxidant activity among all the PLLA/PLA-lignin nanofibers, due to the intrinsic antioxidant property of the lignin polymer. Additionally, the lowest content of lignin in the PLLA/PLA-lignin nanofibers exhibited good biocompatibility and induced higher cell proliferation on: (i) PC12, a common cell line used in neurotoxicological studies and nerve regeneration; (ii) human dermal fibroblasts (HDFs), a cell line that exists within the dermis layer of human skin and presents a critical role in the wound healing process; and (iii) human mesenchymal stem cell (MSCs), which are multipotent stromal cells capable to differentiate into several cell types, such as bone cells, myocytes, nerve cells and chondrocytes. Overall, these results suggested that such lignin-based materials present high potential in the fabrication of scaffolds for tissue engineering applications.

Hydrogels

Hydrogels comprise a 3D network of hydrophilic polymers that form bonds between polymer chains and allow a superior absorption of water compared to their own dry weigh, being generally classified according to the chemical or physical interactions in the 3D structure network: (i) chemical hydrogels, prepared by converting hydrophobic monomers and polymers into hydrophilic ones and cross-linking water-soluble monomers and polymers, connected through covalent bonds, and (ii) physical hydrogels, which present networks linked together by secondary forces, such as ionic forces, hydrogen bonds, van der Waals interactions, and hydrophobic forces.[92–94] In the past years, it has been observed an increased demand on the fabrication of hydrogels based on natural polymers in preference to the synthetic polymers, mainly due to their low toxicity, biocompatibility and biodegradability, responsiveness to enzymatic degradation and their intrinsic eco-friendly properties.[92,95] Among other biopolymers, lignin has been used to develop different types of hydrogels in order to facilitate the hydrogels' formation and improve their properties for a wide range of applications, including wound dressings, drug delivery and tissue engineering.[7,24] After mixing lignin and cellulose in an alkaline solution, and further chemical cross-linking with epicholohydrin, Ciolacu *et al.* (2012)

fabricated cellulose-lignin hydrogels for drug delivery aplications.[96] By controlling the composition of the hydrogels and increasing the lignin content in the matrices, it was possible to change the swelling process and increase the release of polyphenols from the hydrogels. A radical polymerization assisted by ultrasonication was used by Wang *et al.* (2016) to prepare lignosulphonate-grafted poly(acrylic acid-*co*-poly(vinyl pyrrolidone)) hydrogels to incorporate amoxicillin, exhibiting a pH-responsive and controlled drug release, with improved release profiles in simulated intestinal fluids compared to the simulated gastric fluids.[97]

In another study, Diao *et al.* (2014) synthesized temperature sensitive lignin thermogelling graft copolymers using ATRP, after grafting multiple polymer chains of a block of brush-like random copolymer of poly(ethylene glycol) (PEG) and poly(propylene glycol) (PPG) and a block of poly(N-isopropylacrylamide) (PNIPAAm) onto the lignin core.[98] PNIPAAm-*block*-PEG/PPG and PNIPAAm-*random*-PEG/PPG copolymers with different block architecture were obtained, and when grafted onto the lignin core, were found to play an important role in the hydrogel formation. The PNIPAAm-*block*-PEG/PPG copolymer exhibited thermogelling behavior going from a solution at low temperatures to a hydrogel at 32–34 °C, and then to a dehydrated gel at higher temperatures; however, when the PNIPAAm-*random*-PEG/PPG copolymer was grafted onto lignin using the same monomer ratio, the formation of hydrogel did not take place at any temperature. In this formulation, the PNIPAAm was crucial for the gelling at the critical gelation temperature, and the PPG chains can contribute to the water retention by balancing the hydrophilicity/hydrophobicity of the hydrogel network at the temperatures up to 52 °C. The fabricated hydrogel can experience a thermogelling transition at a temperature lower than human body temperature and higher than room temperature, indicating that it can be used for drug delivery and tissue engineering (*e.g.*, stem cells culture and differentiation).

2.1.3 Biomedical applications of lignin-based nanomaterials

The fabrication of lignin-based nanomaterials offers crucial advantages, including the improvement of the properties of polymer blends, and a higher antioxidant activity due to the higher surface area-to-volume ratios.[4,69,71] Moreover, the presence of functional groups on the lignin structure that can be easily chemically modified increases the potential of the LNPs for a wide range of biomedical applications.[7] As a result of their intrinsic properties, lignin-based nanomaterials present a great potential to be used in surface coatings in the preparation of nanocomposites and stabilization of Pickering emulsions, for example, in drug/gene delivery and tissue engineering.[7] The main biomedical applications and preparation methods of lignin-based nanomaterials, and respective outcomes are summarized in **Table 1**.

Table 1. Overview of the main biomedical applications of lignin-based materials, with reference to the type of lignin, preparation method and main outcomes of these materials.

Type of Lignin (Shape)	Preparation Method	Outcome	Ref.
Antioxidant Properties			
Enzymatic hydrolysis lignin (Spherical)	Anti-solvent precipitation	Besides the influence of the total phenolic content, the particle size was shown to have a proportional effect on the antioxidant activity of the LNPs, where smaller NPs exhibited the highest activity.	[99]
Organosolv lignin (Nanospheres)	Supercritical anti-solvent process	The nanosized lignin (*ca.* 144 nm) exhibited much higher antioxidant ability compared to the irregular non-nanoscale lignin (around 1–100 μm).	[69]

Alkali lignin (Nanofibers)	Polymerization and electrospinning	Different lignin−PCLLA copolymers were prepared, with molecular weights ranging from 10 to 16 kDa and glass transition temperatures from −40 to 40 °C. The incorporation of lignin copolymers greatly enhanced the antioxidant properties of the resulting copolymers, compared to the PCL or PLLA counterparts.	90
UV Absorbing Capability			
Alkali lignin (Spherical)	Liquid precipitation method	Pure PVA films, PVA films with raw lignin, and PVA films with LNPs were fabricated. The films with LNPs exhibited better performance for UV absorption then the ones containing raw lignin, due to the presence of more phenolic groups on the surface of the NPs.	100
Organic acid lignin (Spherical)	Solvent exchange	The lignin particles (dosage of 5%) presented a high ability to enhance the sun protection factor values of lotions (by 2.80–3.53), showing also UVA/UVB values in the range of 0.69–0.72. Additionally, the addition of lignin particles to the lotion improved the antioxidant and UV protection abilities, suggesting that lignin can have a broad-spectrum skin photo-protection effect.	101
Acetylated alkali lignin (Spherical)	Ultrasonication	The addition of LNPs with smaller size enhanced the sunscreen performance of a commercial pure cream compared to the LNPs with larger size.	87
Antimicrobial Properties			
Kraft lignin (Spherical)	Anti-solvent precipitation method	The as-prepared Ag^{+}-infused EbNPs, coated with a cationic polyelectrolyte (PDAC), showed higher antimicrobial activity and inferior environmental impact than metallic AgNPs.	102
Kraft lignin (Spherical)	Ion and solvent exchange	The AgCLPs showed high antibacterial efficacy, with low silver loading, even without the cationic polyelectrolyte coating.	77
Chitosan-lignosulfonate (Spherical)	Ultrasonication	The chitosan-lignosulfonate complexes were found to have and increased antibacterial effect on both gram-negative and gram-positive bacteria, compared to the chitosan alone.	86
Pickering Emulsions			
Kraft lignin (Spherical)	Anti-solvent precipitation method	The adsorption of cationic lignin onto the CLPs originated positively charged particles that provided an improved stability in a wider range of Pickering emulsions at pH values ranging from 2 to 6, compared to the irregular lignin particles or the regular CLPs. This might be ascribed to their pH-dependent surface charge, amphiphilicity, and the intermolecular stabilization due to the electrostatic and cation-π interactions of the cationic CLPs.	103
Kraft lignin (Spherical)	Interfacial crosslinking	Larger lignin particle size led to better stability and increased emulsion drop size.	79
Alkali lignin	Polymerization	Water-insoluble lignin was grafted with 2-(diethylamino)ethyl methacrylate (DEAEMA), rendering a polymer that presented CO_2/N_2-switchability of dispersion/precipitation, correlated to the graft density and chain length of DEAEMA units, which can be used as a surfactant for Pickering emulsions.	104
Drug and Gene Delivery			
Alkaline lignin (Spherical)	Anti-solvent precipitation method	Lignin was self-assembled with resveratrol and iron oxide magnetic NPs to form a stable nanodrug carrier that showed and improved drug accumulation and tumor reduction *in vivo*, along with lower adverse effects than the free resveratrol.	105
Enzymatic hydrolysis lignin (Spherical)	Anti-solvent precipitation method	Lignin hollow NPs were loaded with doxorubicin, and covered by magnetic NPs and folic acid through layer-by-layer self-assembling. As a result, the folic-magnetic-functionalized lignin hollow NPs answered to the magnetic field and targeted the folic acid receptors, increasing the cellular uptake of NPs into HeLa cells.	106
Organosolv lignin (Spherical)	Ultrasonication	The curcumin-loaded LNPs showed an improved bioavailability after oral administration compared to the free curcumin, which can be ascribed to the enhanced curcumin solubility and stability, sustained release and superior intestinal permeability and consequent its absorption, as well as the inhibition of P-gp mediated efflux.	107
Different Lignin sources (Nanotubes)	Polymerization	Vehicles for gene delivery and transfection with HeLa cells.	108
Tissue Engineering			
Kraft lignin (Scaffold fibers)	Electrospinning	The incorporation of 10 wt-% lignin in the lignin-PCL composites resulted in a minimum fiber diameter and optimal pore size, along with an enhanced mechanical, physical, and morphological properties	109

		compared with pure PCL, making the lignin-PCL promising for tissue regeneration applications.	
Alkylated lignin (Nanofibers)	Polymerization and electrospinning	The incorporation of lignin into the PLLA/PLA-lignin nanofibers increased their antioxidant activity, and showed good biocompatibility and induced higher cell proliferation (PC12, HDFs, and MSCs), relevant cell lines for tissue regeneration applications.	91
Enzymatic hydrolysis lignin (Aerogels)	CO_2 induced gelation and supercritical drying	Stable calcium-crosslinked alginate–lignin aerogels were prepared, using up to 2:1 (w/w) alginate-to-lignin ratio. The resulting aerogels presented good cytocompatibility and cell adhesion, making them promising for tissue engineering and regenerative medicine.	110

Abbreviations: Ag: Silver; CLPs: Colloidal lignin particles; EbNPs: Environmentally benign lignin-core NPs; HDFs: Human dermal fibroblasts; LNPs: Lignin NPs; MSCs: Mesenchymal stem cell; PCL: Polycaprolactone; PCLLA: Poly(ε-caprolactone-co-lactide); PDAC: Polydiallyldimethylammonium chloride; P-gp: P-glycoprotein; PLA: Poly(lactic acid); PLLA: Poly(ι-lactic acid); PVA: Poly(vinyl alcohol); SAS: Supercritical anti-solvent.

Antioxidant compounds possess the ability to inhibit or scavenge free radicals in order to prevent oxidation, being particularly interesting for several industries, including pharmaceuticals, cosmetics, food, plastics, and oil fuel production.[111–113] Originated from natural sources, lignin has the potential to replace synthetic antioxidant compounds, due to the biodegradability and low toxicity. Moreover, the abundance of hydroxy- and methoxy-groups in the lignin backbone prevents the oxidation propagation reactions by hydrogen donation, and acts as a stabilizer in reactions induced by oxygen and reactive oxygen species (ROS) to slow down the ageing process of different composites and biological systems.[111,114,115]

Although raw lignin presents an inherent antioxidant property, the source of the lignin polymer can influence the scavenging ability, as demonstrated by Yearla and Padmasree (2016).[71] In their study, the absorbance of 2,2-diphenyl-1-picrylhydrazyl (DPPH) radical at 517 nm was measured to compare the antioxidant potential of softwood alkali lignin (AL) and hardwood dioxane lignin (DL). The AL showed higher DPPH scavenging ability than the DL, possibly owing to the higher guaiacyl content in the softwood AL, which presents higher antioxidant ability due to the ortho-methoxy substitution, as well as the lower carbohydrate contamination in AL compared to DL.[71,116] Moreover, the AL and DL were nanosized to ALNPs and DLNPs, respectively, which increased even more their radical scavenging ability compared to the raw lignin polymers, showing the following order for the antioxidant potential: DLNPs > ALNPs > DL > AL.[71] Additionally, the antioxidant activity was also dependent on the size of the LNPs, in which smaller NPs exhibited higher activity due to the better accessibility of phenolic hydroxyl groups to free radicals compared to the larger particles.[99]

The UV-protective or absorbing properties of the lignin polymer is especially important in the formulation of sun protection lotions due to the excellent sunscreen performance by reducing the UV exposure, in particular the UVA and UVB transmittances. For example, Lee *et al.* (2019) prepared lignin-poly(vinyl alcohol) (PVA) nanocomposite fibers *via* electrospinning, with 50 and 85 wt-% lignin content.[117] Both ratios of the lignin-PVA composites showed UV protection factors higher than 50, indicating an excellent UV protection of the nanocomposite fibers. This UV-blocking effect of lignin is ascribed to the different functional groups present in the lignin structure, such as phenols, ketones and other chromophores, being considered a natural broad-spectrum sun blocker.[118,119] Additionally, Qian *et al.* (2015) verified that after incorporation of 2 or 10 wt-% lignin into a commercial sunscreen lotion made a sun protection factor (SPF) of 15 reach that of a SPF 30 or SPF 50, respectively.[120] Therefore, lignin can be considered as a green alternative to substitute the synthetic sunscreen actives currently available in the market.

Lignin is also a source of natural antimicrobial compounds, in which the phenolic monomeric fragments of the lignin can inhibit several microorganisms, including *E. coli*, *B. licheniformis*, and *S. cerevisiae*.[111,121] This inhibitory mechanism can be ascribed to the presence of the C-C double bond in the α- and β-positions of the side chain and a methyl group in the γ-position in the phenolic fragments, which are more inhibitory than the phenolic fragments containing functional groups with oxygen (*e.g.*, –OH, –CO, and –COOH) in the side chain.[111] Additionally, the intrinsic antimicrobial activity can also be correlated with the antioxidant property of the lignin, in which a higher antimicrobial effect of the lignin is related with a superior radical scavenging activity of the soluble lignin fractions.[114,122] Additionally, silver (Ag^+)-infused LNPs can also be prepared to potentiate the antibacterial effect of the Ag ions against Gram-positive and Gram-negative bacteria strains, using lower amounts of Ag to produce the same effect as the free Ag ions.[77,102] This provides an environmentally friendly approach to replace the conventional metallic AgNPs, whose usage is limited by their high toxicity, persistence in nature, and negative effects related to their accumulation in water systems.[77,123]

Pickering emulsions consist of emulsions stabilized by the presence of solid particles at oil–water interface, instead of using typical surfactants as stabilizers as in conventional emulsions.[124,125] Compared to the conventional emulsions, Pickering emulsions can provide an increased stability against coalescence, biocompatibility and safety for *in vivo* purposes, as well as stimuli-responsiveness, being used in different fields, including biomedical, food and cosmetics.[124] Generally, the mechanism for the stabilization in Pickering emulsions relies on the formation of a steric barrier at the oil–water interface, where the solid particles attach in an irreversible manner, providing an improved stabilization compared to the surfactant adsorption.[124,125] However, the type of Pickering emulsion (oil-in-water or water-in-oil), the stability and morphology will depend on the properties of the solid particles, and the most commonly used particles are composed by silica, chitosan, magnetic NPs, nanotubes and cyclodextrin, among others.[124] In addition to those, LNPs have been proposed as alternative to improve the stabilization of Pickering emulsions *via* steric and electrostatic repulsion.[126] An effective stabilization will depend on the LNP properties, such as average size and size distribution, surface charge, wettability, LNP concentration, and presence of functional groups that allow the grafting onto lignin core or modification of LNPs with stimuli-responsive materials.[103,126,127]

Finally, lignin has gained increased attention as a starting material to prepare a variety of LNPs and other lignin-based drug/gene delivery carriers (*e.g.*, micro/nano-capsules, micro/nano-particles, and hydrogels) or tissue engineering and regeneration materials (*e.g.*, hydrogels, scaffolds or nanofibers).[7,128] As discussed in section 2.1.2, different methodologies and several parameters can be fine-tuned to develop lignin-based materials with suitable properties for the desired application. In particular, LNPs have recently emerged as a platform to deliver different compounds for cancer therapy, and the majority of the existing literature is mainly focused on *in vitro* anticancer studies, while the *in vivo* assessments are barely studied, with only few reports on the *in vivo* performance of LNPs.[7,129] For example, Dai *et al.* (2017) evaluated the anticancer effect of resveratrol-loaded LNPs both *in vitro* and *in vivo*.[105] In this study, the non-loaded NPs did not show adverse hemolysis effects or other side effects, while the resveratrol-loaded NPs showed a significant inhibition of tumor growth.

2.2 Nanomedicines for cancer therapy

According to the World Health Organization (WHO), cancer consists of a group of the diseases with the highest incidence and mortality worldwide.[8] Cancer is characterized by the uncontrolled division and growth of anomalous cells that ultimately can acquire the capacity to invade the surrounding tissues and spread to other organs.[130] In 2018, there were 18.1 million new cases and 9.6 million deaths, and these numbers are expected to increase in the future to 20 million new cancer cases per year by 2025.[8]

Currently, the cancer treatments rely on surgery to remove the tumor, and chemotherapy together with radiation to kill tumor cells that are more susceptible to these treatments due to their ability to divide and grow faster than healthy cells.[131] A variety of chemotherapeutics have been mainly used to induce apoptosis, interfere with the cell cycle progression and gene transcription, and inhibit angiogenesis.[131,132] Despite all the advances in the cancer treatment modalities during the recent years, most of the conventional chemotherapeutic drugs still lack efficiency to eradicate the cancer. These challenges are mainly due to the poor tumor-specific delivery and non-specific distribution of the drugs in the body, which can lead to appearance of systemic side effects caused by the high toxicity towards healthy cells, and low water solubility and therapeutic index of the chemotherapeutics.[9] This will eventually induce multidrug resistance, defined as either a lack of tumor size reduction or the occurrence of clinical relapse after an initial positive response to antitumor treatment.[10,11] Additionally, other therapeutic modalities have been investigated in order to answer the hallmarks of cancer that were established to rationalize and understand the complexity of this disease.[133] The therapeutic approaches that target the hallmarks of cancer include the use of epidermal growth factor receptor (EGFR) inhibitors to sustain the proliferative signaling, immune activating anti-cytotoxic T-lymphocyte associated protein 4 (CTLA-4), monoclonal antibodies to avoid the immune destruction, and inhibitors of vascular endothelial growth factor (VEGF) signaling pathways that induce angiogenesis, among others.[133]

Nanomedicines have emerged as innovative and promising alternative technologies with many advantages over the conventional therapies, providing new opportunities for early detection, diagnosis, and enhanced treatment of cancer.[12] Moreover, these nanosystems can also be used to carry multiple therapeutic molecules for synergistic cancer therapy.[134] Additionally, theranostic platforms in cancer combine both diagnostic and therapeutic tools in a single formulation, offering the possibility to have an individualized treatment regimen (*e.g.*, select the therapy and monitor the response to the treatment based on the specific molecular characteristics of the disease).[135–137] In fact, nanoparticulate drug delivery systems have been utilized in clinical practice since the 1990's. Until 2016, over 25 nanomedicines were approved either by Food and Drug Administration (FDA) or European Medicines Agency (EMA), and other 45 nanoparticulate systems were at that time in ongoing clinical trials.[138] Since 2016, another 3 nanomedicines were approved, and 18 new NPs have entered clinical trials, of which 17 are indicated for cancer therapy.[139]

Generally, the distinctive characteristics of cancer nanomedicines include: (i) biocompatibility; (ii) the ability to improve the pharmaceutical properties of the therapeutic molecules, such as stability, solubility and circulating half-life; (iii) co-deliver multiple drugs to improve their therapeutic efficiency and overcome drug resistance; (iv) deliver the payloads specifically to a certain cell or tissue, reducing their side effects; and (v) sustain or trigger the drug release upon a certain stimulus.[9,13–15] The physicochemical properties of NPs, such as size, shape, charge, and surface chemistry can determine their biodistribution and *in vivo* biological interactions, upon a specific administration route (**Figure 4**).[16] Therefore, it is

important to choose the NPs' composition and tailor and design the NPs, according to their application and administration route to have the desired properties/effects.

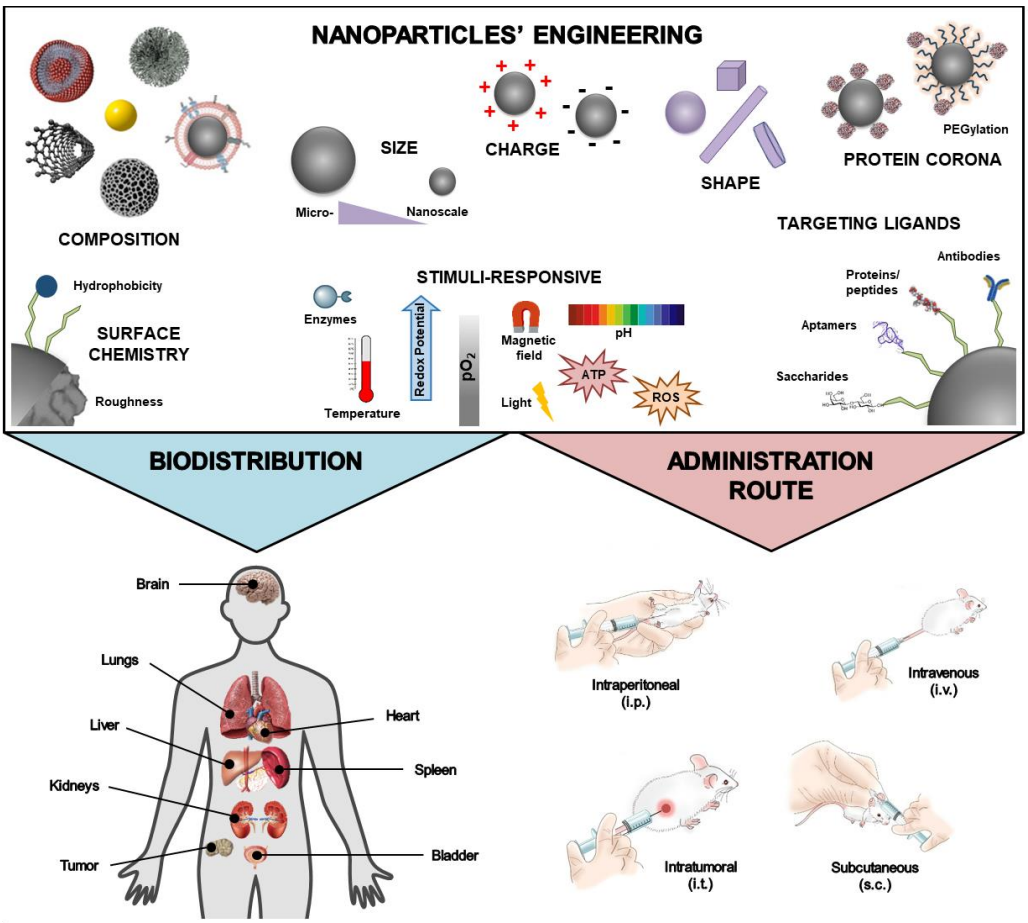

Figure 4. Parameters that should be considered when engineering nanoparticles, such as composition, charge, size and surface chemistry of the NPs, as well as the use of targeting ligands or stimuli-responsive materials. These parameters should be evaluated carefully according to the administration route, as they will affect the biodistribution of the nanoparticles after *in vivo* administration. Copyright © 2020 Elsevier B.V. Adapted and reprinted with permission from ref.[16]

Administration route

The abovementioned physicochemical properties of the nanocarriers impact their stability, delivery efficiency, and biodistribution upon administration. The delivery of NPs into the tumor is affected by several factors: NPs should (i) evade clearance by renal filtration and the reticuloendothelial system (RES); (ii) extravasate through the enlarged endothelial gaps in tumors; (iii) penetrate the compact stroma in the TME to reach the tumor cells; (iv) persist in the tumor tissue for a sustained period of time; and (v) release the therapeutic agents to induce their pharmacological effect.[140–142] Therefore, the design of the NPs should be optimized and adjusted taking into consideration the tumor physiology and the administration route of the NPs for optimal delivery of the payloads.[140,143,144] The delivery of nanocarriers to the tumor tissue in different animal species usually involves a systemic or local administration, where the most commonly used approaches are intravenous (i.v.), intraperitoneal (i.p.), and intratumor (i.t.).

The local delivery of nanomedicines (*e.g.*, i.t. injection) should be considered when the tumor site is accessible, avoiding the need of the EPR effect. Additionally, bypassing the systemic administration can also help to easily overcome other physiological barriers and achieve a better therapeutic effect at the tumor site, with reduced systemic toxicity, being a promising approach for tumors in the lung, bladder, brain and eye.[145–148] Regarding the systemic administration of nanomedicines, the i.v. route of administration can be used to deliver the nanomedicines to the tumor tissue, and the NPs can benefit of the EPR effect in some solid tumors, which is responsible for the "passive targeting" of nanomedicines to the tumor site.[149,150] Additionally, the i.p. administration of nanomedicines is an attractive strategy for the treatment of peritoneal carcinomatosis for different animal models.[151] The peritoneal carcinomatosis is characterized by the attachment of cancer cells to the mesothelial layer on the peritoneal membrane, originating primary cancers in peritoneal cavity of certain organs, including ovary, liver, colon, pancreas and stomach.[151,152] Delivering the nanomedicines by i.p. injection will retain the therapeutic agents as much as possible in the peritoneal cavity, maximizing the therapeutic efficiency and limiting the systemic side effects.[151]

Composition

The NP composition affects the biodistribution and stability, as well as the optical/magnetic properties. Nanomedicines can be classified as organic or "soft" NPs (*e.g.*, polymeric and lipid-based NPs), inorganic or "hard" NPs (*e.g.*, silicon/silica NPs, gold NPs, iron oxide NPs, and carbon nanotubes), or biologically-derived nanoplatforms (*e.g.*, cancer cell or red blood cell membrane-coated NPs).[12,153,154] Additionally, the preparation of pure drug nanocrystals can also improve solubility and bioavailability of poorly water-soluble drugs.[155] The main advantages and disadvantages of each nanosystem are summarized in **Table 2**.

Size, shape, surface chemistry and charge

In addition to the effect of the NP composition, the physicochemical properties of the nanomedicines (*e.g.*, size, morphology, surface chemistry and charge) can also alter the cellular interaction and *in vivo* pharmacokinetics, such as biodistribution, cellular uptake, and half-life of NPs in the bloodstream after administration.[156]

Regarding the NP size, smaller NPs (< 5.5 nm) tend to face a rapid renal filtration and consequent urinary excretion, while NPs larger than 200 nm can suffer from liver and spleen clearance, while particles or NP aggregates larger than 2 μm will accumulate in the lungs.[156–158] Consequently, the optimal NP size that shows an increased extravasation through the vasculature at the tumor and benefits of the EPR effect appears to range between 20 and 200 nm.[159] In addition to the influence on the *in vivo* fate of the NPs, the particle size also influence the pathway by which the NPs are internalized by different cells: (i) large particles are more likely to be internalized by phagocytosis; (ii) particles smaller than 1 μm can be taken up non-specifically by micropinocytosis; and (iii) smaller particles (60–200 nm) can be internalized using different mechanisms, such as clathrin- and caveolin-mediated endocytosis or clathrin- and caveolin-independent endocytosis.[160–162]

Table 2. Summary of the main advantages and disadvantages of different nanosystems, based on their composition.

Type of Nanosystem	Advantages	Disadvantages	Ref.
Drug nanocrystals 	▪ 100% drug (no carrier); ▪ Crystalline or amorphous structure (amorphous state offers advantages); ▪ Increased solubility and dissolution rate; ▪ Increased solubility; ▪ Increased adhesiveness to surface/cell membranes; ▪ Increased bioavailability of the drug.	▪ Generally needed to be stabilized by surface active agent; ▪ Possible nanotoxicity and side effects.	155
Organic/"Soft" NPs			
Polymeric-based NPs 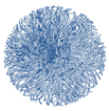	▪ Tunable size, shape, and surface properties, and easy functionalization; ▪ Biocompatibility; ▪ Good stability; ▪ Encapsulation of both hydrophilic and hydrophobic agents; ▪ Possible to use stimuli-responsive polymers; ▪ Drug release in a controlled and sustained manner; ▪ Promote humoral and cellular responses.	▪ Difficult to scale-up; ▪ Difficult purification methods; ▪ Poor storage conditions.	163–168
Lipid-based NPs 	▪ Ability to entrap hydrophobic and hydrophilic chemotherapeutic and imaging agents; ▪ Good stability in biological environments; ▪ Drug controllable release kinetics; ▪ Biocompatibility; ▪ Allow surface functionalization.	▪ Short-circulating properties (if not functionalized); ▪ Difficult purification methods; ▪ Poor encapsulation of hydrophilic drugs.	169–172
Inorganic/"Hard" NPs			
Mesoporous Silica/Silicon NPs 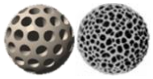	▪ High loading degree; ▪ High porosity; ▪ Allow surface functionalization; ▪ Biocompatibility; ▪ Biodegradability; ▪ Intrinsic adjuvant property.	▪ Short circulation time (if not functionalized); ▪ Poor stability in physiologic conditions.	173–177
Gold NPs 	▪ Bioinert; ▪ Tunable size and shape, and it can be functionalized with drugs and other ligands; ▪ Easy penetration and accumulation at the tumor sites; ▪ Optical properties (for photothermal therapy and photoimaging).	▪ Nonbiodegradable; ▪ Long-term toxicity.	178–180
Iron oxide NPs 	▪ Chemically inert; ▪ Low toxicity; ▪ Easy tunable surface properties and functionalization; ▪ Superparamagnetic behavior (for magnetic resonance imaging); ▪ Hyperthermia agents; ▪ Contrast agents for computed tomography.	▪ Limited colloidal stability (if their surface is not coated); ▪ High opsonization by macrophages.	181–183
Carbon nanotubes 	▪ Unique structures; ▪ Easy functionalization; ▪ Large surface area; ▪ Optical properties (for photothermal therapy and photodynamic therapy).	▪ Long-term cytotoxicity (if not functionalized); ▪ Lack of size uniformity during the synthesis process.	184–186
Biologically-derived NPs			
Cancer cell membrane-coated NPs 	▪ Long-circulating properties; ▪ Surface antigenic source; ▪ Stimulate both cell-mediated and humoral immune responses.	▪ Poor colloidal stability; ▪ Difficulty of loading proteins.	187–189

As for the surface charge, positively charged NPs tend to interact to a higher extent with the negatively charged components on the cell membrane *via* electrostatic attractions, compared to the negatively charged or neutral counterparts.[161,190] Furthermore, the cationic particles take advantage of their charge to facilitate endosomal escape through the 'proton sponge effect', avoiding the premature release or degradation of the payloads in the endosomal compartment.[191] However, cationic NPs can also cause cytotoxicity due to the increased mitochondrial and lysosomal damage, and disruption of plasma membrane integrity, compared to the anionic counterparts.[190] In order to overcome this limitation, zwitterionic NPs can be tailored to have a balance between negative and positive charges on their surface in order to accomplish simultaneously an enhanced cellular uptake and cytocompatibility.[161]

Although the spherical shape of NPs is the most widely studied morphology, different shapes have also been developed, such as cylinders or rod-like, prisms, worms, branched structures, or cubes, and their interaction with cells and the hemorheological dynamics have been evaluated.[156,161,192,193] During the circulation in the bloodstream, rod-like particles exhibit increased predisposition of NP–cell wall contact and possible extravasation through fenestrations in vasculature compared to the spherical counterparts.[156,194] In addition, the ratio between the height and width of the particle, *i.e.*, the aspect ratio, also affects the cellular uptake rate. Here, the rod-like particles (higher aspect ratio) exhibit an enhanced internalization than the spherical particles (low aspect ratio), because of the higher contact area with the cell membrane.[195]

Flexibility/elasticity, hydrophilicity/hydrophobicity and roughness are other parameters that influence the biodistribution, cell internalization, cytocompatibility and also immunogenicity of the NPs. In accordance with the film-tension model, NPs that are more hydrophobic than the cell surface tend to be more internalized than the ones that are more hydrophilic.[196] Conversely, hydrophobic NPs are more prone to aggregate and, consequently, removed from the bloodstream by the mononuclear phagocyte system (MPS).[197] In order to overcome this problem, the coating of the NP surface with PEG provides hydrophilicity and a hydrated cloud to the nanocarrier that sterically prevents the NPs from interacting with blood components and extends their circulating half-life.[198]

The elasticity of NPs, defined by Young's or elasticity modulus, can also regulate the circulation of the NPs in the bloodstream and, consequently, their accumulation at the tumor tissue due to the ability of the NPs to interact with the cell surface receptors and being internalized. In this regard, softer or low-flexible NPs are more taken-up by the cells than the stiffer or high-flexible NPs.[199,200] Additionally, the elasticity/flexibility can also direct the uptake mechanism of the NPs by the cells: (i) soft NPs are more internalized through micropinocytosis; (ii) an intermediate Young's modulus can drive the NPs to be internalized using multiple uptake mechanisms; and (iii) stiff particles are more likely taken-up *via* the clathrin-mediated mechanism.[201]

Overall, the different parameters of the NPs, and respective outcomes on the NP biodistribution and cellular uptake upon administration are summarized in **Table 3**.[16]

Table 3. Influence of the physicochemical properties of NPs in the biodistribution and cellular uptake. Adapted and reprinted with permission from ref.[16]

Parameter	Outcome
Size	
< 6 nm	▪ Undergo kidney by renal clearance after i.v. administration.
20–200 nm	▪ Increased extravasation through vascular fenestrations of tumors (*via* the EPR effect); ▪ Increased ability to cross the gastrointestinal barrier and blood-brain barrier; ▪ Optimal size for passive targeting of the injured left ventricle.
> 200 nm	▪ Increased entrapment within the liver and spleen.
2–5 μm	▪ Accumulation in the lungs.
Charge	
Anionic	▪ Moderated circulating half-life.
Neutral	▪ Moderated circulating half-life.
Zwitterionic	▪ Moderated circulating half-life.
Cationic	▪ Rapid clearance from circulation; ▪ Higher interaction with the negatively charged cell membranes; ▪ Facilitated endosomal escape *via* 'proton sponge effect'.
Shape	
Spherical	▪ Induce less cytotoxicity, compared to the fiber-shaped particles.
Rod-like	▪ Prolonged circulation time, compared to the spherical NPs; ▪ Improved ability to marginate and drift towards the vessel walls, increasing their interaction with the endothelial cells and consequent extravasation through the vasculature.
Discoidal	▪ Increased tendency for the NP–cell wall interaction and potential extravasation through the vascular fenestrations.
Chemistry	
Hydrophilicity	▪ Prolonged circulating half-life.
Hydrophobicity	▪ Increased cellular uptake; ▪ Induce more cytotoxicity than the hydrophilic surfaces.
Flexibility/Elasticity	▪ Higher internalization of softer particles by different cell lines, compared with the stiffer particles.
Roughness	▪ Improved loading capacity of therapeutics; ▪ Enhanced cellular uptake.

2.3 Biological barriers encountered by nanomedicines

Generally, nanomedicines come across several biological barriers upon administration, before they reach the tumor, after which they experience other obstacles at cellular and intracellular level.[12] By understanding the physiology and architecture of the tumors (*e.g.*, density and extracellular matrix organization), other properties of nanomedicines can be tailored to increase their accumulation in the tumor site, including passive targeting (driven by the EPR effect), active targeting of nanomedicines decorated with targeting ligands, and also the use of stimuli-responsive materials that allow the release of the therapeutic cargos at a specific site under certain stimulus.[145,202,203] Additionally, the nanomedicines can be modified to decrease the protein adsorption after administration and, therefore, prevent their opsonization and rapid clearance from the blood stream.[145] These different approaches will be addressed in the following sections.

2.3.1 Protein corona formation, opsonization and clearance of nanomedicines

Besides the red blood cells, the bloodstream contains plenty of small molecules, such as proteins, peptides, lipids, sugars and complexes of these molecules. When NPs reach the bloodstream upon administration, the NP surface can be covered by the abovementioned molecules, which will modulate the NP interaction with the different tissues and alter their fate.[204] This adsorption of biomolecules (usually small proteins) onto the NP surface is a phenomenon known as “protein corona” formation, which was first proposed in 2007 and derived from the concept of “protein adsorption” in different materials initially described in the 1950s and 1960s.[205–208] The protein corona can be defined by the existence of two distinct layers adsorbed onto the NP surface: (i) the “hard corona” constituted by proteins with high affinity that may be irreversibly bound onto the NP surface, and (ii) a “soft corona” composed by a second protein layer with low affinity to the chemical moieties on the NP surface that are adhered through reversible interactions.[204,209] Among other important parameters, the formation of the protein corona will alter the original NPs composition, leading to the reduction in their stealth effect, targeting ability of the NPs to recognize specific receptors in the target tissue, and consequent reduction in cell internalization, which then translates into a poor therapeutic efficiency of their cargos.[208,210] Additionally, the opsonin molecules (*e.g.*, proteins, immunoglobulin (Ig) G or complement factors) present in the bloodstream can also bind to the NP surface, which leads to the recognition, phagocytosis and clearance of the NPs from the systemic circulation by the macrophages of the MPS, usually liver Kupffer cells and splenic macrophages, a process known as opsonization.[197,211,212] The circulation time of the NPs in the bloodstream is also dependent on the nature of the molecules that bind to the NP surface. When high amounts of dysopsonins (*i.e.*, molecules that slow down the phagocytosis process, such as apolipoproteins and albumin) are part of the protein corona, the NPs are retained in the blood circulation for longer times than the ones with opsonin proteins in their surface.[213,214]

The interaction of proteins with NPs will also depend on the physicochemical properties of the NPs, including the composition, size, hydrophobicity, surface charge and chemistry, and shape, but also on the characteristics of the physiological environment in which the NPs are exposed, such as the composition, pH, and temperature of the media, the duration of exposure, as well as the dynamic shear stresses in the body.[210,214] Therefore, modulating the surface properties of the NPs by coating them with stealth polymers, such as PEG or polyvinylpyrrolidone (PVP), can prevent the NPs from aggregation and opsonization, and help to escape from the MPS.[215,216] Consequently, there is an increased circulation time of the NPs in the bloodstream and improved delivery of their therapeutic compounds to the target tissue.[214] Besides the reduced protein adsorption, PEGylation also allows the NPs to adsorb distinct proteins that were found to be necessary for the stealth effect and prevent non-specific cellular uptake of the PEGylated NPs, such as apolipoprotein J.[217,218] In addition, parameters such as the molecular weight, length, conformation, and the density of PEG on the NP surface affect the circulation time in the bloodstream.[219] For example, increasing the molecular weight of the PEG used to cover the NP surface leads to an increase in the circulation time and decrease on the protein adsorption onto the NP surface.[220,221]

Although the protein corona formation was initially seen as an obstacle that interferes with the NP stability and prevents NPs to reach their target tissue, this phenomenon is now seen as a tool to modify the NP surface in order to develop nanomedicines with better therapeutic effect and diagnosis ability. More recently, the concept of the protein corona has been evolved to the one of “biomolecule corona”, which also contains several types of

biomolecules that are part of the corona, and this is explored for targeting, diagnosis and also drug delivery purposes.[208]

2.3.2 Extravasation and accumulation of nanomedicines at the tumor

Nanomedicines can be tuned and benefit from different strategies in order to increase their accumulation in the tumor site, and also the therapeutic efficiency of their payloads. These approaches are generally divided into passive and/or active targeting of nanomedicines, and the use of stimuli-responsive materials that allow the release of the payloads upon a certain internal or external trigger (**Figure 5**).[14,222]

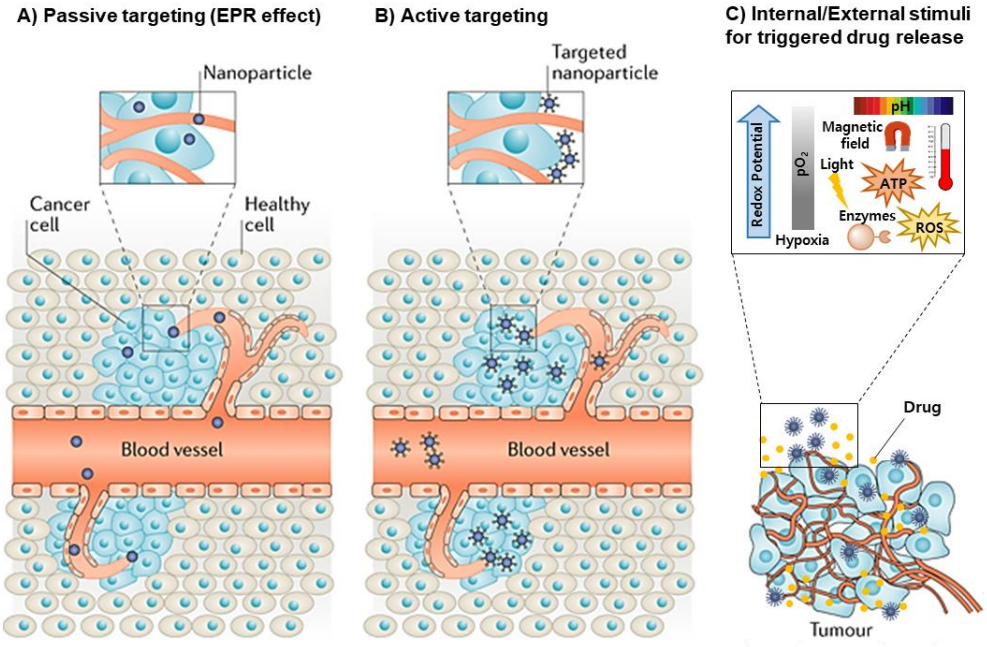

Figure 5. Mechanisms/approaches to deliver chemotherapeutics into tumors: **A)** Passive targeting that exploit the EPR effect mediated through leaky tumor vessels; **B)** active targeting of nanoparticles functionalized targeting ligands that specifically bind to receptors on the tumor cell's surface; and **C)** use of stimuli-responsive materials that release the chemotherapeutic upon an external or internal stimuli. Copyright © 2019 Nature Publishing Group. Adapted and reprinted with permission from ref.[222]

Enhanced permeability and retention effect in passive targeting

The EPR effect was first described in 1986 by Matsumura and Maeda,[223] and it is based on the pathophysiological and anatomical characteristics of some solid tumors and their microenvironment compared to the healthy tissues, which allows a preferential accumulation of the nanomedicines in the tumor.[224,225] The passive targeting of NPs is based on the EPR effect, along with the modifications on the NP surface to prolong the circulation time in the bloodstream.[135] The EPR effect on the passive targeting of NPs is due to the abnormal and large fenestrations in the blood vessels present in the TME, usually between 100 and 780 nm, that allows the extravasation of nanomaterials with sizes up to several hundreds of nanometers. Additionally, the extensive angiogenesis and lack of lymphatic drainage also promote the

retention of nanomedicines in the tumor vicinity.[224,225] The density of the extracellular matrix components in the TME, such as hyaluronic acid and collagen, can also limit the penetration of the NPs from the blood vessels deep into the tumor tissue. The TME is also composed by stromal cells, which include pericytes, fibroblasts, endothelial cells, macrophages, dendritic cells, among other immune cells, that also affect to the EPR effect and limit the diffusion of NPs into to tumor cells.[14,224] Moreover, there are some other challenges regarding the heterogeneity within and between the different types of solid tumors, such as: (i) the dimensions in the vasculature fenestrations can change with the tumor location (*i.e.*, primary tumor *versus* metastases); (ii) distinct vessel structures within a single tumor type; and (iii) the extent of macrophage infiltration and the activity of the MPS that can vary within and between tumors.[226,227] Additionally, the EPR effect does not direct the end result upon *in vivo* administration of nanomedicines. The events after the delivery of NPs or macromolecules to tumor tissues through the EPR effect also control the true therapeutic outcome.[149] The development of a next-generation of nanomedicines with targeting ligands and/or stimuli-responsive materials is needed to overcome the abovementioned issues and improve the accumulation of the nanomedicines at the tumor tissue.

Active targeting strategies

A second generation of nanomedicines has emerged to improve the properties of the NPs and overcome the limitations of the EPR effect and complement the passive targeting of NPs. For that, the nanosystems can be decorated with targeting ligands that allow the NPs to bind specifically to a certain cell receptor after extravasation, increasing their cell internalization and, consequently, improving the efficacy of the therapeutic compounds while minimizing their side effects.[9,17,18] Generally, targeting approaches take advantage of the differential expression of certain receptors between healthy and tumor cells. The most commonly used ligands are proteins, antibodies, peptides, nucleic acids (aptamers), polysaccharides (hyaluronic acid), among other small molecules.[228–230] The NP surface can be functionalized with the different targeting moieties using different approaches, such as chemical/covalent conjugation or physical adsorption on the NPs after the preparation, or linked to the NP functional groups before the formation of the NPs.[17] Among all the biological ligands, peptides have been most widely used for actively targeting nanomedicines and delivering anticancer drugs to the tumor tissue.[231,232] Short tumor-penetrating peptides offer certain advantages over other targeting ligands, such as other small molecules and larger antibodies, including small size, high specificity and affinity, increased tissue penetration, easiness to synthesize, and non-immunogenic nature.[231,232] Tumor homing peptides are usually identified using a bacteriophage (phage) display, which is a technique that allows the screening of different peptides in order to design and select the peptide sequences that show higher affinity to the specific target and respective hydrophobic binding pocket.[232,233] Briefly, the phage display technique is a cyclic process that relies on the incubation of the purified target molecules with a randomized peptide sequences library displayed on bacteriophage capsids. Afterwards, non-specific peptides are washed away, allowing the selection of high affinity peptides displayed on the bacteriophages, which are then eluted, collected, and seeded on a plate to infect *E. coli*, before amplification and new cycle of selection. Up to five rounds of biopanning, *i.e.*, affinity selection, are needed in order to identify the peptides that bind to the target with high affinity.[233,234] This technique has allowed the discovery of a large number of tumor-homing peptides that have been used as tools for imaging and therapy.[235,236]

The most widely used peptide that specifically recognizes and extravasates through the endothelial cells of tumor blood vessels, and penetrate into the tumor tissue, is the iRGD (CRGDKGPDC). This peptide contains an integrin-binding RGD motif that specifically binds at a first stage to αv-integrins that are selectively expressed on several tumor cells, which then binds to the neuropilin-1 (NRP-1) receptor upon a proteolytic processing of the iRGD, improving the tumor penetration.[237] This class of tumor-penetrating peptides requires the C-terminal exposure of the C-end rule (CendR) motif (R/KXXR/K), which then binds to the CendR NRP-1 receptor. Other classes of tumor-penetrating peptides have also been identified by phage display, such as the smaller peptides constructed from tumor-homing motifs or CendR elements.[237] Although they offer a solution for the drug penetration issue into the tumors, these peptides have usually a very short half-life upon administration (few minutes). This can be explained by enzymatic degradation and rapid renal clearance and elimination into the urine.[237,238] One way to overcome this problem is to attach the peptides on the surface of drug-loaded NPs, with increased therapeutic efficiency of the payloads.[239,240] Additionally, the ligand density on the NP surface is an important parameter to achieve the most efficient delivery of the therapeutics, which can differ in *in vitro* and *in vivo* circumstances, mainly due to the abovementioned biological barriers.[241] It is expected that at a high ligand density, the chances of improved binding of NPs to the target are more likely to happen. However, the high ligand density can raise some issues, such as: (i) increased NP average size after functionalization can decrease the accumulation in the tumor through the EPR effect; (ii) high conjugation efficiencies of the targeting moieties can be responsible for the decreased stealth properties of the NPs due to the reduced presentation of antifouling agents at the NP surface, promoting their rapid clearance from the bloodstream; (iii) the steric hindrance derived from the presence of high ligand amounts can lead to a diminished binding of NPs to their target; and (iv) the binding of NPs to a high number of cell surface receptors can reduce the overall cell internalization.[241] Another aspect to consider is the nanomedicine stability to avoid premature drug release and degradation in the bloodstream, which can be improved by developing stimuli-responsive materials.

Stimuli-responsive approaches

This generation of nanomedicines relies on the use of stimuli-responsive materials to enhance even further the therapeutic efficacy and biological specificity of the therapeutic compounds, by releasing the drug upon exposure to a certain stimuli and, therefore, minimizing the systemic side effects of these compounds.[242,243] Different triggers can be used to promote the drug delivery in a temporal-, spatial-, and dosage-controlled manner, and these can be (i) endogenous stimuli, such as enzyme concentration, pH changes in the body compartments, and redox gradients; (ii) exogenous stimuli, including magnetic field, temperature variation, ultrasound intensity, and light pulses; and (iii) multi-stimuli triggered drug release.[135,243,244]

Regarding the endogenous triggers, the fact that some solid tumors exhibit a more acidic microenvironment (pH 5.5–7.2) than the physiological pH in the blood and healthy tissues (pH 7.2–7.4) can be exploited to deliver drugs specifically to a tumor tissue.[135,245] Different approaches can be done to develop pH-responsive nanomedicines for cancer therapy, such as pH-sensitive polymers that include histidine-, sulfonamide-, and tertiary amine-containing groups, or by including pH-sensitive chemical bonds that are stable at physiological pH but are hydrolyzed under the acidic TME conditions.[245–247] The differential redox potential in tumor cells compared to the healthy tissues is another approach to selectively deliver drugs to the tumor

cells. Generally, reductive agents, such as glutathione (GSH), are present in the TME at higher levels compared to normal cells, which can be used to develop redox-responsive nanosystems, containing disulfide bonds or other GSH-sensitive crosslinking agents that are more prone to be cleaved by GSH.[243,248] Enzyme-mediated drug release relies on the altered expression profile of certain enzymes, such as phospoholipases, glycosidases or matrix metalloproteinases. This controlled drug release can be mediated be the use of short peptide sequences that are prone to be cleaved by these enzymes, allowing a more effective drug accumulation in the tumor site.[249,250]

An example of exogenous stimuli-sensitive materials is a thermo-responsive nanosystem that benefits from an induced local hyperthermia in the tumor compared to the surrounding temperature, increasing the vascular permeability at the tumor tissue and allowing the drug release. Preferably, thermo-responsive materials should be designed so that their payloads are not released at body temperature (~37 °C), and delivered in the tumor at higher temperatures (~39–43 °C). There are a variety of nanosystems described in the literature that can be used for this purpose, including magnetic and superparamagnetic iron oxide NPs, gold NPs, and thermo-responsive polymers (*e.g.*, PNIPAAm) that are used to develop different types of NPs or hydrogels.[251,252] Magnetic-sensitive NPs can also enable the transport of the drug to the tumor tissue upon exposure to a permanent and/or alternating magnetic field. Iron oxide NPs, such as magnetite (Fe_3O_4) or maghemite (γ-Fe_2O_3), have been extensively exploited for the fabrication of these magnetically responsive systems, mainly due to their relatively low toxicity and high saturation magnetization, and they can also be loaded into a variety of colloidal nanosystems that will release the drug and become sensitive to the external magnetic field exposure.[253,254] Other non-invasive and effective strategies to spatiotemporally release the drugs and contrast agents at the tumor site are based on the use of ultrasound, or photo-responsive materials that can react to different wavelengths (*e.g.*, ultraviolet, visible, or near-infrared regions).[243,255]

Additionally, the combination of different stimuli-responsive approaches gives the possibility to integrate both imaging and therapeutic modalities into a single platform for theranostic applications, allowing the real-time monitoring and assessment of the *in vivo* therapeutic efficacy of the drugs.[135]

2.4 Nanotechnology and cancer immunotherapy

Cancer immunotherapy represents a prominent class of treatments that exploits and boosts the immune system to fight tumors, and it shows several advantages compared to the other conventional treatments: (i) allows the immune system to specifically target and recognize the cancer cells, minimizing the side effects on healthy cells; (ii) can eradicate residual diseased cells and metastasis by the immune system, reducing cancer recurrence; (iii) can prevent cancer recurrence by generating immune memory, and (iv) the administration of cancer vaccines allows a prophylactic action against tumor cells.[256] Generally, cancer immunotherapies are based on the lymphocyte activating cytokines (*e.g.*, interferon (IFN)-α and interleukin (IL)-2), immune checkpoint inhibitors (*e.g.*, anti-CTLA-4 and anti-programmed death-1 (anti-PD-1) monoclonal antibodies), adoptive cellular therapies (*e.g.*, *ex vivo* expansion of tumor infiltrating lymphocytes, or chimeric antigen receptor (CAR) T cell therapy), oncolytic viruses, and cancer vaccines.[222,256] Despite these improvements and innovations in cancer therapy, the use of immunotherapies still encounters some limitations related to their high cost, non-specific toxicity and lack of efficacy. Nanotechnology has appeared as a tool to

make immunotherapies less toxic and more effective, while facilitating the combination of current chemo- and immune-therapies for synergistic purposes.[257–260] More specifically, nanosystems have been extensively engineered either to act as adjuvants in cancer vaccines, or as delivery systems of antigens and adjuvants.[257,261] Nanocarriers present intrinsic advantages that enable their application in immunotherapy, including tunable size that allows the delivery of different compound to the lymphoid organs; the ability to carry antigens and adjuvants to mimic pathogens and increase their immunogenicity; and lastly the uptake of NPs by APCs leads to an increased cross presentation of antigens on major histocompatibility complex class I (MHC I) to the cytotoxic T cells (CTLs).[19]

Among other modalities, TAMs-based therapies have also emerged as a promising target for cancer immunotherapy, due to the dominant presence of TAMs in the TME of certain tumors, and their phenotypic plasticity that enables their polarization towards an anti-tumor and pro-inflammatory subtype, also known as M1-like macrophages.[20,21]

2.4.1 Role of tumor associated macrophages in cancer progression

Solid tumors are composed by a complex environment that involves the interaction of tumor cells with the extracellular matrix components and stromal cells in the TME.[262] Among other stromal cells in the TME, macrophages represent one of the most common inflammatory cells that make-up the tumor mass, and they can contribute up to 50% of the overall tumor mass.[263] Regarding their origin, TAMs can be derived from circulating monocyte precursors that are recruited to the tumor tissue in response to the chemotactic signals released by cancer cells, or they may originate from bone-marrow progenitors that are later differentiated into mature cells after seeding in the tumor tissues and partially maintained *via* self-renewal.[263–265] Usually correlated with a poor outcome in most of the solid tumors, TAMs can be responsible for tumor growth and promotion by facilitating angiogenesis and immunosuppression, inhibiting T cell activation, tumor relapse after conventional cancer treatments, and tumor invasion and metastasis. This “communication” of TAMs with the tumor cells is done by releasing certain growth factors, cytokines and chemokines, in the TME that ultimately leads to the tumor progression and inhibits anti-tumor immune response (**Figure 6**).[263,266,267]

Macrophages are generally classified into 2 groups: (1) the “classically activated M1”, which typically requires IFN-γ and/or lipopolysaccharide (LPS) for their polarization, and (2) the “alternatively activated M2” that involves the stimulation with IL-4 and/or IL-13. After their differentiation, they can be distinguished by the changes in gene and cell surface markers expression, and also by the consequent activation of different signaling pathways.[263,268] On one hand, TAMs in progressing tumors present an immunosuppressive phenotype that resemble the “alternatively activated M2”, which usually express distinctive cell surface markers, such as CD163, CD204, and mannose receptor (CD206), and lead to the increased production of anti-inflammatory signals, including IL-10 and transforming growth factor (TGF)-β, and also arginase 1 (ARG 1).[266,269] On the other hand, TAMs with an anti-tumor phenotype resemble M1-like (or “classically activated”) macrophages, which are characterized by the expression of MHC II, CD68, CD80, and CD86 cell surface markers, the release of pro-inflammatory cytokines, including IL-12, IL-1β, IL-6 and tumor necrosis factor (TNF)-α, and production of inducible nitric oxide synthase (iNOS, NOS2).[263,269,270]

Although this is an oversimplification of the complexity of the different phenotypes and composition of TAMs, which can fluctuate between tumor stage and type of cancer, this

plasticity property of the macrophages that are able to go from a pro-tumor phenotype to an anti-tumor phenotype has been recently explored as a therapeutic target in cancer therapy.[20]

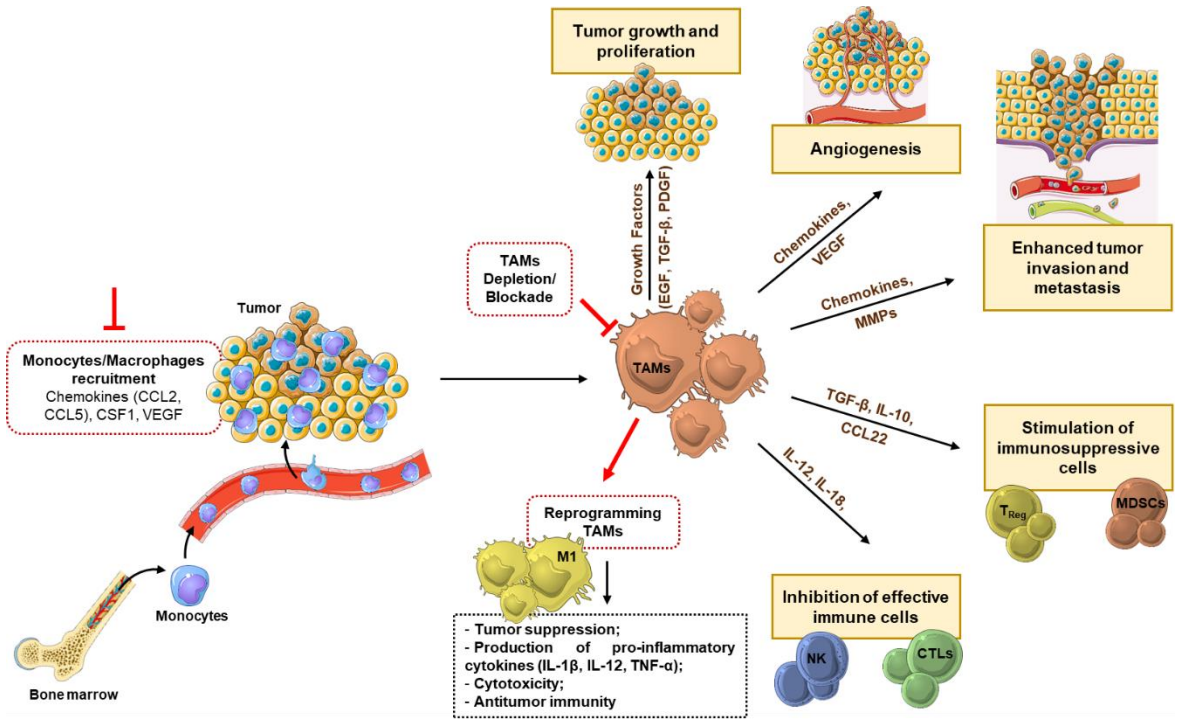

Figure 6. Role of M2-like TAMs in tumor progression, invasion and metastasis and possible therapeutic targets/options (red lines).

2.4.2 Tumor associated macrophages as a therapeutic target

As a result of the reasons previously explained, TAMs have become an interesting therapeutic target in cancer therapy, and the emerging therapeutic strategies are: (i) inhibition of the monocytes/macrophages recruitment to the tumor tissue; (ii) blockade or depletion of TAMs; and (iii) repolarization of TAMs from their pro-tumor M2-like phenotype to an anti-tumor M1-like phenotype (**Figure 6**).[20,271–273]

The first mentioned strategy is to block the monocyte infiltration into the tumor tissue, which is usually done through the secretion of chemoattractant signals by the TME, such as colony-stimulating factor 1 (CSF-1, or M-CSF), VEGF, CCL2 and CCL5.[20,263,274] The release of CSF-1 is responsible for controlling the proliferation, differentiation, survival and recruitment of monocytes and macrophages, and blocking the CSF-1 receptor signaling pathway leads to a decreased accumulation of immunosuppressive and pro-tumorigenic M2-like macrophages at the tumor.[275,276] The CCL2 is one of the main responsible for recruiting classical monocytes from bone marrow to bloodstream, because CC-chemokine receptor 2^+ monocytes are the main precursors of M2-polarized TAMs and, therefore, the CCL2-CCR2 signaling inhibits the recruitment of inflammatory monocytes and prevents metastasis in vivo.[277]

Another approach is to selectively eliminate or deplete TAMs at the tumor tissue in order to trigger their apoptosis and, consequently, block the signal network that leads to the tumor growth. Different drugs can induce TAMs apoptosis and delay the tumor progression, but this approach usually brings severe side effects (*e.g.,* bacterial infections), by systemically depleting other macrophages and other immunoprotective cells.[20,263]

One way to circumvent the drawback of TAMs depletion therapies is to take advantage of the macrophage plasticity, and use therapeutic modalities that revert their anti-tumor M2-like phenotype towards a tumoricidal M1-like phenotype of TAMs after manipulating the environmental stimuli.[20,263,272,273,278]

An overview of the current drugs and their respective targets used in the TAMs-based therapeutic approaches are presented in **Table 4**. Additionally, different nanoparticulate systems have been engineered to carry these drugs and effectively target them to the TAMs at the tumor site, or then to "take a ride" using macrophages as drug delivery carriers, because of their ability to migrate and infiltrate into tumors.[279,280]

Table 4. Some examples of the TAMs-based therapeutic strategies.

Therapeutic approach	Drugs (Type)	Target	Ref.
Inhibition of monocytes recruitment	Carlumab (Antibody)	CCL2	281
	PF-04136309 (Small molecule)	CCR2	282
TAMs depletion	Alendronate (Bisphosphonate)	Phagocytes	283
	Trabectedin (Small molecule)	Caspase 8	284
	AMG 820 (Antibody)	CSF-1R	285
	RG7155 (Antibody)	CSF-1R	275
	JNJ-40346527 (Small molecule)	CSF-1R	286
Reprogramming M2-like towards an M1-like TAMs	CC-90002 (Ab)	CD47	287
	HPA063793 (Antibody)	MARCO	288
	CP-870,893 (Agonistic Antibody)	CD40	289
	R848 (Small molecule)	TLR 7/8	290
	IMO-2055 (Small molecule)	TLR 9	291

As these strategies to target TAMs act upstream of T cell responses, they might be useful to complement other immunotherapies that regulate T cells, such as the use of immune checkpoint inhibitors or adoptive cell therapies.[267] Therefore, the combination of different anticancer treatment modalities simultaneously seems to improve the therapeutic efficiency and overcome the limitations of the individualized treatments.

3 Aims of the study

Nanosystems with different compositions have been widely studied for cancer therapy and imaging during the past decades. The main aim of this thesis was to evaluate the potential of underexplored and innovative LNPs as platforms to deliver therapeutics for enhanced cancer therapy. In addition, the cytocompatibility and cell-NP interactions of bare and functionalized nanoparticles were investigated, and their biodistribution and therapeutic efficacy were also assessed.

More specifically, the objectives of the present study were:

1. To investigate the cytocompatibility of different lignin-based NPs towards several cell lines, and to evaluate the drug loading ability into the LNPs (**I**).

2. To prepare carboxylated lignin to allow the preparation of LNPs functionalized with polymers and different targeting ligands (**II**).

3. To surface modify the LNPs with DSS peptide and compare the cellular internalization with iRGD-functionalized LNPs, using 2D- and 3D-cell culture models (**III**).

4. To functionalize resiquimod (R848)-loaded LNPs with mUNO peptide to target M2 macrophages, to study their tumor-homing ability, and to assess repolarization of M2-like phenotype into M1-like macrophages for synergetic chemotherapy (**IV**).

4 Experimental

This section summarizes the experimental methods used for the studies described in the thesis. Detailed description of the materials, instrumentation and methods can be found in the original publications (**I–IV**). The preparation of oleic acid-coated Fe_3O_4 NPs and iron(III)-complexed LNPs (**I**) was done at Aalto University, Finland. The *in vivo* studies presented in publication **IV** were performed in collaboration with the Laboratory of Cancer Biology, University of Tartu, Estonia.

The detailed description of the materials used in this thesis can be found in the materials and methods section of each original publication.

4.1 Synthesis of carboxylated lignin (II–IV)

The carboxylation reaction of the original lignin was done to increase the amount of carboxyl groups on the lignin for further conjugation reactions. In this thesis, the softwood kraft lignin used was obtained using two different technologies: LignoBoost™ and UPM BioPiva™.

4.1.1 Carboxylation of LignoBoost™ softwood kraft lignin (II)

Here, 100 mg of LignoBoost™ softwood kraft lignin was reacted with succinic anhydride (100 mg, 21.2 mmol) and 4-dimethylaminopyridine (DMAP; 20 mg, 4.1 mmol) in 40 mL of THF at room temperature (RT) for 48 h.[292] The reaction mixture was dialyzed against MilliQ-water, using a dialysis bag (Spectra/Por® 1 Standard RC Dry Dialysis Tubing, 12–14 kDa, Spectrum Labs, CA, USA) for 48 h to remove the unreacted reagents, changing the water periodically. Finally, the carboxylated lignin was freeze-dried and characterized with a Fourier transform infrared (FTIR) spectroscopy instrument (Vertex 70, Bruker, MA, USA), using a horizontal attenuated total reflectance (ATR) accessory (MIRacle, PIKE Technologies, WI, USA). The ATR–FTIR spectra were recorded at RT between 4000 and 650 cm^{-1} with a resolution of 4 cm^{-1}, using an OPUS 5.5 software.

4.1.2 Carboxylation and characterization of BioPiva™ softwood kraft lignin (III, IV)

Using a similar process as described above, 100 mg of BioPiva™ softwood kraft lignin was reacted with different mass ratios of succinic anhydride (as detailed in publication **III**), in the presence of 20 mg of DMAP as catalyst, in a final volume of 40 mL of THF at RT for 48 h.[292] The same procedure for purification and freeze-drying of the carboxylated polymers was followed as described in the *Section 4.2.1*. All the carboxylated lignin polymers were posteriorly characterized with a ATR–FTIR. Additionally, aliphatic hydroxyl, phenolic hydroxyl, and carboxyl groups of original softwood kraft lignin and carboxylated lignin polymers were analyzed by phosphorus-31 nuclear magnetic resonance (^{31}P NMR) spectroscopy (**III**), as described earlier, except that now the sample weight was 25 mg and 15 sec relaxation time was used in the inverse-gated pulse sequence.[103]

After optimization of the carboxylation conditions, the carboxylated lignin polymer (4:1) was selected to prepare the LNPs in the subsequent studies (**III, IV**).

4.2 Preparation and characterization of lignin nanoparticles (LNPs) (I-IV)

4.2.1 Preparation of LNPs (I-IV)

All the LNPs were prepared using the solvent exchange method, as described previously.[76] The LNPs were formed during the dialysis process (Spectra/Por® 1 Standard RC Dry Dialysis Tubing, 12–14 kDa, Spectrum Labs, USA), in which the lignin molecules self-assembled into colloidal spheres as the THF was gradually replaced by deionized water.

Pure LNPs (pLNPs, **I**) were prepared after dissolving 1 mg of original LignoBoost™ softwood kraft lignin in 1 mL of THF, and dialyzed against water periodically replaced under slow stirring in a fume hood for 24 h.

The synthesis of iron(III)-complexed LNPs (Fe-LNPs, **I**) was performed, as described elsewhere.[78] Briefly, a condensation reaction was performed by adding a solution $Fe(OiPr)_3$ in THF into a solution of lignin in THF. A hydrolysis reaction was done after the addition of an equal volume of 1 wt-% water in THF to a solution of Fe:lignin in THF. Finally, the particles were solvent exchanged in a dialysis tube against deionized water that was periodically replaced during 24 h to minimize the residual solvents.

A mixture containing 50:50 w/w of lignin solution and oleic acid-coated Fe_3O_4 NPs in THF was prepared for the synthesis of Fe_3O_4-infused LNPs (Fe_3O_4-LNPs, **I**), and placed into a dialysis bag for solvent exchange against deionized water for 24 h.

The carboxylated LNPs were prepared after dissolving 1 mg of carboxylated LignoBoost™ softwood kraft lignin (**II**) or carboxylated BioPiva™ softwood kraft lignin (**III, IV**) with 1 mL of THF, and the mixture was dialyzed against deionized water during 24 h.

4.2.2 Surface functionalization of carboxylated LNPs (II–IV)

*4.2.2.1 Preparation of PEG-poly(histidine) and CPP-functionalized LNPs (**II**)*

The conjugation reaction between the –COOH groups of carboxylated lignin and $–NH_2$ groups of NH_2-PEG-Poly(histidine) (PHIS) and CPP was performed in 10 mM of 2-(*N*-morpholino)ethanesulfonic acid (MES) buffer (pH 5.5), using 1-ethyl-3-(3-dimethylaminopropyl)carbodiimide and *N*-hydroxysuccinimide (EDC/NHS) coupling chemistry.[293,294] After optimization of the conjugation conditions, to obtain LNPs conjugated with a 9 amino acid cell penetrating peptide (CPP), 1 mg of LNPs were activated using 400 µL of 10 mM of MES buffer (pH 5.5), with 2.5 µL of EDC (20 mM) and 2.3 mg of NHS (50 mM), and stirred at 500 rpm for 1 h at RT. After removing the excess of EDC/NHS, the LNPs were resuspended with 1 mL 1× Hanks' balanced salt solution with 4-(2-hydroxyethyl)-1-piperazineethanesulfonic acid (HBSS–HEPES, pH 7.4), containing 0.2 mg of CPP (mass ratio CPP:LNPs of 1:5), and the mixture was reacted for 4 h under stirring, at RT. Finally, the CPP-functionalized LNPs (LNPs-CPP) were centrifuged and washed twice with HBSS–HEPES (pH 7.4).

In order to obtain the NH_2-PEG-PHIS-modified LNPs (LNPs-PEG-PHIS), 1 mg of LNPs was activated for 1 h, using the same conditions, as described above. After removing the excess of EDC/NHS, the LNPs were resuspended with 1 mL of 10 mM of MES buffer (pH 5.5), containing 0.1 mg of NH_2-PEG-PHIS (mass ratio 1:10 of copolymer:LNPs). The mixture was stirred at RT for 4 h, and then washed twice with HBSS–HEPES (pH 7.4) to purify the

functionalized LNPs. Afterwards, the same protocol used to prepare the LNPs-CPP was employed to react the LNPs-PEG-PHIS with the CPP in order to obtain LNPs-PEG-PHIS-CPP.

*4.2.2.2 Preparation of iRGD and DSS-modified LNPs (**III**)*

The conjugation reaction between the –COOH groups of LNPs and $–NH_2$ groups of dentin phosphophoryn-derived peptide (DSS) and iRGD peptide was also performed using EDC/NHS coupling chemistry. The molar amount of peptides used for the reaction was chosen taking into consideration the molecular weight of the peptides (*see* the in original publication), and after optimization of the conjugation conditions. The –COOH groups on the LNPs were activated by reacting 1 mg of LNPs in 400 µL of 100 mM of MES buffer (pH 5.5), containing 5 µL of EDC (40 mM) and 4.6 mg of NHS (100 mM), and the mixture was stirred for 1 h at RT in the dark. After removing the excess of EDC/NHS, the LNPs were resuspended with 500 µL of PBS (pH 7.4), containing 250 µM of the DSS and iRGD and reacted during for 4 h, to prepare LNPs-DSS and LNPs-iRGD, respectively. Afterwards, the peptide-functionalized LNPs were centrifuged, and washed twice with MilliQ-water.

*4.2.2.3 Preparation of mUNO-modified LNPs (**IV**)*

Using the same coupling chemistry described above, 3 mg of LNPs dispersed in 1.2 mL of 10 mM of MES buffer (pH 5.5), containing 4.5 µL of EDC (12.8 mM) and 1.2 mg of NHS (8.7 mM) were reacted for 1 h, and then 15 mg of maleimide-PEG-amine (Mal-PEG-NH_2, 2K) in 1.5 mL of 10 mM of MES buffer (pH 7) was reacting with the activated LNPs, during 3 h, in order to obtain the LNPs-PEG-Mal. Afterwards, the maleimide group on the LNPs-PEG-Mal was used to react with the free cysteine groups on 5(6)-carboxyfluorescein (FAM)-Ahx-Cys-NH_2 (FAM) and FAM-Ahx-CSPGAK-COOH (mUNO) in MilliQ-water for 2 h at RT, rendering LNPs-P-FAM and LNPs-P-F-mUNO, respectively.

4.2.3 Characterization of LNPs (I–IV)

All the LNPs were characterized for their average particle size (Z-average), polydispersity index (PDI) and average zeta (ζ)-potential (surface charge) by dynamic light scattering (DLS) and electrophoretic light scattering (ELS), respectively, using a Malvern Zetasizer Nano ZS instrument (Malvern Instruments Ltd, UK). In addition, the LNPs were visualized by transmission electron microscopy (TEM), using a Jeol JEM-1400 (Jeol Ltd., Tokyo, Japan), with an acceleration voltage of 80 kV, in order to characterize their morphology and confirm their size distribution.

To study the magnetic properties of Fe_3O_4-LNPs (**I**), the NP suspension was placed in a 6-well plate, and the photos were taken while the particles were guided and accumulated around the magnetic field. Additionally, the hysteresis loop of oleic acid-coated Fe_3O_4 NPs and Fe_3O_4-LNPs was measured using a vibrating sample magnetometer (MicroMag 3900 VSM; Lake Shore Cryotronics, Inc.). The obtained magnetic moment (A m^2) *versus* the applied magnetic field (T) was normalized with the amount of Fe_3O_4 in the sample, and corrected for dia/paramagnetic component in order to determine the magnetization value (A m^2 kg^{-1}).

After drying the samples overnight, the functional groups present on the LNP surface of the bare and functionalized LNPs (**II, III**) were evaluated by ATR–FTIR.

The dissolution experiments of the LNPs were done to evaluate the long-term stability of the LNPs prepared with the different carboxylated lignin polymers at physiological conditions (**III**). For that, 50, 200 and 500 µg/mL of LNPs were incubated in Dulbecco's phosphate buffer saline (PBS, pH 7.4), at 37 °C. Then, 100 µL of LNP suspension were withdrawn at determined time points (4, 6, 24, 48 and 72 h), and centrifuged at 16100 *g* for 5 min. Finally, the absorbance of the supernatant at λ = 380 nm was measured by UV-Vis spectroscopy, using a Varioskan Flash plate reader (Thermo Fisher Scientific Inc., USA), and the dissolution of the LNPs was calculated taking into account the absorbance of the dissolved LNPs in EtOH, which corresponded to the maximum absorbance that the supernatant would have if the LNPs were totally dissolved at physiological conditions.

4.2.4 Human plasma stability of LNPs (I, II)

Plasma proteins can interact with the LNPs and affect their fate upon administration. In order to evaluate the interaction of the LNPs with the plasma components, the size and ζ-potential changes of the LNPs were determined after incubation of the LNP suspensions (200–300 µg/mL) with 100% human plasma (**I, II**) at 37 °C during 90–120 min. All the experiments were performed in triplicates.

4.2.5 Drug loading (I–IV)

In order to assess the ability of pLNPs to load cytotoxic compounds with different solubility properties in aqueous media, three different compounds were used as models in the first study (**I**): poorly water-soluble drug (sorafenib, SFN) and cytotoxic agent (1-methyl-8-(propan-2-yl)-4-(trifluoromethyl)-3*H*-benzo[*cd*]azulen-3-one, benzazulene, BZL), and a water-soluble drug (capecitabine, CAP). For that, 2 mg of original LignoBoost™ softwood kraft lignin was dissolved with 1 mL of THF containing 200 µg of drug (mass ratio 1:10 of drug:lignin), and then dialyzed against MilliQ-water during 24 h.

Based on the results obtained in this first study, BZL was selected as the model drug for the following two studies (**II, III**). Here, the carboxylated LignoBoost™ softwood kraft lignin (**II**) or carboxylated BioPiva™ softwood kraft lignin (**III**) was dissolved in a THF solution, containing the BZL, in a mass ratio BZL:lignin of 1:5 (**II**) or 1:3 (**III**). For the publication **IV,** resiquimod (R848) was loaded into LNPs after mixing carboxylated BioPiva™ softwood kraft lignin and R848 in THF, in a mass ratio of 1:10 of R848:lignin. All these solutions were placed inside the dialysis membrane, and the drug-loaded LNPs were formed during the dialysis process against deionized water (periodically replaced) under slow stirring in a fume hood for 24 h in order to remove THF and free compound.

The conjugation reactions of drug-loaded LNPs with the different polymers/targeting ligands were performed according to the procedure described in the *Section 4.2.2.* for the empty LNPs. The average drug loading degree (LD) into the LNPs was determined by immersing the drug-loaded LNPs in EtOH under vigorous stirring. Afterwards, the solution was centrifuged at 16100 *g* for 5 min, and the supernatant was collected in order to determine the drug concentration detected by UV with a high-performance liquid chromatography (HPLC; Agilent 1100 series, Agilent Technologies, USA). The experimental conditions used for quantification of the drug loaded into the LNPs are detailed in the original manuscripts.

4.2.6 *In vitro* drug release studies (I–III)

BZL and SFN (**I**) were used to evaluate the *in vitro* release profiles of free drug and drug-loaded pLNPs in two different buffers: HBSS–MES (pH 5.5) and HBSS–HEPES (pH 7.4). For that, 100 µg of pure drug and 200 µg of drug-loaded pLNPs were immersed in 200 mL and 25 mL of release media, respectively. As for the second study (**II**), the *in vitro* release profiles of free BZL and BZL-loaded LNPs was evaluated in HBSS–MES (pH 5.5) and HBSS–HEPES (pH 7.4), supplemented with 2% (v/v) Tween-80, and 70 µg of free BZL and 250 µg of BZL-loaded LNPs were immersed in 60 mL and 20 mL of release media, respectively. In publication **III**, the release profiles of free BZL and BZL-loaded NPs were studied in HBSS–MES (pH 5.5) and HBSS–HEPES (pH 7.4), supplemented with 10% (v/v) fetal bovine serum (FBS) after 4h, where 30 µg of free BZL and 100 µg of BZL-loaded LNPs were immersed in 10 mL of release media. In all the release experiments, the samples were stirred at 150 rpm at 37 °C. At scheduled time intervals (up to 24 h), 200 µL of the release media were withdrawn and the same volume of fresh preheated release medium was added, keeping the releasing volume constant. After spinning down the samples at 16100 *g* for 5 min, the supernatants were collected, and analyzed in HPLC to determine the amount of drug released by measuring the drug concentration, using the same HPLC methods as in the determination of the drug loading degree.

In addition, the morphology of the drug-pLNPs during the release was evaluated and compared to the drug-loaded pLNPs before the release (**I**). For that, 200 µL of release medium were collected after 4 and 24 h incubation of 1 mg of drug-pLNPs in 1 mL of HBSS–MES (pH 5.5) and HBSS–HEPES (pH 7.4), stirred at 150 rpm at 37 °C. The samples were placed on a carbon-coated copper grid, and air-dried before analysis and visualization using TEM, and the average size, PDI and ζ-potential values of the same samples were also characterized by DLS.

4.3 *In vitro* cell-based studies (I–IV)

4.3.1 Cell lines and cell culturing (I–IV)

Human umbilical vein (EA.hy926), human mammary carcinoma (MDA-MB-231 and MCF-7), mouse mammary carcinoma (4T1), human lung carcinoma (A549), human prostate cancer (PC3-MM2), and human colorectal adenocarcinoma (Caco-2) cell lines were all obtained from American Type Culture Collection (ATCC, USA). The EA.hy926, MCF-7, PC3-MM2, A549 and Caco-2 cells were grown in Dulbecco's Modified Eagle Medium (DMEM), and the MDA-MB-231 and 4T1 cells were cultured in Roswell Park Memorial Institute (RPMI), supplemented with 10% inactivated fetal bovine serum (HIFBS), 1% of non-essential amino acid (NEAA), 1% of L-glutamine (200 mM) and 1% of penicillin (100 IU/mL)-streptomycin (100 mg/mL) in 75 cm^2 flasks. EA.hy926 medium was also supplemented with 1% of sodium pyruvate (100 mM). All the cells were kept in an incubator (BB 16 gas incubator, Heraeus Instruments GmbH) at 37 °C, 5% CO_2 and 95% relative humidity. The cell culturing medium was changed every 2–3 days, and the subculturing was performed when the cells reached 80% of confluence, until the moment of the experiments. For this, the cells were harvested with 0.25% (v/v) trypsin-PBS-ethylenediamine tetraacetic acid (EDTA) solution.

4.3.2 Isolation of murine bone marrow derived macrophages and differentiation into macrophages (IV)

Both femur and tibia bones were isolated from female 6-8 week old BALB/c mice, and the bones were cut and flushed with cold PBS to a Petri dish, assisted with a 21G needle. Subsequently, the cell suspension was centrifuged at 500 *g* for 5 min, suspended with 1 mL of Ammonium-Chloride-Potassium (ACK) lysing buffer for 2 min to remove the red blood cells, and then 9 mL of PBS were added before centrifugation (500 *g* for 5 min).[295] The bone marrow derived macrophages (BMDMs) were then redispersed with RPMI (supplemented with 10% of HIFBS, 1% of L-glutamine and 1% of penicillin-streptomycin), and 300000 cells/mL were seeded in Petri dishes in 10 mL of RPMI, containing 20 ng/mL of macrophage colony-stimulating factor (M-CSF). After 3 days, 5 mL of cell culturing medium were exchanged by 5 mL of fresh RPMI, supplemented with 20 ng/mL of M-CSF. Resting macrophages (so-called M0 macrophages) were obtained at day 6, and seeded in 48-well plates at a density of 250000 cells per well in 0.5 mL of RPMI supplemented either with 20 ng/mL of IL-4 to differentiate into M2-like macrophages, or 10 ng/mL of IFN-γ and 100 ng/mL LPS to obtain M1 macrophages. They were incubated at 37 °C for 48 h before the flow cytometry analysis to evaluate the expression of the cell surface markers, as detailed in the experimental section of publication **IV**.

4.3.3 Preparation of three-dimensional cell culturing model (III)

The three-dimensional (3D) spheroids were prepared using the 3D bioprinting method (**III**). Initially, 1.5 mL of cells (PC3-MM2, MDA-MB-231 and A549) were seeded in 6-well plates at a density of 400000 cells per well, and allowed to attach overnight. Then, 50 µL of NanoShuttle™-PL were added to the cells for their magnetization, and incubated for 8–10 h. Afterwards, the cells were washed twice with PBS buffer (pH 7.4) and plated in ultra-low attachment 96-well plates at a density of 5000–7000 cells per well, which was then placed over a 96-well spheroid magnetic drive. The cells within the solution aggregated in the well plate upon the magnetic field, and the spheroids were cultured for 2 days.

4.3.4 Cytocompatibility studies (I-IV)

For the two-dimensional (2D) cell culturing model, 15000–30000 cells per well were seeded in 96-well plates, and allowed to attach overnight. Afterwards, 100 µL of LNPs' suspensions (**I-IV**) and free R848 (**IV**) in HBSS–HEPES buffer (**I**) or cell media (**II-IV**) at different concentrations (25–500 µg/mL) were added to each well and the plates were incubated at 37 °C for 24 h. Incubations with HBSS–HEPES buffer (**I**) or cell media (**II-IV**) and 1% (v/v) Triton X-100 were used as a positive and negative controls, respectively. After equilibrating the plates at RT, and washing the wells with 100 µL of HBSS–HEPES buffer, 50 µL of CellTiter-Glo® were added to 50 µL of HBSS–HEPES (pH 7.4) in each well. Finally, after stabilizing the plates the luminescence was measured using a Varioskan plate reader. The number of viable cells in culture was quantified based on the amount of ATP produced by metabolically active cells.[175,239]

For the 3D cell culturing model (**III**), after gently transferring the cell spheroids to 96-well plates, 50 µL of LNPs suspensions were mixed with 50 µL of NanoLuc® luciferase and MT Cell

Viability Substrate in complete cell culture medium, so that the final concentration of NPs was ranging from 10 to 100 µg/mL, followed by the incubation at 37 °C, up to 48 h. The RealTime-Glo™ MT Cell Viability Assay is a nonlytic, homogeneous and bioluminescent assay that allows to quantify the luminescence in order to determine the cell viability, using a Varioskan plate reader. The number of viable cells was assessed by measuring the reducing potential of cells, and thus metabolism.[296]

4.3.5 Detection of reactive oxygen species (I, IV)

The fluorescent 2',7'-dichlorofluorescein (DCF) probe was used to measure the generation of hydrogen peroxide (H_2O_2), which results from the oxidation of a non-fluorescent compound 2',7'-dichlorodihydrofluorescein diacetate ($DCFH_2$-DA) by the intracellular reactive oxygen species (ROS). Briefly, 15000–30000 cells per well (MDA-MB-231, MCF-7, PC3-MM2, Caco-2 and EA.hy926 cells, for publication **I**; and M2-like macrophages, for publication **IV**, were seeded in 96-well plates, and incubated overnight at 37 °C. Afterwards, 100 µL of LNP suspensions (25 to 250 µg/mL) in HBSS–HEPES buffer (**I**) or cell media (**IV**) were incubated with the cells, for 24 h (**I**) or 30 min (followed by 48 h incubation with cell medium, **IV**) at 37 °C. After that, 100 µL of $DCFH_2$-DA (10 µM) in HBSS–HEPES buffer was incubated with the cells for 1h, at 37 °C. Cells treated with 0.25% of H_2O_2 (**I**) or cell media (**IV**) were used as controls. Afterwards, the fluorescence of DCF (λ_{ex} = 498 nm; λ_{em} = 522 nm) was measured with Varioskan plate reader.

4.3.6 Hemotoxicity (I)

Red blood cells (RBCs) were isolated from human blood of anonymous donors at the Finnish Red Cross Blood Service. For the isolation, the blood sample was diluted with of PBS (pH 7.4) (50:50 v/v) and this solution was further layered in Ficoll-Paque PLUS. The mixture was centrifuged (1500 *g* for 40 min) to split up the RBCs from the serum. After extensive washing, the RBCs were diluted with PBS (pH 7.4) to obtain a 5% RBCs suspension. Afterwards, 60 µL of this suspension was incubated with 240 µL of LNPs' suspensions (25 and 250 µg/mL) in PBS (pH 7.4), up to 12 h at 37 °C. In addition, PBS (pH 7.4) and MilliQ-water were used as negative and positive controls, respectively. At defined time points (1, 4, 6 and 12 h), 100 µL of the RBC-LNP suspensions were centrifuged (3 min, 16100 *g*), and the absorbance intensity of hemoglobin at 577 nm in the supernatants was measured, using Varioskan plate reader.

4.3.7 Antiproliferative experiments (I-III)

The *in vitro* antiproliferative effect of the pure BZL and BZL-loaded LNPs was assessed using the same protocol and the ATP-based cell viability assay described in the *Section 4.3.4*, for both 2D cell (**I-III**) and 3D (**III**) cell culturing models. Different concentrations of BZL-loaded LNPs (5–250 µg/mL) in HBSS–HEPES buffer (**I**) or cell media (**II, III**) were incubated with the different cell lines. Additionally, similar concentrations of pure BZL (1.6–68.2 µM) in HBSS–HEPES buffer (**I**), or pure BZL previously dissolved with 1–3% of EtOH in cell media (**II, III**), were added to each well. A specific control for pure BZL was also added with the same amount of ethanol used in the BZL-loaded LNP dilutions.

4.3.8 Cellular association and internalization studies (III)

For the cell-LNP interaction studies (**III**), the LNPs were loaded with a highly stable fluorescent dye 4-[4-(dihexadecylamino)styryl]-*N*-methylpyridinium iodide (DiA), in a mass ratio of 1:100 (DiA:LNPs), and the conjugation reactions with the peptides were done as described for the empty LNPs (*see Section 4.2.2.2*). Afterwards, the interactions between the cells and DiA-loaded LNPs, LNPs-iRGD and LNPs-DSS were qualitatively and quantitatively evaluated by confocal microscopy and flow cytometry, respectively.

For the 2D cell culturing model, 50000 cells per well were seeded in Lab-Tek 8-chamber slides for confocal microscopy, and allowed to attach overnight. After removing the medium, 100 µg/mL of LNP suspensions in PBS (pH 7.4) were added to the cells and incubated for 3 h at 37 °C. The cells were washed, and the plasma membranes were stained by adding CellMask Red (5 µg/mL) for 3 min at 37 °C. After washing, the cells were fixed using 4% paraformaldehyde (PFA) for 10 min at RT, and the nuclei were stained by adding 4',6-diamidino-2-phenylindole (DAPI, 2.8 µg/mL) for 5 min at 37 °C. The localization of NPs was observed with a Leica SP5 inverted confocal microscope (Leica Microsystems), using a 63×/1.2-0.6 oil immersion objective.

For flow cytometry analysis, 100000 cells per well were seeded in 24-well plates and allowed to attach during overnight incubation. Afterwards, 100 µg/mL of LNP suspensions were added to the cells for 3 h at 37 °C. After removing the non-adherent LNPs, the cells were harvested with Gibco™ Versene Solution for 5 min (0.48 mM), incubated with trypan blue (0.005% v/v) during 4 min, and washed with PBS (pH 7.4) before analysis. Flow cytometry was performed with a LSR II flow cytometer (BD Biosciences, USA), and a FACS Diva software, and the data was analyzed using FlowJo V10 software after collecting 20000 events.

Regarding the 3D cell culturing model, the 3D tumor spheroids (prepared as described in the *Section 4.3.3*) were incubated with 100 µg/mL of LNP suspension in PBS (pH 7.4), at 37 °C for 3 h. For confocal microscopy, the spheroids were further fixed with 4% of PFA (24 h at 37 °C), and the nuclei were stained with DAPI (2.8 µg/mL, for 24 h at 37 °C). Finally, the cell spheroids were transferred to a Lab-Tek 8-chamber to observe the localization of NPs with a Leica SP5 inverted confocal microscope, using a 20× objective. As for flow cytometry analysis, the spheroids were harvested with trypsin-PBS-EDTA during 5 min, after incubation with the LNP suspensions. Then, the cells were incubated with trypan blue (0.005% v/v, 4 min) and washed with PBS–EDTA (pH 7.4) before flow cytometry analysis, using a LSR II flow cytometer (BD Biosciences, USA), and FlowJo V10 software to analyze the data after collecting 5000 events.

4.3.9 Immunostainings and cellular association studies (IV)

For flow cytometry, M0 macrophages were seeded in 48-well plates at density of 250000 cells per well (500 µL of RPMI supplemented with 20 ng/mL of IL-4), for 48 h at 37 °C, to obtain M2-like macrophages. Then, LNPs-P-FAM and LNPs-P-F-mUNO (200 µg/mL) were added to each well and incubated at 37 °C for 10, 30 and 60 min in complete medium. Afterwards, the macrophages were detached using PBS–EDTA (5 mM), during 15 min on ice. The cells were centrifuged at 500 *g* during 5 min, and resuspended in PBS–EDTA for flow cytometry analysis (LSR II flow cytometer, BD Biosciences, USA), and the data was analyzed using FlowJo V10 software after collecting at least 10000 events.

As for confocal microscopy, the M0 macrophages were seeded in Lab-Tek 8-chamber slides, at density of 75000 cells per well (in 200 µL of RPMI supplemented with 20 ng/mL of IL-4), during 48 h, at 37 °C. Next, 200 µg/mL of LNPs-P-FAM and LNPs-P-F-mUNO in complete cell culturing medium were added to the M2-like macrophages for 10, 30 and 60 min, at 37 °C. Afterwards, the cells were fixed with 4% of PFA (10 min at RT), permeabilized with 0.2% (v/v) Triton-X in PBS (10 min at RT), and incubated with 5% of blocking buffer (5% Bovine serum albumin (BSA) + 5% FBS + 5% Donkey serum in PBS + 0.05% (v/v) Tween-20 (PBS-T)), for 1 h at RT, in order to avoid unspecific binding of the antibodies. Next, rat anti-mouse CD206 and rabbit anti-mouse FAM in 1% of blocking buffer (1% BSA + 1% FBS + 1% Donkey serum in PBS-T) were incubated with the cells for 1 h at RT, followed by the incubation with the secondary antibodies anti-rat Alexa Fluor 647 and anti-rabbit Alexa Fluor 488 in 1% of blocking buffer (35 min at RT). Finally, the nuclei were stained with DAPI (5 min, at RT). The samples were observed with a Leica SP5 inverted confocal microscope, using a 63×/1.2–0.6 oil immersion objective. The colocalization of the LNP FAM signal with $CD206^+$ M2-like macrophages (Pearson's coefficient) was quantified using ImageJ software.

4.3.10 Repolarization study (IV)

The expression of specific cell surface markers on macrophages was evaluated after *in vitro* repolarization of M2-like macrophages. For that, after the differentiation of M0 macrophages into M2-like macrophages, 200 µg/mL of R848-loaded LNPs and a similar concentration of free R848 (1 µg/mL) in complete media were added to each well, for 30 min at 37 °C, and further replaced by fresh complete medium for 48 h at 37 °C. After detaching the macrophages, the samples were incubated with TruStain FcX™ anti-mouse CD16/32 antibody (BioLegend, USA) in cold PBS during 10 min at 4 °C, before staining with anti-mouse Alexa Fluor 488–CD86 and APC–CD206 (BioLegend, USA) in cold PBS for 20 min at 4 ºC. Finally, the samples were analyzed by flow cytometry (LSR II flow cytometer, BD Biosciences, USA), and the data was analyzed by FlowJo V10 software after collecting at least 10000 events.

4.4 *In vivo* studies (IV)

The nanoplatform developed in the publication **IV** was assessed *in vivo*, using a murine breast adenocarcinoma model (4T1 tumor-bearing mice), for combination with chemotherapy.

4.4.1 Experimental model and ethical permit (IV)

The 4T1 tumors were inoculated according to protocols approved by the Estonian Ministry of Agriculture, Committee of Animal Experimentation (permit #48). Here, female 8-12 week old Balb/c mice (in-house bred) were inoculated orthotopically by injecting 1 million 4T1 cells (in 50 µL of PBS) in the 5th mammary fat pad. The tumor dimensions were measured using a digital caliper, and the tumor volumes were calculated using the formula $[(W^2 \times L)/2]$, in which W is the tumor width and L is the tumor length.

4.4.2 Homing study and *ex vivo* biodistribution (IV)

The tumor homing of R848-loaded LNPs-P-FAM and LNPs-P-F-mUNO was evaluated 6 days after tumor inoculation, when the tumors reached a volume of *ca.* 50 mm^3. Then, 250 µg of LNPs were dispersed in 200 µL of 5.4% glucose, and administered intraperitoneally. After 3 h, mice were sacrificed by i.p. administration of 500 µL of 2.5% Avertin and cervical dislocation, and the tumors and organs were excised, washed with PBS and fixed with 4% of PFA (4 °C, overnight). The tissues were further placed in 15% of sucrose (in PBS, overnight), and later in 30% of sucrose. Afterwards, the tissue blocks were frozen, cut into 20 µm-thick sections (Leica cryotome), and placed onto glass slides before storing at −20 °C.

For immunostaining purposes, the tissue sections were incubated with rat anti-mouse CD206 and rabbit anti-FAM as the primary antibodies, and then with anti-rat Alexa Fluor 546 and anti-rabbit Alexa Fluor 647 as the secondary antibodies. Finally, the nuclei were stained with DAPI, and the sections were mounted and sealed, before imaging with a Zeiss LSM-710 confocal microscope (Germany). The total FAM signal and colocalization (Pearson's coefficient) of both FAM and CD206 channels were estimated using ImageJ software.

4.4.3 Therapeutic studies and *ex vivo* immunological profile of tumor cells (IV)

On day 6 post-inoculation (p.i.), mice were randomly distributed into 5 treatment groups (n = 6) according to their tumor volume average (46–48 mm^3). Then, mice were initially treated three times with Vinblastine alone (1 mg/kg, in 500 µL of PBS, i.p.) or vinblastine combined with free R848 or R848@LNPs (0.125 mg/kg, in 200 µL of 5.4% glucose, i.p.), followed by two isolated administrations of the R848 (free form or nanoformulated). Detailed description of the treatment schedule is provided in the original publication. The mice weights and tumor volumes were measured every other day. On day 18 of p.i., all mice were sacrificed, and their tumors were weighed.

Tumor tissues from each treatment group (n = 3) were further used for evaluating the immunological profile of the cells. For that, single cell suspensions were obtained after gentle disruption of the tumor tissues using cell strainers (70 µm mesh) with a syringe plunger. Samples were then cryopreserved at −80 °C (in FBS containing 5% of DMSO) until the day of analysis. After thawing, the samples were incubated with ACK lysis buffer, and the cells were incubated with TruStain FcX™ anti-mouse CD16/32 antibody (10 min, at RT), followed by staining with antibody combinations (20 min, at 4 °C). After washing twice with PBS, the samples were analyzed by flow cytometry (BD Accuri 6 plus, BD Biosciences, USA), and the data analysis was performed using FlowJo V10 software, after collecting 500000 events. The antibodies to stain specific markers on the cell surface were the following: macrophages (PE-F4/80, APC-CD206 and Alexa Fluor 488-CD86), T cells (Alexa Fluor 488-CD3 and APC-CD8), and DCs (FITC-CD11c and APC-CD86).

4.5 Statistical analysis (I-IV)

The measured values are expressed by mean ± standard deviation (s.d.). Statistical analysis was performed using the GraphPad Prism (GraphPad software Inc., CA, USA), and set at the probabilities of $*p < 0.05$, $**p < 0.01$ and $***p < 0.001$. Detailed description of the statistical methods used to analyze the data can be found in the experimental section of each publication.

5 Results and Discussion

Lignin has recently emerged as a novel starting material for different biomedical applications. In this thesis, the potential use of this underexplored material was evaluated for drug delivery purposes. In particular, different LNP platforms were evaluated in terms of their biocompatibility towards various cell lines, the ability to load different therapeutic compounds, and to modify their surface with different ligands. Lastly, the potential ability of LNPs to deliver an immunomodulatory compound for synergistic effect with chemotherapy was assessed also *in vivo*.

5.1 *In vitro* evaluation of LNPs for drug delivery and enhanced antiproliferative effect in cancer cells (I)

The physicochemical properties of NPs play an important role in the biodistribution, internalization, pharmacokinetics and safety of the chemotherapeutics. The NP's biological fate can be influenced by structural and physical parameters, such as size, shape, surface charge and chemistry.[9,297] The main aim of this study was to fabricate and characterize LNPs in terms of their physicochemical properties, biocompatibility, stability in biorelevant media, and ability to load and release different cytotoxic compounds.

5.1.1 Characterization of LNPs

Here, three different lignin-based NPs were prepared by solvent exchange, intended to be used as vehicles to deliver anticancer agents: pure LNPs (pLNPs); iron(III)-complexed LNPs (Fe-LNPs), and oleic acid-coated Fe_3O_4-loaded lignin NPs (Fe_3O_4-LNPs), as shown in **Figure 7A**. These nanosystems were firstly characterized by DLS (**Table 5**) and TEM (**Figure 7B-D**), in order to assess their average size diameter and distribution, surface charge, and also their morphology.

Table 5. Physicochemical characterization of the fabricated lignin-based NPs.

Sample	Size (nm)	PDI	ζ-Potential (mV)
pLNPs	220 ± 10	0.19 ± 0.02	−44 ± 4
Fe-LNPs	160 ± 21	0.09 ± 0.01	−43 ± 2
Fe_3O_4-LNPs	464 ± 15	0.22 ± 0.06	−42 ± 1

With the exception of the Fe_3O_4-LNPs, both pLNPs and Fe-LNPs showed an average size that fulfils the requirements for a passive targeting of NPs to the tumor tissue, in response to the large fenestrations and discontinuous endothelium present in the blood vessels in the vicinity of the tumor tissue.[298] Additionally, the PDI values lower than 0.25 are indicative of a moderately uniform size polydispersity of the prepared LNPs. Regarding the surface charge, all the LNPs presented ζ-potential values of *ca.* −43 mV, driven by the negatively charged functional groups on the LNP surface (in water) that promote the formation of electrical double layers, which then stabilize the NP dispersion through electrostatic repulsion.[76] Additionally, TEM images revealed symmetric and spherically shaped LNPs (**Figure 7B-D**), which can be

ascribed to the good solubility of the lignin polymer in THF and poor solubility in water that allowed a proper interaction between the water and lignin in the course of the solvent exchange process.

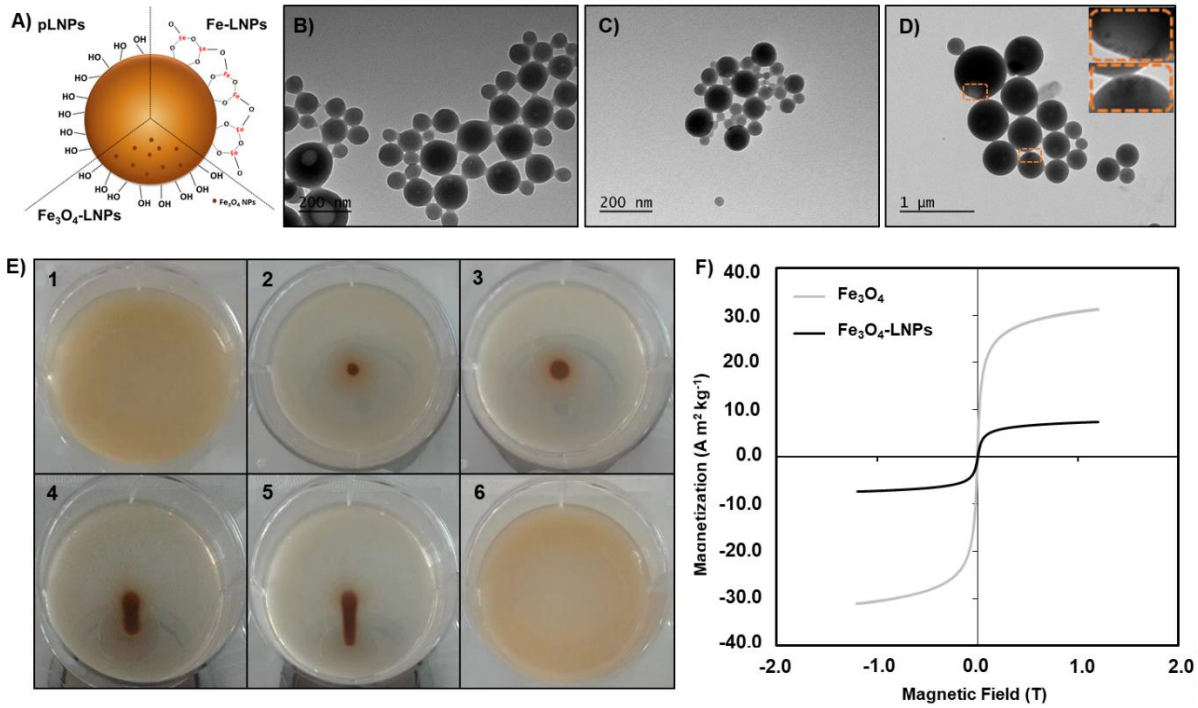

Figure 7. Schematic representation of the three types of LNPs evaluated in this study (**A**), TEM images of (**B**) pLNPs, (**C**) Fe-LNPs and (**D**) Fe_3O_4-LNPs and magnification of the Fe_3O_4 NPs inside the LNPs. Characterization of the magnetic behavior of the Fe_3O_4-LNPs (**E**); Sequence of images showing the magnetic-guided behavior of Fe_3O_4-LNPs in suspension: **1**, Fe_3O_4-LNPs in suspension; **2** and **3**, Fe_3O_4-LNPs accumulated around the magnetic field after placing the magnet under the well; **4** and **5**, Fe_3O_4-LNPs guided by the magnetic field after moving the magnet under the well; **6**, Fe_3O_4-LNPs redispersed by gently shaking. (**F**) Hysteresis loop of Fe_3O_4 NPs and Fe_3O_4-LNPs. Copyright © 2017 Elsevier B.V. Adapted and reprinted with permission from publication (**I**).

The magnetic properties of the Fe_3O_4-LNPs were also evaluated (**Figure 7E** and **7F**). For an efficient loading of the Fe_3O_4 NPs into LNPs, the Fe_3O_4 NPs were coated with oleic acid, which provided hydrophobicity and also better dispersibility for the magnetic NPs,[299] allowing the Fe_3O_4 NPs to be loaded during the solvent exchange process from THF to water. As shown in the TEM image (**Figure 7D**), around 10 nm diameter Fe_3O_4 NPs can be found loaded inside the LNPs, suggesting a successful formation of Fe_3O_4-LNPs, and the loading degree of Fe_3O_4 NPs was *ca.* 9.9 wt-%. The magnetic behavior of the Fe_3O_4-LNPs was assessed after magnetically guiding the NP suspension (**Figure 7E**). It was possible to observe that the Fe_3O_4-LNPs accumulated and translocated to another place of the well, towards the point where the magnetic field applied was higher, and they were easily redispersed by gently shaking.

Classified as superparamagnetic iron oxide NPs, the Fe_3O_4 NPs also exhibited a superparamagnetic behavior shown by NP sizes of about 10–20 nm. These NPs reached saturation magnetization after the application of an external magnetic field. After removing the magnetic field, the NPs retained no residual magnetic interaction and they could be easily

redispersed.[300] In this way, the hysteresis loop given by the magnetization *versus* magnetic field curves of Fe_3O_4 NPs and Fe_3O_4-LNPs allowed to evaluate the magnetic properties (**Figure 7F**). The results indicated that the superparamagnetic properties of the Fe_3O_4-LNPs were retained after loading of the Fe_3O_4 NPs into LNPs, despite of the decrease on the saturation magnetization values after the loading of the Fe_3O_4 NPs, from 31 to 7 A m^2 kg^{-1}. The decrease in the saturation magnetization can be ascribed to the larger size of the Fe_3O_4-LNPs compared to the Fe_3O_4 NPs alone, a phenomenon that has been reported in the literature for other magnetic nanosystems.[301,302] Therefore, due to the superparamagnetism of the developed Fe_3O_4 NPs, they could be used as a delivery vehicle to a specific target in the body upon magnetic field exposure, for example for cancer diagnosis and therapy, and magnetic resonance imaging.[183,303]

Another aspect to take into consideration is the NP stability at physiological conditions and, therefore, the stability of the three types of LNPs were evaluated in PBS (pH 7.4) and in human plasma. Upon incubation with the PBS (**Figure 8A**), the sizes of the LNPs were constant over time and they did not form aggregates, indicating that the prepared LNPs presented a good colloidal stability. However, the sizes of LNPs were generally increased during the first minutes of incubation in human plasma (**Figure 8B**), indicating a certain degree of plasma protein adsorption onto the LNPs. Although the sizes slightly decreased over time, owing to the slow detachment of weakly interacting proteins from the hard protein corona layer on the LNP surface,[304] their final sizes after incubation with plasma were *ca.* 200 nm higher than their initial size. The grafting of hydrophilic polymers (*e.g.*, PEG) on the NP surface could minimize the protein corona formation, improving plasma stability and, consequently, increase the circulation time in the bloodstream upon *in vivo* administration.[219,305]

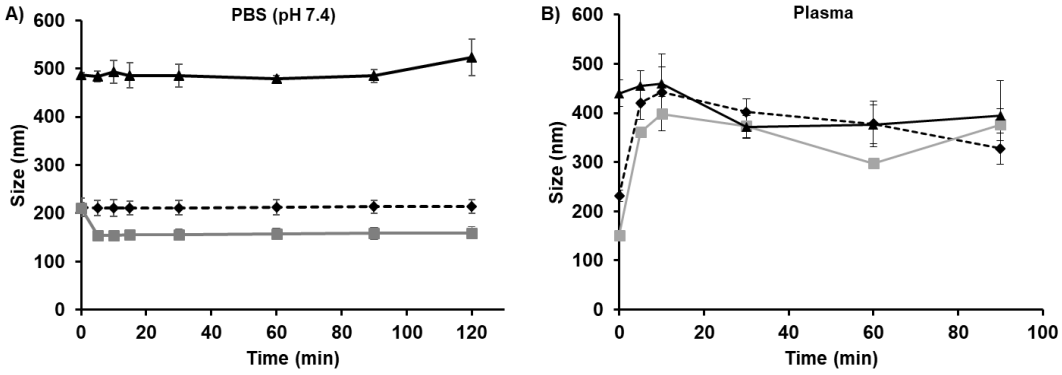

Figure 8. Stability of the LNPs in terms of average size, up to 2 h incubation at 37 °C in (**A**) PBS (pH 7.4), and (**B**) human plasma. Error bars represent mean ± s.d. (*n* = 3). Copyright © 2017 Elsevier B.V. Adapted and reprinted with permission from publication (**I**).

5.1.2 *In vitro* cytocompatibility studies

Although the three LNPs were prepared with the same starting material, different cell–NP interactions, biological activities (*e.g.*, ROS production), and NP-associated cytotoxicity could be observed in response to the different surface compositions (*e.g.*, presence of iron), aggregation behavior, and sizes.[304,306–308] Therefore, toxicological effects on the cells after exposition to the LNPs were investigated by evaluating the cell viability values in terms of ATP production (**Figure 9A–E**) and production of H_2O_2 (**Figure 9F–J**), as a function of the

concentration of the LNPs. Different cancer cell lines were selected in order to evaluate the potential application of these LNPs in the treatment of different types of cancer, such as breast (MDA-MB-231, MCF-7), prostate (PC3-MM2) and colorectal (Caco-2) cancers. Additionally, a non-tumor EA.hy926 endothelial cell line was also selected, because of the potential application of these LNPs for i.v. administration.

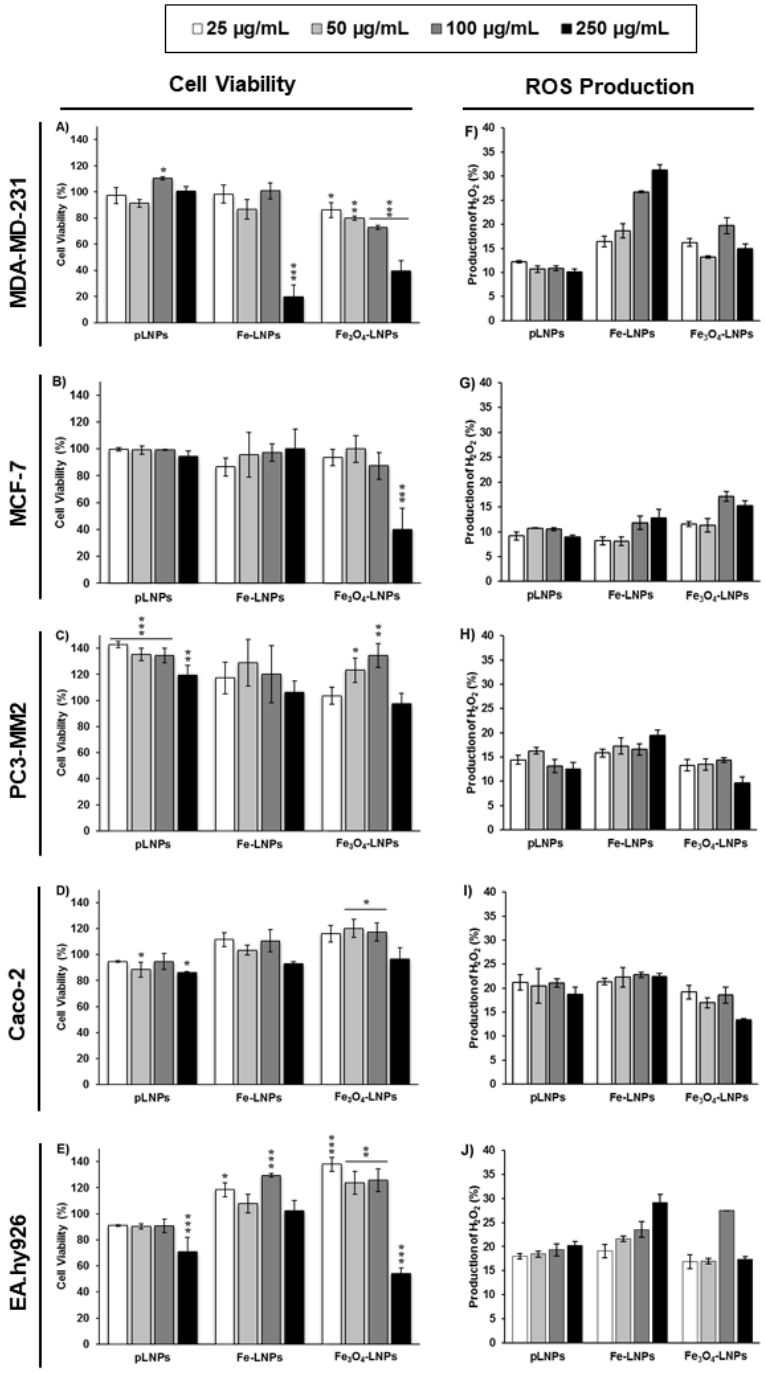

Figure 9. Cell viability of (**A**) MDA-MB-231, (**B**) MCF-7, (**C**) PC3-MM2, (**D**) Caco-2 and (**E**) EA.hy926 cell lines after incubation with pLNPs, Fe-LNPs and Fe_3O_4-LNPs at different concentrations for 24 h at 37 °C. The cell viability was determined using the CellTiter-Glo® luminescence assay and all data sets were compared to the positive control (HBSS–HEPES, pH 7.4). Evaluation of ROS production in (**F**) MDA-MB-231, (**G**) MCF-7, (**H**) PC3-MM2, (**I**) Caco-2 and (**J**) EA.hy926 cell lines after 24 h incubation at 37 °C with pLNPs, Fe-LNPs and

Fe_3O_4-LNPs at different concentrations. The ROS production was determined with a fluorescent $DCFH_2$-DA assay. All data sets were compared with the positive control (H_2O_2). Errors bars represent the mean ± s.d. ($n \geq 3$). The level of the significant differences was set at probabilities of $*p < 0.05$, $**p < 0.01$ and $***p < 0.001$. Copyright © 2017 Elsevier B.V. Adapted and reprinted with permission from publication (**I**).

Overall, all the tested concentrations of the three types of LNPs showed very good cytocompatibility at concentrations up to at least 100 µg/mL after 24 h of incubation, with more than 80% of cell viability values (**Figure 9A–E**). However, the Fe_3O_4-LNPs at concentration of 250 µg/mL showed an increased toxicity towards MDA-MB-231, MCF-7, and EA.hy926 cell lines, and the Fe-LNPs (250 µg/mL) were also toxic against MDA-MB-231 cells. This higher cytotoxicity of the NPs can be correlated with an increased production of H_2O_2 against the same cell lines (**Figure 9F–J**), after conversion into highly reactive superoxide or hydroxyl radicals by Fenton reaction, which is a process catalyzed by Fe^{2+}/Fe^{3+} ions.[308–310] Additionally, the presence of iron ions and iron oxide NPs can also affect the homeostasis of ROS inside the cells and the intracellular redox reactions, leading to the conversion of ROS into highly reactive superoxide or hydroxyl radicals, and consequent oxidative stress.[308–310] This effect can then lead to DNA damage, unregulated cell signaling, cytotoxicity, and finally apoptosis.[311,312]

In general, no significant cytotoxicity and intracellular ROS production was observed at LNP concentrations up to at least 100 µg/mL, after 24 h of incubation with the different cell lines.

5.1.3 Drug loading assessment and release studies

The potential of pLNPs to be used as a vehicle for drug delivery applications was further studied using three different drugs and cytotoxic agents with different solubility profiles: poorly water-soluble compounds (SFN and BZL), and water-soluble drug (CAP), were used as model drugs for loading into pLNPs during the solvent exchange process.

The loading degrees (LD) of the different drugs were quantified after completely releasing the drugs during the incubation of pLNPs with ethanol, which caused the dissolution of the lignin polymer (**Figure 10B**). This slight difference between the LD of BZL (8%) and SFN (7%) can be ascribed to the different molecular weight, chemical structures, and solubility characteristics of these drugs. As the BZL is more hydrophobic and smaller compared to SFN, it can be encapsulated more efficiently into the pLNPs than SFN. For the same reason, the SFN@pLNPs also showed a larger size than BZL@pLNPs, and the sizes of both the drug-loaded pLNPs were slightly higher compared to the empty pLNPs (**Figure 10A**). Moreover, the PDI values were lower than 0.25, and the surface charge of the drug-loaded pLNPs did not change significantly, suggesting that the pLNPs were still monodispersed even after the drug loading, and the drugs were successfully loaded and were not on the pLNP's surface. However, the solvent exchange method to prepare pLNPs did not allow the encapsulation of hydrophilic drugs, such as CAP (**Figure 10A** and **10B**). This suggests the potential of using pLNPs as a carrier for poorly water-soluble cytotoxic agents and drugs (*e.g.*, BZL and SFN).

The drug release profiles of BZL@pLNPs, SFN@pLNPs and free drugs were evaluated in two different aqueous buffers to mimic the tumor microenvironment or intracellular endosomes (pH 5.5, **Figure 10C**) and the physiological pH (pH 7.4, **Figure 10D**). Overall, the

drug-loaded pLNPs improved the drug dissolution rates at pH 5.5 and 7.4, because both pure BZL and SFN present very low solubilities in aqueous solutions (< 5% release after 24 h). However, the amount of SFN released from the pLNPs was slightly decreased after 24 h, which could be due to the instability and consequent precipitation of SFN in the aqueous solution. Therefore, the pLNPs could protect the hydrophobic drugs inside the nanostructure, while substantially improving the dissolution profiles.

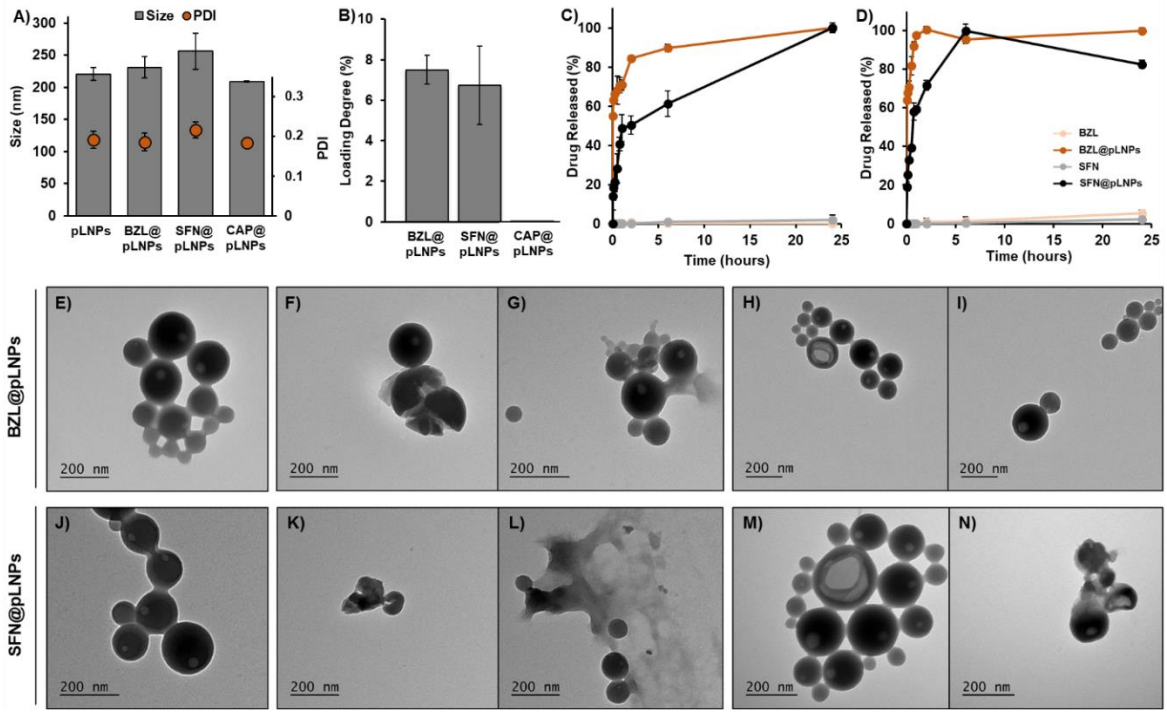

Figure 10. Characterization of the drug-loaded pLNPs: (**A**) Size, PDI, and ζ-potential, (**B**) loading degree and solubility kinetics of pure drugs and drug-loaded pLNPs in (**C**) HBSS–MES (pH 5.5) and (**D**) HBSS–HEPES (pH 7.4) at 150 rpm and 37 °C for 24 h. Results are presented as mean ± s.d. (*n* = 3). TEM pictures taken during the release study: (**E and J**) drug-loaded pLNPs, (**F and K**) drug-pLNPs after 4 h release at pH 5.5, (**G and L**) drug-pLNPs after 24 h release at pH 5.5, (**H and M**) drug-pLNPs after 4 h release at pH 7.4, and (**I and N**) drug-pLNPs after 24 h release at pH 7.4. Copyright © 2017 Elsevier B.V. Adapted and reprinted with permission from publication (**I**).

The morphology and size of the drug-loaded pLNPs before and during the release were evaluated with the aim to demonstrate reasoning for the release mechanism of both the drugs from the pLNPs (**Figure 10E-N**). First of all, the drug-loaded pLNPs were also spherically shaped as the empty pLNPs, indicating that the morphology did not change after drug loading. After incubation at pH 5.5 (**Figure 10F, G, K, L**), both the drug-loaded pLNPs showed some disintegration of the NPs, and possibly the formation of aggregates, as the sizes were increased from about 300 to 600 nm after 4 and 24 h of release, respectively. Regarding the incubation of drug-loaded pLNPs at pH 7.4 (**Figure 10H, I, M, N**), a less significant disintegration of the NPs was observed, and the size increases were smaller, from 300 to 400 nm after 4 and 24 h, respectively.

Overall, these observations suggested that the drug release from the pLNPs can be dictated by a diffusion mechanism through the lignin structure.

5.2 Functionalization of LNPs for pH-responsive delivery of a cytotoxic agent (II)

Different polymers have been employed to efficiently deliver the therapeutic compounds into a specific site of action.[313] In particular, the advantageous properties of PEG allow the PEGylated NPs to prolong their circulation time in the bloodstream, by avoiding opsonization and clearance by the MPS.[198,219] Additionally, the use of pH-responsive polymers (*e.g.*, PHIS) can trigger the drug release in response to the lower pH values of the TME (pH 5.5–6.8).[246,247] In this study, the original lignin polymer was subjected to a carboxylation reaction in order to increase the amount of carboxyl groups available for further conjugation reactions with different polymers/ligands. After characterization of the prepared nanosystems, the drug release profile of poorly-water soluble BZL-loaded LNPs was evaluated, and their *in vitro* antiproliferative effects in different cell lines studied.

5.2.1 Carboxylation and characterization of LNPs

The carboxylation of the lignin polymer was done by reacting the hydroxyl groups of the original lignin with succinic anhydride, with DMAP as a nucleophilic catalyst.[292] The potential mechanism for this reaction starts with the nucleophilic attack of DMAP on a carbonyl group of succinic anhydride that leads to the formation of a tetrahedral intermediate. This intermediate is more active than the original anhydride towards a further nucleophilic attack, and will react with the hydroxyl groups on lignin, originating another intermediate that will collapse to obtain the carboxylated lignin upon elimination of the pyridine group.[314] In the ATR–FTIR spectra in **Figure 11C** of the original lignin polymer and carboxylated LNPs (simply referred to as LNPs), shows the success of the carboxylation reaction. In addition to the typical bands attributed to the different functional groups on the lignin structure (*e.g.*, aromatic structure (1427–1512 cm^{-1}), carbonyl groups (1600 cm^{-1}), and alcohol and phenol –OH (3500–3100 cm^{-1})), the LNPs exhibited a stronger absorption band at about 1720 cm^{-1} compared to the original lignin. Apart from the contribution of the stretching vibrations of C=O derived from the ketone group positioned at β-location, which also appeared in the original lignin, this stronger absorption was mainly due to the stretching vibrations of C=O of the free –COOH groups.

Afterwards, water-dispersed LNPs prepared with the carboxylated lignin were also formed by solvent exchange process *via* dialysis. Therefore, a block copolymer NH_2-PEG-PHIS was attached to the LNP surface to provide the aforementioned PEGylation effect and a pH-responsive behavior of PHIS.[198,219,315] Additionally, the LNPs were also decorated with a CPP (polyarginine R9), a highly positively charged peptide that is known to enhance the translocation through the plasma membrane, which is negatively charged.[316] Regarding the characterization of the prepared LNPs, the average sizes of both CPP or PEG-PHIS-CPP-functionalized LNPs were slightly increased after the conjugation reaction, compared to the bare LNPs, and the PDI values remained below 0.25, suggesting a moderate polydispersity of all the prepared LNPs (**Figure 11A**). As for the surface charge, the ζ-potential values of the bare LNPs were negative (*ca.* −36 mV), due to the presence of free –COOH groups on the LNP surface (**Figure 11B**). However, the surface charge become positive after the surface modification of LNPs, because of the $–NH_2$ groups presented by both CPP and PHIS,

indicating that the functionalization of the LNPs with NH_2-PEG-PHIS and CPP was successfully accomplished.

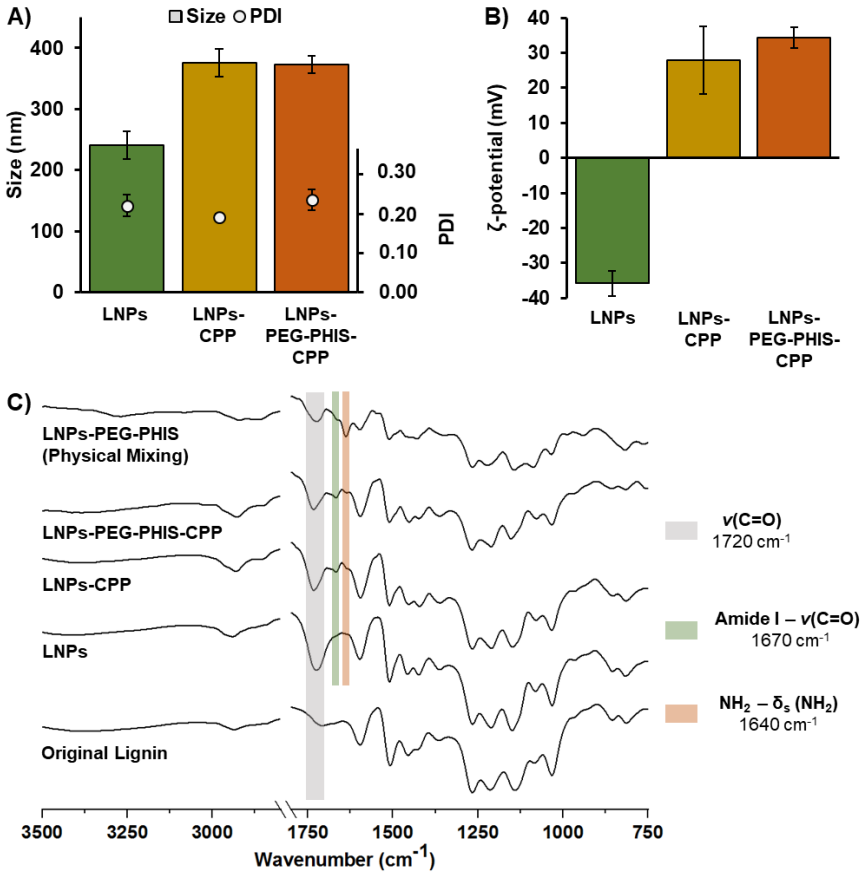

Figure 11. Characterization of carboxylated LNPs and functionalized carboxylated LNPs by (**A**) measuring their average size and PDI; (**B**) ζ-potential, and (**C**) ATR–FTIR spectroscopy. Error bars represent the mean ± s.d. ($n \geq 3$). Copyright © 2017 Future Science Group. Adapted and reprinted with permission from publication (**II**).

The ATR–FTIR spectra were also recorded to determine the functional groups present on the LNP surfaces, and to evaluate the differences between bare LNPs and modified-LNPs (**Figure 11C**). All the prepared LNPs presented an adsorption band at around 1720 cm^{-1}, due to the C=O stretching vibrations of the unconjugated –COOH groups. However, both the LNPs-CPP and LNPs-PEG-PHIS-CPP showed a characteristic band absorbing near 1670 cm^{-1}, ascribed to the C=O stretching vibrations of the amide bond (O=C–NH), with minor contributions from the out-of-phase C–N stretching vibration, the N–H in-plane bend and the C–C–N deformation.[317,318] At the same time, the intensity of the band at 1720 cm^{-1} for the functionalized LNPs was decreased compared to the bare LNPs, while a small band at *ca.* 1640 cm^{-1} emerged, which could be due to the free $–NH_2$ groups present on both CPP and PHIS.[319] The ATR–FTIR spectrum of a physical mixture, composed by LNPs and PEG-PHIS mixed together, was also determined to compare with the chemically modified LNPs-PEG-PHIS-CPP. Here, the absorption bands were slightly different from those observed for the LNPs, but the characteristic band corresponding to the amide bond formation (1670 cm^{-1}) was reduced, while a stronger band at *ca.*1640 cm^{-1} was present due to the free $–NH_2$ groups on the PHIS.

Concluding, the ATR–FTIR spectra along with the obtained ζ-potential values for the LNPs indicated that the conjugation reactions were successfully achieved through an amide bond formation.

5.2.2 pH-Responsive drug release and delivery into cancer cells

Here, the poorly water-soluble cytotoxic compound (BZL) was selected as a model drug, because of its ability to inhibit the Pim kinases, which are frequently overexpressed in some solid tumors (*e.g.*, prostate and colon cancers), and are implicated in promoting the cell survival and developing resistance against chemo- and radiation-therapies.[320–322]

The BZL@LNPs were again prepared by solvent exchange, and further conjugated with PEG-PHIS and/or CPP. The LDs of BZL into the LNPs, LNPs-CPP and LNPs-PEG-PHIS-CPP were 11, 10 and 9%, respectively, decreasing slightly along the conjugation reactions. Afterwards, the release profiles of pure BZL and BZL@LNPs were evaluated in two different aqueous buffers, mimicking the tumor microenvironment/acidic endosomal (pH 5.5, **Figure 12A**) and the physiological pH values (pH 7.4, **Figure 12B**).[323] The dissolution of the pure BZL at pH 5.5 was slightly slower than at pH 7.4, and reached a plateau at around 48% after 24 h for both the pH values tested. When loaded into LNPs, the BZL release profile was strongly improved, in particular at pH 5.5 (*ca.* 100% after 24 h). However, a decreased dissolution of BZL was observed for all the BZL@LNPs at pH 7.4 after 24 h, when compared to the BZL released from the LNPs at pH 5.5, which can be ascribed to the possible precipitation or degradation of BZL.

Generally, the three LNPs, before and after functionalization, showed the following trend for the release of BZL in both the pH values: BZL@LNPs > BZL@LNPs-CPP > BZL@LNPs-PEG-PHIS-CPP. The decoration of the LNP surface with the block copolymer or CPP seemed to slightly prevent the release of BZL from the LNPs, acting as a drug release barrier. In addition, the ionic interactions between the BZL and the attached ligands could also affect the release profile of BZL.[324] Moreover, the BZL@LNPs-PEG-PHIS-CPP showed a sustained release of BZL compared to the bare BZL@LNPs and CPP-functionalized BZL@LNPs at pH 5.5. Additionally, the release of BZL from BZL@LNPs-PEG-PHIS-CPP was more efficient at pH 5.5 than pH 7.4, showing a pH-responsive behavior that could be correlated with the presence of a basic nitrogen atom on the imidazole ring of PHIS, which after protonation leads to a change on the conformation of the block copolymer on the LNP surface and, consequently, allows the drug release.[246,315]

Overall, the BZL@LNPs showed improved dissolution rates along with pH-responsive release of the BZL compound, by diffusion through the lignin structure.

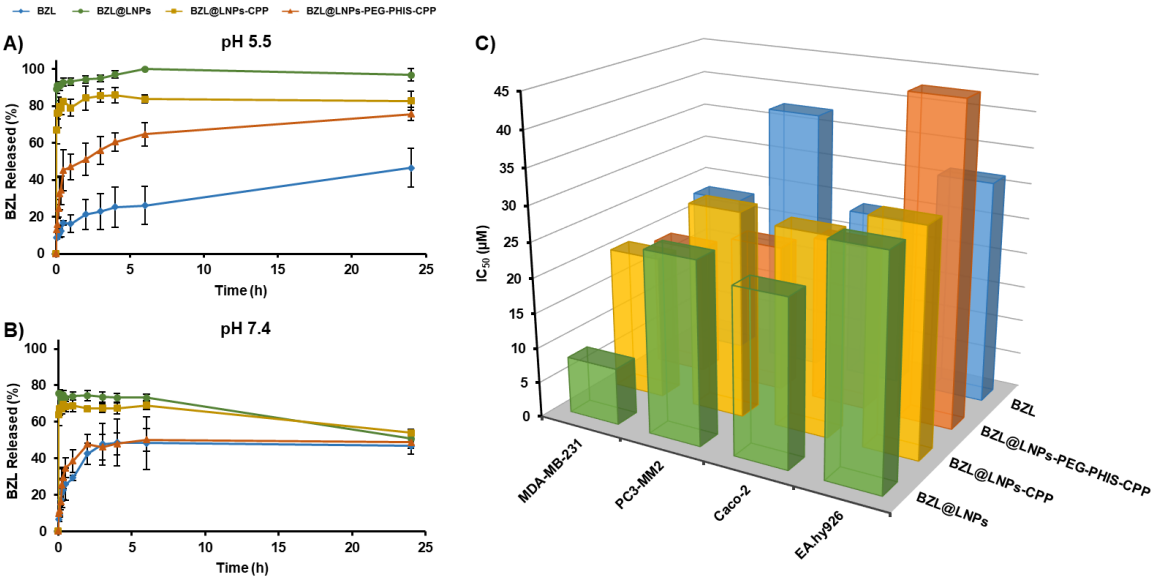

Figure 12. Release profiles of pure BZL and BZL-loaded carboxylated LNPs in (**A**) HBSS–MES (pH 5.5) and (**B**) HBSS–HEPES (pH 7.4), containing 2% (v/v) Tween-80 at 150 rpm at 37 °C for 24 h. (**C**) Representation of the half maximal inhibitory concentration (IC_{50}) values, obtained after the antiproliferative studies of MDA-MB-231, PC3-MM2, Caco-2 and EA.hy926 cell lines treated with pure BZL (blue), previously dissolved with 1% EtOH, BZL@LNPs (green), BZL@LNPs-CPP (yellow) and BZL@LNPs-PEG-PHIS-CPP (orange) after 24 h of incubation with the different cell lines. Error bars represent the mean ± s.d. ($n \geq 3$). Copyright © 2017 Future Science Group. Adapted and reprinted with permission from publication (**II**).

Finally, the antiproliferative effects of the BZL@LNPs were studied using MDA-MB-231, PC3-MM2 and Caco-2 cells to represent the breast, prostate and colon cancers, respectively. In addition, a non-tumor endothelial cell line (EA.hy926) was also evaluated to compare the cytotoxicity effect caused by the BZL released from the LNPs in a physiological environment with the TME present in cancer cells. Here, the growth inhibition effect of BZL@LNPs was compared with equal molar ratio of pure BZL, previously dissolved with 1% EtOH and diluted with cell culture media (**Figure 12C**). Generally, a similar trend on the growth inhibition effect were observed for pure BZL and BZL@LNPs, before and after surface modifications, within the same cell lines. Upon incubation with the three cancer cell lines, the LNPs showed a lower half maximal inhibitory concentration (IC_{50}) values, thus, were more efficient in decreasing the cell viability than the free BZL. Here, the growth inhibition effect of the BZL@CLNPs showed the following trend in cancer cell lines: BZL@LNPs-PEG-PHIS-CPP > BZL@LNPs > BZL@LNPs-CPP > pure BZL. However, upon incubation with a non-tumor EA.hy926 cells, the BZL@LNPs-PEG-PHIS-CPP showed the highest IC_{50} (45.1 μM), compared with the pure BZL, BZL@LNPs and BZL@LNPs-CPP (*ca.* 31 μM). This indicates that the coating with PEG-PHIS slowed down the BZL release from the LNPs-PEG-PHIS-CPP in physiological environment and, consequently, caused less toxic effects to the normal cells.

Taking everything into account, the functionalization of LNPs with PEG-PHIS-CPP was found to be an advantageous approach to slow down the drug release, and the BZL@LNPs inhibited efficiently the cell growth in all the cancer cell lines tested, due to the enhanced solubility of BZL when loaded into the LNPs, without using an organic solvent to pre-solubilize the BZL.

5.3 Preparation and *in vitro* characterization of DSS-modified carboxylated LNPs with long-term stability for enhanced cellular uptake (III)

After the successful modifications on the LNPs obtained in the previous work, the next step was to prepare and characterize different carboxylated lignin polymers, in order to achieve a long-term stability of the LNPs at physiological conditions, so that their cargos would be protected for longer times upon *in vivo* administration. Afterwards, the optimally carboxylated lignin was used to produce LNPs that were further functionalized with a Asp-Ser-Ser (DSS). The DSS polypeptide, derived from dentin phosphophoryn, is a repetitive DSS-rich domain that facilitates non-receptor-mediated endocytosis, acting like the CPP.[325] Additionally, the cellular uptake of DSS-functionalized LNPs in three different cancer cell lines was compared to corresponding iRGD-functionalized LNPs, using 2D and 3D cell culture models.

5.3.1 Characterization of carboxylated lignin and evaluation of long-term stability of carboxylated LNPs

The carboxylation reaction was performed as described in the previous work. In this study, different ratios of the lignin:succinic anhydride were tested in order to find a balance between the carboxylation degree of the lignin polymer and the long-term stability of LNPs at physiological conditions.

In order to confirm the success of the carboxylation reaction, the ATR−FTIR spectra were recorded to qualitatively analyze and compare the prepared carboxylated lignin polymers with the original lignin polymer (**Figure 13A**). Besides the typical bands shown on both original and carboxylated lignin polymers, as already described above, all the carboxylated lignin polymers exhibited a stronger adsorption band at *ca.* 1720 cm^{-1} compared to the original lignin, which is predominantly due to the stretching vibrations of C=O on the free –COOH groups on the carboxylated lignin structure. In addition, an increase on this adsorption band was observed according to the degree of carboxylation, suggesting that the reaction was successfully accomplished.

The resulting carboxylated lignin polymers were quantitatively characterized using ^{31}P NMR spectroscopy to determine the aliphatic and phenolic –OH groups, as well as the carboxyl groups present on the lignin polymers (**Figure 13B**). The amount of –COOH present in the original lignin was 0.455 mmol/g, and it increased after the carboxylation reaction from 0.985 mmol/g for the ratio 5:1 to 2.280 mmol/g for the ratio 1:2, although this increase was not linearly correlated. Consistently, the decrease on the aliphatic and total phenolic –OH groups accompanied the increase on the carboxyl groups, suggesting that the hydroxyl groups on the original lignin structure were successfully reacted with succinic anhydride.

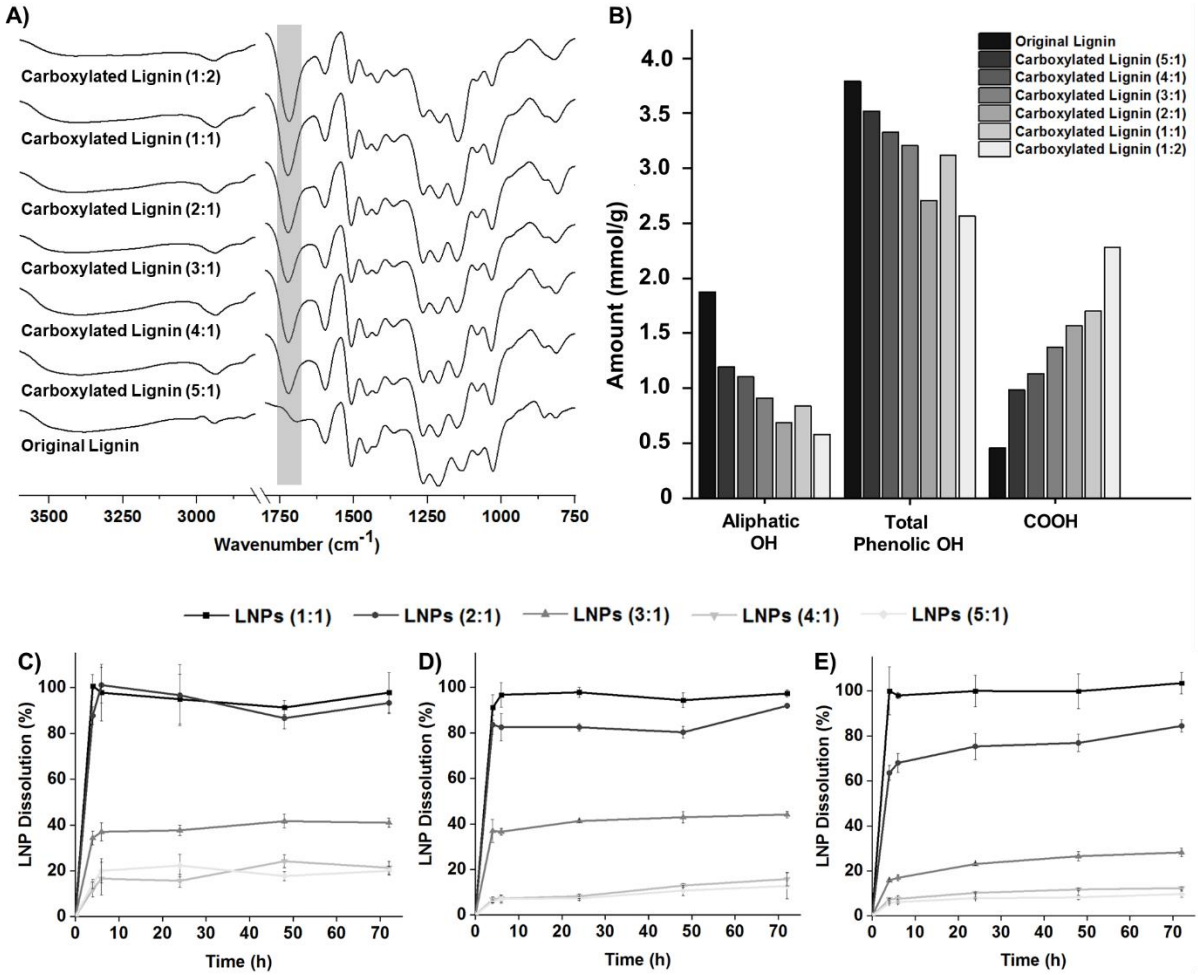

Figure 13. Characterization of the carboxylated lignin polymers after carboxylation reaction using different lignin:succinic anhydride ratios by (**A**) ATR–FTIR spectra and (**B**) quantitative ^{31}P NMR measurements. Evaluation of the long-term stability of LNPs prepared with the different carboxylated lignin by evaluating the dissolution rate of the LNPs after incubation of (**C**) 50 µg/mL, (**D**) 200 µg/mL and (**E**) 500 µg/mL in PBS buffer (pH 7.4) up to 72 h. Results are shown as mean ± s.d. (*n* = 3).

A dissolution experiment with the LNPs was done to evaluate the long-term stability of the LNPs at physiological conditions, in order to select the ideal carboxylated lignin polymer to prepare the LNPs for further experiments. For that, LNPs were prepared using the different carboxylated polymers previously synthesized with the lignin:succinic anhydride ratios of 1:2 [LNPs (1:2)], 1:1 [LNPs (1:1)], 2:1 [LNPs (2:1)], 3:1 [LNPs (3:1)], 4:1 [LNPs (4:1)], and 5:1 [LNPs (5:1)], by the solvent exchange method. Next, LNPs at concentrations of 50 µg/mL (**Figure 13C**), 200 µg/mL (**Figure 13D**), and 500 µg/mL (**Figure 13**) were incubated in PBS (pH 7.4) to mimic the physiological pH, at 37 °C, up to 72 h. The LNPs (1:2) were dissolved instantly after incubation (data not shown). The LNPs (1:1) showed a complete dissolution after 4 h for the three concentrations of LNPs tested. Both LNPs (2:1) and LNPs (3:1) experienced a concentration-dependent dissolution over time. A similar trend for the dissolution of LNPs (4:1) and LNPs (5:1) was noticed, but no significant differences on the dissolution rate between these two LNPs were observed, in particular for the two highest concentrations of LNPs. After 48 h, at 50, 200, and 500 µg/mL, the dissolution of the LNPs (4:1) was about 24, 13, and 11%, and 18, 11, and 8% for the LNPs (5:1), respectively. In general, the dissolution of the LNPs

increased according to the increase on the amount of –COOH groups on the carboxylated lignin polymers. This effect can be attributed to the conversion of carboxylic acids into carboxylates, due to the sodium and potassium ions present in the PBS buffer in a basic environment that reacted with the carboxylic acids. Typically, presenting pK_a values ranging from 3 to 5 in aqueous media at basic pH, the carboxylic acids can be ionized and converted into cationic carboxylates and, consequently, improve their water solubility at basic pH.[326] Here, the NP dissolution seemed to be dependent on the LNP concentration in PBS buffer, because at lower LNP concentration (50 µg/mL), the dissolution was more pronounced as the amount of ions in the PBS buffer was higher. Furthermore, the NP dissolution rate appeared to reach a constant value after a certain carboxylation degree, as it could be observed for both LNPs (4:1) and LNP (5:1). This suggests that some degree of dissolution of LNPs will occur, at any carboxylation degree.

Based on these observations, the ratio 4:1 of lignin:succinic anhydride was the best option to prepare the LNPs (4:1) and carry out the following experiments, because it offered more than two times higher amounts of carboxyl groups (1.132 mmol/g) than the original lignin, and also a good stability at physiological conditions for over 72 h.

5.3.2 Cell–NP interaction studies

The material composition, hydrophobicity/hydrophilicity, size, shape, and surface charge of NPs are important parameters that influence the interactions of the NPs with cells and, therefore, the cytocompatibility and cellular uptake.[162,327] In addition to that, the NP surface functionalization with peptides can be done to increase the cellular uptake of the NPs into different types of cells and tissues.[237,328] Here, the cellular interaction/uptake of the LNPs was evaluated with three different cell lines, both qualitatively and quantitatively, by confocal microscopy and flow cytometry, respectively. For that purpose, a highly stable fluorescent dye (DiA) was loaded into the LNPs before the surface functionalization with iRGD or DSS. The cellular uptake of the bare and peptide-functionalized LNPs was evaluated after incubation with PC3-MM2, MDA-MB-231, and A549 cells during 3 h, using the conventional *in vitro* 2D cell culture model (**Figure 14**). According to the confocal images, there was an increase in the interaction of both LNPs-iRGD and LNPs-DSS with PC3-MM2 (**Figure 14A**), MDA-MB-231 (**Figure 14B**), and A549 (**Figure 14C**) cell lines.

In order to quantify the cellular uptake, the extracellular fluorescence was quenched with trypan blue, before analysis by flow cytometry (**Figure 14D-I**). For the PC3-MM2, both the peptide-functionalized LNPs showed a statistically significantly higher cellular uptake than the bare LNPs, and the LNPs-DSS showed a higher internalization rate than LNPs-iRGD (**Figure 14D**). The mean fluorescence intensity (MFI) values obtained also confirmed these observations (**Figure 14E**). In addition, the LNPs-DSS showed more internalization than LNPs and LNPs-iRGD for both MDA-MB-231 (**Figure 14F** and **14G**) and A549 (**Figure 14H** and **14I**) cells. However, the LNPs showed higher internalization than the LNPs-iRGD for A549, which could be due to a non-specific binding and clustering of negatively charged NPs, such as the –COOH modified NPs, on cationic sites on the plasma membrane, leading to higher internalization.[306] Guarnieri *et al.* (2014) also showed that the cellular internalization of −COOH-modified silica NPs was higher than of the $-NH_2$ counterpart.[329] Therefore, and in a similar way, the surface characteristics of the bare LNPs could also lead to an increased cellular uptake in A549 compared to the LNPs-iRGD.

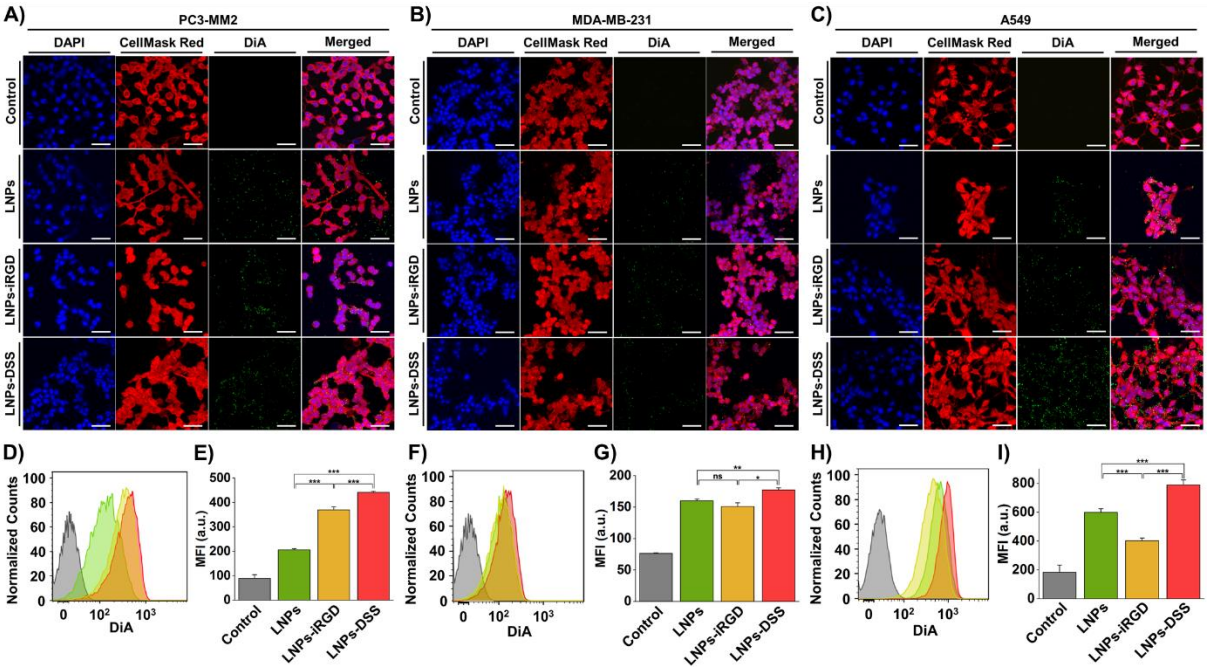

Figure 14. *In vitro* cellular interaction studies using a 2D cell culture model: (**A-C**) Confocal fluorescence microscopy images of (**A**) PC3-MM2, (**B**) MDA-MB-231 and (**C**) A549 cell lines, after incubation with 100 µg/mL of bare and peptide-functionalized DiA@LNPs for 3 h at 37 °C. DAPI (blue), DiA (green), and CellMask Red (red) were used to stain the nucleus, the LNPs, and the cell membrane, respectively. The merged panels show the association of the LNPs with the cell membrane. Scale bars are 50 µm. Quantitative cellular uptake by flow cytometry, after incubation of 100 µg/mL of LNPs with (**D**) PC3-MM2, (**F**) MDA-MB-231, and (**H**) A549, for 3 h at 37 °C, in which the LNPs (green) LNPs-iRGD (yellow) and LNPs-DSS (red) were compared to the untreated control (grey). MFI quantification for (**E**) PC3-MM2, (**G**) MDA-MB-231, and (**I**) A549 before and after treatment with the DiA@LNPs. At least 10000 events were collected for each measurement. The error bars show the mean ± s.d. (n = 3). Statistical significance was set at probabilities of *p < 0.05, **p < 0.01 and ***p < 0.001, and *ns* is non-significant.

The *in vitro* cellular uptake of NPs is conventionally evaluated using a 2D model in a flat cell culturing surface, a model that does not represent the morphology and 3D organization of the native tissues. Consequently, the cell−cell interactions are not realistic, which can lead to a misinterpretation of the cellular uptake and consequent biological efficacy of the NPs compared to the 3D culturing models.[330–332] Thus, the cellular interactions/uptake of bare and peptide-functionalized LNPs were evaluated with the same cell lines using the 3D tumor spheroids (*ca.* 600 µm of diameter), and compared with the conventional 2D model. The confocal microscopy images of the tumor spheroids showed that both the peptide-functionalized LNPs improved the interaction with the three cell lines, compared to the bare LNPs (**Figure 15A-C**). For PC3-MM2 and A549 cells, the LNPs-DSS showed an increased interaction compared to the LNPs-iRGD. Additionally, the tumor spheroids were disassembled after the incubation with the LNPs, the extracellular fluorescence was quenched after incubation with trypan blue, and the cellular uptake was then quantified by flow cytometry. For the PC3-MM2, the cellular uptake of the LNPs-DSS was found to be significantly higher than the LNPs-iRGD and bare LNPs (**Figure 15D** and **15E**). Regarding the MDA-MB-231, the two

peptide-modified LNPs showed increased cellular internalization compared to the bare LNPs (**Figure 15F** and **15G**). As for the A549 cells, the same trend was observed for the cellular uptake of LNPs, and the LNPs-DSS showed an improved cellular internalization compared to the LNPs-iRGD and LNPs (**Figure 15H** and **15I**).

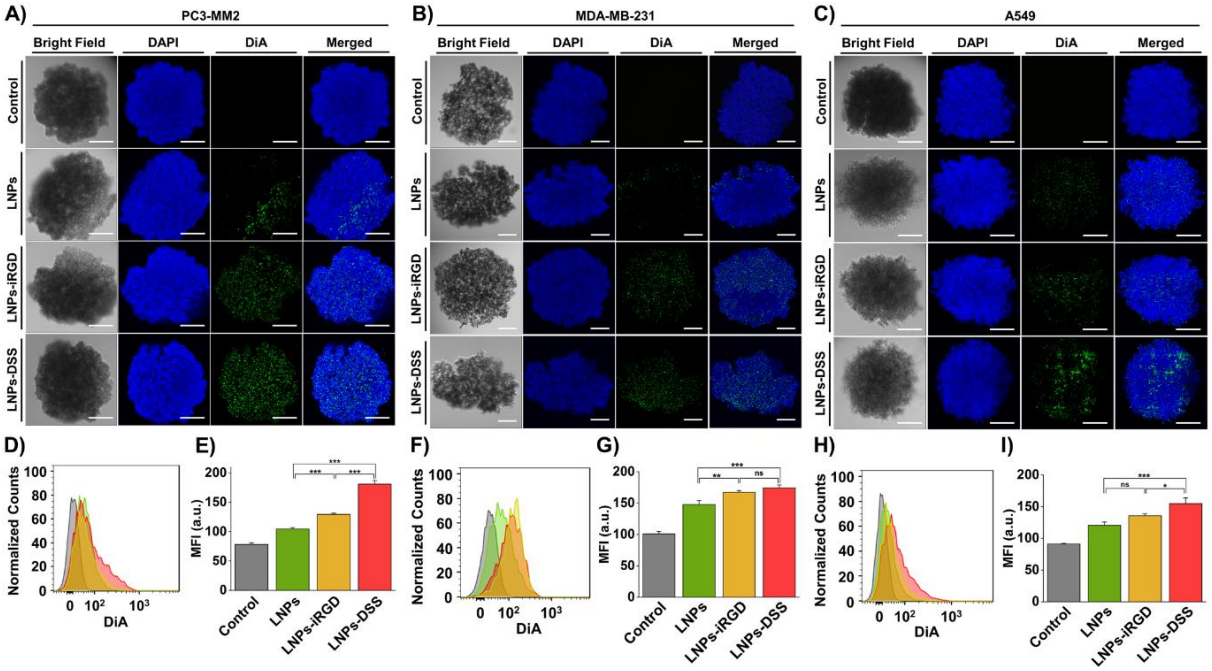

Figure 15. *In vitro* cellular interaction studies using 3D tumor spheroids: (**A-C**) Confocal fluorescence microscopy images of (**A**) PC3-MM2, (**B**) MDA-MB-231 and (**C**) A549 cell lines, after incubation with 100 µg/mL of bare and peptide-functionalized DiA@LNPs for 3 h at 37 °C. DAPI (blue) and DiA (green) were used to stain the nucleus and the LNPs, respectively. The merged panels show the association of the LNPs with the tumor spheroid. Scale bars are 200 µm. Quantitative cellular uptake by flow cytometry, after incubation of 100 µg/mL of LNPs with (**D**) PC3-MM2, (**F**) MDA-MB-231, and (**H**) A549, for 3 h at 37 °C, in which the LNPs (green) LNPs-iRGD (yellow) and LNPs-DSS (red) were compared to the untreated control (grey). MFI quantification for (**E**) PC3-MM2, (**G**) MDA-MB-231, and (**I**) A549 before and after treatment with the DiA@LNPs. At least 5000 events were collected for each measurement. The error bars represent mean ± s.d. (n = 3). Statistical significance was set at probabilities of *p < 0.05, **p < 0.01 and ***p < 0.001, and *ns* is non-significant.

Comparing the two cell culturing models, the cellular uptake of the LNPs was expectably higher for the 2D cell model than for the 3D tumor spheroids, which is in agreement with the higher MFI values obtained for the 2D-cultured cells. This can be correlated with the stronger and more realistic cell−cell interactions in the 3D cell culturing model, and also because of the effect of the NPs sedimentation on the 2D cell culturing plate.[333]

Although both the peptide-modified LNPs were generally internalized more efficiently in both the cell culturing models in the three cell lines, LNPs-DSS showed a superior cellular internalization compared to the LNPs-iRGD in some cases. The iRGD binds to the integrins overexpressed in the tumor endothelium, improving the tissue penetration in the tumor, and upon cleavage it binds to NRP-1 receptor.[334] Even though the dentin phosphophoryn contains a conserved RGD domain in several species, the internalization of this DSS polypeptide is not

mediated through integrin receptors.[325] Moreover, neither clathrin nor the caveolae-mediated pathways were responsible for the improved cellular uptake of DSS peptide.[325] Additionally, the disruption of the microtubules and microfilaments involved in the endocytic process did not prevent the endocytosis of the DSS peptide.[325] Contrasting with iRGD peptide, the internalization of the DSS peptide was not associated with the amount of cellular target/receptor for its endocytosis.

Concluding remarks: the DSS peptide can also be employed to modify the NP's surface, improving the cellular internalization of the NPs into different types of cancer cells through a non-receptor-mediated endocytosis and, consequently, releasing different cargos intracellularly in an efficient manner for different therapeutic applications.

5.4 Skewing M2-like tumor macrophages with mUNO-targeted R848-loaded LNPs for enhanced chemotherapy (IV)

Triple-negative breast cancer (TNBC) is characterized by the lack of molecular targets/receptors (*e.g.*, estrogen and progesterone or HER2), which are molecular targets of different therapeutic agents and, therefore, is associated with a poor prognosis of patients compared to other breast cancer subtypes.[335] Additionally, TAMs that usually resemble an M2-like macrophage phenotype constitute up to 50% of the tumor mass in breast cancer, being associated to an even worse prognosis, tumor progression and recurrence, and higher risk of distant metastases.[336–338] Chemotherapy is still the primary established systemic treatment choice for patients with both early-stage and advanced-stage TNBC.[339] Therefore, targeting of therapeutics to TME components, such as TAMs, seems to be an alternative or complementary approach to improve the outcome of the TNBC patients.

In this study, LNPs were loaded with R848, a dual agonist of the toll-like receptors TLR7 and TLR8 that can induce the repolarization of M2-like macrophages towards M1-like macrophages, which present an anti-tumor phenotype that can lead to a controlled tumor growth.[290] The R848@LNPs were functionalized with a short peptide (CSPGAK, "mUNO") that targets the mannose receptor (CD206), typically overexpressed in the M2-like macrophages.[340,341] The homing ability of untargeted and targeted R848@LNPs, hereafter referred as R848@LNPs-P-FAM and R848@LNPs-P-F-mUNO, respectively, was assessed using an orthotopic 4T1 TNBC preclinical model. Afterwards, the therapeutic effect of these nanosystems was evaluated to potentiate the antitumor efficacy of a chemotherapeutic compound (vinblastine, Vin). Finally, the immunological profile of the cells extracted from the tumor tissue of the groups receiving the nanoformulated or free R848 were also compared, using flow cytometry.

5.4.1 Homing study and *ex vivo* biodistribution analysis

After the physicochemical characterization of the nanosystems, and the *in vitro* targeting ability towards M2-like macrophages and re-education into the anti-tumor M1-like macrophages, the *in vivo* biodistribution of the prepared nanosystems was evaluated. For that, both R848@LNPs-P-FAM and R848@LNPs-P-F-mUNO were injected i.p. in an orthotopic 4T1 tumor-bearing mice, and their homing ability to the tumor tissue was compared. After 3 h of circulation time, mice were sacrificed and their organs were collected and cryo-sectioned for *ex vivo* biodistribution analysis by confocal microscopy (**Figure 3A**, publication **IV**). The

accumulation of the NPs in the lungs was very low, suggesting that almost no NP aggregates were formed. Additionally, the accumulation of both the nanosystems was low in the main organs associated to the clearance of NPs (liver, spleen and kidney), which indicated that the NPs were either in the bloodstream circulation or cleared out from these organs after 3 h.

Looking at the tumor tissue sections (**Figure 3A** and **3B**, publication **IV**), both R848@LNPs-P-FAM and R848@LNPs-P-F-mUNO showed similar patterns of accumulation in the TAMs at the tumor site, which was quantified by the co-localization of the FAM signal and CD206 signal (**Figure 3C**, publication **IV**). Here, the percentage of co-localization of both channels was about 50% and 60% for R848@LNPs-P-FAM and R848@LNPs-P-F-mUNO, respectively. However, when the intensity of the FAM signal was quantified in the $CD206^+$ macrophages, the R848@LNPs-P-F-mUNO showed a significantly higher accumulation compared to the control R848@LNPs-P-FAM (**Figure 3D**, publication **IV**), indicating that the mUNO peptide can effectively increase the interaction of R848@LNPs with the M2-like macrophages in the TME.

5.4.2 Therapeutic study and *ex vivo* immunological profile of tumor cells

Vin is a vinca alkaloid and microtubule-destabilizing agent that interferes with the cell growth and survival, by disrupting the dynamic equilibrium of the microtubules, which blocks the cell cycle at the metaphase-anaphase transition in mitosis, leading to the cellular apoptosis.[342] For this therapeutic study, the water-soluble Vin (Vinblastine sulfate) was selected as the chemotherapeutic agent, because it does not interfere with the viability of the M2-like TAMs, as they present none or minimal proliferation rates.[266]

As a result of the relative toxicity of Vin towards different cell lines compared to other chemotherapeutic agents,[343] the dose for Vin administration chosen was 1 mg/kg, which was co-administered with free R848 or R848@LNPs at *ca.* 0.125 mg/kg, using the orthotopic 4T1 TNBC model in immunocompetent Balb/c mice. On day 6 of p.i., mice were randomly sorted into 5 groups with tumor volume average of 46–48 mm^3, and the treatment administered intraperitoneally was: (1) PBS and 5.4% of glucose (Control); (2) Vin and 5.4% of glucose (Vin); (3) Vin and free R848 (Vin + R848); (4) Vin and R848@LNPs-P-FAM (Vin + R848@LNPs-P-FAM); and (5) Vin and R848@LNPs-P-F-mUNO (Vin + R848@LNPs-P-F-mUNO). The treatment schedule is shown in **Figure 4A** (publication **IV**), where the Vin was co-administered with the free and nanoformulated R848 every other day, to enhance the antitumor efficacy. The Vin treatment was interrupted due to its toxicity, which ultimately led to the weight loss of the mice receiving Vin (**Figure S5** in Supporting Information, publication **IV**). After that, two more doses of the free and nanoformulated R848 were given i.p. until the endpoint, which was defined at day 18 of p.i., in order to study the immunological profile of the cells in the tumor tissues.

During the course of the treatment, the Vin treatment showed some antitumor activity, as the tumor volume decreased compared to the PBS group (**Figure 4B**, publication **IV**). However, the group receiving the R848@LNPs-P-F-mUNO treatment showed an increased antitumor efficacy compared to all the other groups receiving Vin. Interestingly, at the end of the treatment, the two groups receiving both Vin and R848@LNPs showed a significant decrease in tumor weights, compared to the control group (**Figure 4C**, publication **IV**). This is in line with the results observed in the homing study, which showed that both the R848@LNPs could be accumulated in the $CD206^+$ TAMs, which could be explained by the accumulation of both the NPs in the tumor tissue driven by the EPR effect.[224] Moreover, the R848@LNPs-P-F-

mUNO treatment also showed a significant reduction in the tumor weight compared to the groups receiving Vin alone or co-administered with free R848. These findings suggested that the mUNO targeting of the R848 loaded in a nanocarrier to M2-like macrophages at the tumor can improve the efficacy compared to the R848 in the free form, by altering its pharmacokinetics and biodistribution upon administration.

Finally, the profile of the immune cell population extracted from the tumors was investigated using flow cytometry, and a comparison between the groups receiving the nanoformulated or free R848 were carried out (**Figure 4D-G**, publication **IV**). Firstly, the modifications in the macrophage population on the tumor tissue were assessed, which was primarily defined by the presence of the F4/80 marker. Therefore, the CD206 and CD86 markers were further used to identify the M2- or M1-like macrophages, respectively.[269,270] Both untargeted and mUNO-targeted R848@LNPs showed an increased level of $F4/80^+CD86^+$ macrophages, compared to the free R848 (**Figure 4D**, publication **IV**), suggesting that the delivery of R848 with LNPs can significantly improve the therapeutic effect of R848 on the differentiation of M2 macrophages into M1-like phenotype at the tumor tissue. This repolarization into M1 macrophages can lead to an anti-tumor response characterized by the release of pro-inflammatory signals (*e.g.*, TNF-α, IL-6, and IL-12) and production of ROS.[263,269,270] Surprisingly, the amount of $F4/80^+CD206^+$ in the tumor was higher for both treatments with the R848@LNPs than the free R848 (**Figure 4E**, publication **IV**). This effect can be due to an increase in the M2 polarized macrophages in hypoxic/necrotic areas of the tumor, as reported by Galstyan *et al.* (2019), who found a pronounced tissue necrosis and lack of tumor vasculature in treated tumors, and consequent persistence of M2-like macrophages after a nanoscale immunoconjugate treatment.[344] Additionally, M2 macrophages present in the TME are also associated with a poor infiltration of T cells in the tumor, in particular the tumor-infiltrating lymphocytes (TILs), which is frequently correlated to a poor outcome in cancer patients. However, TAMs depletion was shown to restore the T cell migration and infiltration into tumors.[345] In this way, the CD3 and CD8 markers were used to evaluate the presence of TILs or CTLs ($CD8^+$ T cells) in the tumor tissues (**Figure 4F**, publication **IV**). The percentage of $CD3^+CD8^+$ T cells in the tumor was significantly higher for the group receiving the R848@LNPs-P-F-mUNO compared with the other two groups, indicating that the re-education of M2-macrophages accomplished by mUNO-targeted R848@LNPs was more efficient. This might have been a consequence of the reduction of the immunosuppressive microenvironment in the tumor that indirectly inhibited the action of $CD8^+$ T cells, and directly inhibited T cell cytotoxicity caused by the release of ARG1, which ultimately prevents the T cell activation.[346,347] Therefore, the tumor infiltration of CTLs can induce an immune response against the tumor, characterized by IFN-γ secretion.[348] Primarily characterized by the expression of CD11c, the DCs' population was also evaluated in the tumor tissues, in particular the percentage of activated $CD86^+$ DCs (**Figure 4G**, publication **IV**). Generally, the delivery of R848 by LNPs led to an increased percentage of CD86 positive DCs in the tumor, compared to the free R848. The infiltration of tumor tissues by APCs (such as DCs) is also an important prognostic factor in the treatment of cancer, because it can provide a second stimulatory signal to start the anti-tumor T cell response.[346]

The repeated systemic administration of TLR agonists, such as R848, is not a common practice in the clinic, mainly due to its systemic side effects (*e.g.*, fever and headache).[349] However, the delivery of R848 using a nanocarrier can alter the biodistribution of the R848 and increase its accumulation and efficacy in modifying the immunological profile of the cells in the TME, which was not possible with the systemic administration of free R848. In addition, the

use of mUNO-modified LNP to target the M2 macrophages showed an improved efficiency of the R848 in different ways. Therefore, the co-administration of R848@LNPs allowed an improvement of the administered drug in a very aggressive cancer tumor with a poor prognosis, such as the TNBC.

6 Conclusions

Lignin has been recently employed for high-value added applications, such as drug delivery. The key goal of this thesis was to provide new insights on the use of the unexploited lignin polymer to develop and characterize LNPs for anticancer drug delivery applications.

Firstly, three different LNPs were prepared by a solvent exchange process, with a spherical shape and negative surface charge that provided a good colloidal stability. Additionally, they exhibited good cytocompatibility towards different cell lines. LNPs also showed the ability to load different poorly water-soluble therapeutic compounds, and improved their release profiles at different pH-values. Consequently, the growth inhibition effect of BZL in different cell lines was also enhanced after loading into LNPs, which enabled the use of these innovative LNPs as drug delivery systems for anti-cancer applications.

Secondly, a carboxylation reaction was successfully achieved on the original lignin polymer, which allowed the surface modification of LNPs with PEG-PHIS and CPP, confirmed by the conversion of the surface charge from negative to positive after the conjugation reactions, without compromising the cytocompatibility of the LNPs. These nanosystems allowed also the loading of a poorly water-soluble cytotoxic agent, BZL, in order to enhance its release profile at both pH 5.5 and 7.4, with higher dissolution rates at the acidic pH. Furthermore, the functionalization of LNPs with PEG-PHIS-CPP provided an improved antiproliferative effect of BZL in different cancer cell lines, but a decreased release of BZL in physiological environment, resulting in lower toxicity towards a healthy cell line.

After preparing lignin polymers with different degrees of carboxylation, the optimal ratio in terms of stability at physiological conditions was used to prepare LNPs, which were further modified with a novel DSS peptide, and the cellular internalization was compared with the LNPs-iRGD, using both 2D and 3D cell culturing models. Overall, the LNPs-DSS exhibited similar or increased cellular internalization compared with the LNPs-iRGD, indicating that the DSS can also be used as a targeting ligand to enhance the intracellularly delivery of cargos.

Finally, the LNPs were shown to effectively alter the *in vivo* biodistribution of the nanoparticulate R848 compared to the free R848, in enhanced chemotherapy using an aggressive tumor model, such as the orthotopic 4T1 TNBC. In addition, the use of mUNO-modified LNPs showed an improved accumulation and efficacy of the R848 in the tumor, by targeting the M2 macrophages. This was achieved by altering the immunological profile of the cells in the TME, such as macrophages, while promoting the infiltration of the tumor by cytotoxic T cells and dendritic cells.

Overall, lignin-based systems were developed in this thesis by solvent exchange, and further surface functionalization with targeting moieties was done to improve the delivery of poorly water-soluble compounds and, ultimately, to enhance cancer therapy. However, there are some limitations regarding the manufacture of these nanosystems using bulk methods, such as time-consumption, reproducibility and scalability, which are important factors when considering the commercialization and translation of such nanosystems into the clinic. A continuation of this work would be to use, for example, the microfluidic technique to produce LNPs in a more controlled and reproducible manner. The preparation of other lignin-based materials, such as hydrogels, could also be useful to achieve a more controlled drug release of therapeutics in the tumor, in order to avoid multiple administrations of nanoparticulate systems. Additionally, further studies using a combination with checkpoint inhibitors (*e.g.*, anti-PD1 and anti-CTLA4 antibodies) could increase the efficacy of the *in vivo* treatment with R848-loaded LNPs. This combination could also be tested in other types of cancer, such as a highly immunogenic tumor type melanoma.

References

1. Boerjan, W., *et al*. Lignin biosynthesis. *Annu. Rev. Plant Biol.* **54**, 519–546 (2003).
2. Laurichesse, S. & Avérous, L. Chemical modification of lignins: Towards biobased polymers. *Prog. Polym. Sci.* **39**, 1266–1290 (2014).
3. Zhao, W., *et al*. From lignin association to nano-/micro-particle preparation: Extracting higher value of lignin. *Green Chem.* **18**, 5693–5700 (2016).
4. Nair, S. *et al.* High shear homogenization of lignin to nanolignin and thermal stability of nanolignin-polyvinyl alcohol blends. *ChemSusChem* **7**, 3513–3520 (2014).
5. Rinaldi, R., *et al.* Paving the way for lignin valorisation: Recent advances in bioengineering, biorefining and catalysis. *Angew. Chem. Int. Ed.* **55**, 8164–8215 (2016).
6. Kai, D. *et al.* Towards lignin-based functional materials in a sustainable world. *Green Chem.* **18**, 1175–1200 (2016).
7. Figueiredo, P., *et al*. Properties and chemical modifications of lignin: Towards lignin-based nanomaterials for biomedical applications. *Prog. Mater. Sci.* **93**, 233–269 (2018).
8. Bray, F., *et al.* Global cancer statistics 2018: GLOBOCAN estimates of incidence and mortality worldwide for 36 cancers in 185 countries. *CA. Cancer J. Clin.* **68**, 394–424 (2018).
9. Peer, D., *et al.* Nanocarriers as an emerging platform for cancer therapy. *Nat. Nanotechnol.* **2**, 751 (2007).
10. Wang, X., *et al*. Application of nanotechnology in cancer therapy and imaging. *CA. Cancer J. Clin.* **58**, 97–110 (2008).
11. Wu, Q., *et al*. Multi-drug resistance in cancer chemotherapeutics: Mechanisms and lab approaches. *Cancer Lett.* **347**, 159–166 (2014).
12. Bor, G., *et al*. Nanomedicines for cancer therapy: current status, challenges and future prospects. *Ther. Deliv.* **10**, 113–132 (2019).
13. Dawidczyk, C. M., *et al*. Nanomedicines for cancer therapy: state-of-the-art and limitations to pre-clinical studies that hinder future developments. *Front. Chem.* **2**, (2014).
14. Shi, J., *et al*. Cancer nanomedicine: progress, challenges and opportunities. *Nat. Rev. Cancer* **17**, 20–37 (2017).
15. Tran, S., *et al*. Cancer nanomedicine: a review of recent success in drug delivery. *Clin. Transl. Med.* **6**, 44 (2017).
16. Figueiredo, P., *et al*. Chapter 13 - Nanomedicine therapies. in *Handbook of in vivo Chemistry in Mice: from Lab to Living System.* 373–400 (Wiley-VCH, 2020).
17. Yoo, J., *et al*. Active targeting strategies using biological ligands for nanoparticle drug delivery systems. *Cancers (Basel).* **11**, (2019).
18. Gu, F. X. *et al.* Targeted nanoparticles for cancer therapy. *Nano Today* **2**, 14–21 (2007).
19. Fontana, F., Figueiredo, P. & Santos, H. A. Advanced nanovaccines for immunotherapy applications: From concept to animal tests. in *Theranostic Bionanomaterials* 231–260 (Elsevier, 2019).
20. Li, X. *et al.* Harnessing tumor-associated macrophages as aids for cancer immunotherapy. *Mol. Cancer* **18**, 177 (2019).
21. Gustafson, H. H. & Pun, S. H. Instructing macrophages to fight cancer. *Nat. Biomed. Eng.* **2**, 559–561 (2018).
22. Ramakrishna, S., *et al*. Biomedical applications of polymer-composite materials: a review. *Compos. Sci. Technol.* **61**, 1189–1224 (2001).
23. Thakur, V. K., Thakur, M. K. & Gupta, R. K. Rapid synthesis of graft copolymers from natural cellulose fibers. *Carbohydr. Polym.* **98**, 820–828 (2013).
24. Thakur, V. K. & Thakur, M. K. Recent advances in green hydrogels from lignin: A review. *Int. J. Biol. Macromol.* **72**, 834–847 (2015).
25. Tschan, M. J. L., *et al*. Synthesis of biodegradable polymers from renewable resources. *Polym. Chem.* **3**, 836–851 (2012).
26. Bruijnincx, P. C. A. & Weckhuysen, B. M. Biomass conversion: Lignin up for break-down. *Nat. Chem.* **6**, 1035–1036 (2014).
27. Doherty, W. O. S., Mousavioun, P. & Fellows, C. M. Value-adding to cellulosic ethanol: Lignin polymers. *Ind.l Crops Prod.* **33**, 259–276 (2011).
28. Upton, B. M. & Kasko, A. M. Strategies for the conversion of lignin to high-value polymeric materials: Review and perspective. *Chem. Rev.* **116**, 2275–2306 (2016).
29. Duval, A. & Lawoko, M. A review on lignin-based polymeric, micro- and nano-structured materials. *React. Funct. Polym.* **85**, 78–96 (2014).
30. Feldman, D. Lignin nanocomposites. *J. Macromol. Sci. A* **53**, 382–387 (2016).
31. Grabber, J. H. How do lignin composition, structure, and cross-linking affect degradability? A review of cell wall model studies. in *Crop Sci.* **45**, 820–831 (2005).
32. Vanholme, R., *et al*. Lignin biosynthesis and structure. *Plant Physiol.* **153**, 895–905 (2010).
33. Constant, S., *et al.* New insights into the structure and composition of technical lignins: A comparative characterisation study. *Green Chem.* **18**, 2651–2665 (2016).
34. Zhao, Q. Lignification: Flexibility, Biosynthesis and regulation. *Trends Plant Sci.* **21**, 713–721 (2016).
35. Liu, C. J. Deciphering the enigma of lignification: Precursor transport, oxidation, and the topochemistry of lignin assembly. in *Mol. Plant* **5**, 304–317 (Oxford University Press, 2012).
36. Joffres, B., *et al.* Conversion thermochimique de la lignine en carburants et produits chimiques: Une revue.

Oil Gas Sci. Technol. **68**, 753–763 (2013).
37. Xu, C., *et al*. Lignin depolymerisation strategies: Towards valuable chemicals and fuels. *Chem. Soc. Rev.* **43**, 7485–7500 (2014).
38. Wang, J. *et al.* Reduction of lignin color via one-step UV irradiation. *Green Chem.* **18**, 695–699 (2016).
39. Pan, X., *et al*. N. Organosolv ethanol lignin from hybrid poplar as a radical scavenger: Relationship between lignin structure, extraction conditions, and antioxidant activity. *J. Agric. Food Chem.* **54**, 5806–5813 (2006).
40. Cruz, J. M., *et al*. Antioxidant and antimicrobial effects of extracts from hydrolysates of lignocellulosic materials. *J. Agric. Food Chem.* **49**, 2459–2464 (2001).
41. Toh, K. *et al.* Anti-deterioration effect of lignin as an ultraviolet absorbent in polypropylene and polyethylene. *Polym. J.* **37**, 633–635 (2005).
42. Réti, C., *et al*. Flammability properties of intumescent PLA starch and lignin. *Polym. Adv. Technol.* **19**, 628–635 (2008).
43. Norgren, M. & Edlund, H. Lignin: Recent advances and emerging applications. *Curr. Opin. Colloid Interface Sci.* **19**, 409–416 (2014).
44. Zakzeski, J., *et al*. The catalytic valorization of lignin for the production of renewable chemicals. *Chem. Rev.* **110**, 3552–3599 (2010).
45. Galkin, M. V. & Samec, J. S. M. Lignin valorization through catalytic lignocellulose fractionation: A fundamental platform for the future biorefinery. *ChemSusChem* **9**, 1544–1558 (2016).
46. Tejado, A., *et al*. Physico-chemical characterization of lignins from different sources for use in phenol-formaldehyde resin synthesis. *Bioresour. Technol.* **98**, 1655–1663 (2007).
47. Azadi, P., *et al*. Liquid fuels, hydrogen and chemicals from lignin: A critical review. *Renew. Sust. Energ. Rev.* **21**, 506–523 (2013).
48. Liitiä, T. M., *et al*. Analysis of technical lignins by two- and three-dimensional NMR spectroscopy. *J. Agric. Food Chem.* **51**, 2136–2143 (2003).
49. Koljonen, K., *et al*. Precipitation of lignin and extractives on kraft pulp: Effect on surface chemistry, surface morphology and paper strength. *Cellulose* **11**, 209–224 (2004).
50. Chakar, F. S. & Ragauskas, A. J. Review of current and future softwood kraft lignin process chemistry. *Ind. Crops Prod.* **20**, 131–141 (2004).
51. Glasser, W. G., Davé, V. & Frazier, C. E. Molecular weight distribution of (semi-) commercial lignin derivatives. *J. Wood Chem. Technol.* **13**, 545–559 (1993).
52. Valmet LignoBoost - lignin extraction. Available at: https://www.valmet.com/more-industries/bio/lignin-separation/. (Accessed: 12th October 2019)
53. BioChoice® Lignin | Domtar. Available at: https://www.domtar.com/en/what-we-make/biomaterials/biochoice-lignin. (Accessed: 12th October 2019)
54. Lineo™ kraft lignin | Stora Enso. Available at: https://www.storaenso.com/en/products/lignin/lineo. (Accessed: 12th October 2019)
55. UPM BioPiva product family | UPM Biochemicals. Available at: https://www.upmbiochemicals.com/products/lignin/UPM-BioPiva-product-family/. (Accessed: 12th October 2019)
56. de la Torre, M. J., *et al*. Organosolv lignin for biofuel. *Ind. Crops Prod.* **45**, 58–63 (2013).
57. El Hage, R., *et al*. Effects of process severity on the chemical structure of Miscanthus ethanol organosolv lignin. *Polym. Degrad. Stab.* **95**, 997–1003 (2010).
58. Viell, J., *et al*. Is biomass fractionation by Organosolv-like processes economically viable? A conceptual design study. *Bioresour. Technol.* **150**, 89–97 (2013).
59. Matsushita, Y. Conversion of technical lignins to functional materials with retained polymeric properties. *J. Wood Sci.* **61**, 230–250 (2015).
60. Lora, J. H. & Glasser, W. G. Recent industrial applications of lignin: A sustainable alternative to nonrenewable materials. *J. Polym. Environ.* **10**, 39–48 (2002).
61. Mishra, S. B., *et al*. Study of performance properties of lignin-based polyblends with polyvinyl chloride. *J. Mater. Process. Technol.* **183**, 273–276 (2007).
62. Pouteau, C., *et al*. Lignin-polymer blends: Evaluation of compatibility by image analysis. *Comptes Rendus - Biol.* **327**, 935–943 (2004).
63. Lin, N., *et al.* Structure and properties of poly(butylene succinate) filled with lignin: A case of lignosulfonate. *J. Appl. Polym. Sci.* **121**, 1717–1724 (2011).
64. Domenek, S., *et al*. Potential of lignins as antioxidant additive in active biodegradable packaging materials. *J. Polym. Environ.* **21**, 692–701 (2013).
65. Wang, H., Tucker, M. & Ji, Y. Recent development in chemical depolymerization of lignin: A review. *J. Appl. Chem.* **2013**, 1–9 (2013).
66. Pandey, M. P. & Kim, C. S. Lignin depolymerization and conversion: A review of thermochemical methods. *Chem. Eng. Technol.* **34**, 29–41 (2011).
67. Rangan, A., *et al*. Lignin/Nanolignin and their biodegradable composites. in *Biodegradable Green Composites* 167–198 (Wiley, 2016).
68. Thulluri, C., *et al*. Synthesis of lignin-based nanomaterials/nanocomposites: Recent trends and future perspectives. *Ind. Biotechnol.* **12**, 153–160 (2016).
69. Lu, Q., *et al.* Comparative antioxidant activity of nanoscale lignin prepared by a supercritical antisolvent (SAS) process with non-nanoscale lignin. *Food Chem.* **135**, 63–67 (2012).
70. Myint, A. A., *et al.* One pot synthesis of environmentally friendly lignin nanoparticles with compressed liquid

carbon dioxide as an antisolvent. *Green Chem.* **18**, 2129–2146 (2016).
71. Yearla, S. R. & Padmasree, K. Preparation and characterisation of lignin nanoparticles: evaluation of their potential as antioxidants and UV protectants. *J. Exp. Nanosci.* **11**, 289–302 (2016).
72. Qian, Y., *et al*. Formation of uniform colloidal spheres from lignin, a renewable resource recovered from pulping spent liquor. *Green Chem.* **16**, 2156–2163 (2014).
73. Li, H., *et al.* Preparation of nanocapsules via the self-assembly of kraft lignin: A totally green process with renewable resources. *ACS Sustain. Chem. Eng.* **4**, 1946–1953 (2016).
74. Lintinen, K., *et al.* Closed cycle production of concentrated and dry redispersible colloidal lignin particles with a three solvent polarity exchange method. *Green Chem.* **20**, 843–850 (2018).
75. Xiong, F., *et al.* Preparation and formation mechanism of size-controlled lignin nanospheres by self-assembly. *Ind. Crops Prod.* **100**, 146–152 (2017).
76. Lievonen, M., *et al.* A simple process for lignin nanoparticle preparation. *Green Chem.* **18**, 1416–1422 (2016).
77. Lintinen, K., *et al.* Antimicrobial colloidal silver–lignin particles via ion and solvent exchange. *ACS Sustain. Chem. Eng.* **7**, 15297–15303 (2019).
78. Lintinen, K. *et al.* Structural diversity in metal–organic nanoparticles based on iron isopropoxide treated lignin. *RSC Adv.* **6**, 31790–31796 (2016).
79. Nypelö, T. E., Carrillo, C. A. & Rojas, O. J. Lignin supracolloids synthesized from (W/O) microemulsions: Use in the interfacial stabilization of Pickering systems and organic carriers for silver metal. *Soft Matter.* **11**, 2046–2054 (2015).
80. Tortora, M., *et al.* Ultrasound driven assembly of lignin into microcapsules for storage and delivery of hydrophobic molecules. *Biomacromolecules* **15**, 1634–1643 (2014).
81. Yiamsawas, D., *et al.* Biodegradable lignin nanocontainers. *RSC Adv.* **4**, 11661–11663 (2014).
82. Chen, N., Dempere, L. A. & Tong, Z. Synthesis of pH-responsive lignin-based nanocapsules for controlled release of hydrophobic molecules. *ACS Sustain. Chem. Eng.* **4**, 5204–5211 (2016).
83. Kuijpers, M. W. A., Kemmere, M. F. & Keurentjes, J. T. F. Calorimetric study of the energy efficiency for ultrasound-induced radical formation. in *Ultrasonics* **40**, 675–678 (2002).
84. Patil, M. N. & Pandit, A. B. Cavitation - A novel technique for making stable nano-suspensions. *Ultrason. Sonochem.* **14**, 519–530 (2007).
85. Gilca, I. A., Popa, V. I. & Crestini, C. Obtaining lignin nanoparticles by sonication. *Ultrason. Sonochem.* **23**, 369–375 (2015).
86. Kim, S., *et al.* Chitosan-lignosulfonates sono-chemically prepared nanoparticles: Characterisation and potential applications. *Colloids Surf. B Biointerfaces* **103**, 1–8 (2013).
87. Wang, B., Sun, D., Wang, H. M., Yuan, T. Q. & Sun, R. C. Green and facile preparation of regular lignin nanoparticles with high yield and their natural broad-spectrum sunscreens. *ACS Sustain. Chem. Eng.* **7**, 2658–2666 (2019).
88. Liu, X., *et al*. Functionalization of lignin through ATRP grafting of poly(2-dimethylaminoethyl methacrylate) for gene delivery. *Colloids Surf. B Biointerfaces* **125**, 230–237 (2015).
89. Kai, D., *et al.* Engineering highly stretchable lignin-based electrospun nanofibers for potential biomedical applications. *J. Mater. Chem. B* **3**, 6194–6204 (2015).
90. Kai, D., *et al.* Sustainable and antioxidant lignin–polyester copolymers and nanofibers for potential healthcare applications. *ACS Sustain. Chem. Eng.* **5**, 6016–6025 (2017).
91. Kai, D., *et al.* Engineering poly(lactide)–lignin nanofibers with antioxidant activity for biomedical application. *ACS Sustain. Chem. Eng.* **4**, 5268–5276 (2016).
92. Meng, Y., *et al*. Lignin-based hydrogels: A review of preparation, properties, and application. *Int. J. Biol. Macromol.* **135**, 1006–1019 (2019).
93. Hoffman, A. S. Hydrogels for biomedical applications. *Advanced Drug Delivery Reviews* **64**, 18–23 (2012).
94. Kopeček, J. Hydrogel biomaterials: A smart future? *Biomaterials* **28**, 5185–5192 (2007).
95. Mohammadinejad, R. *et al.* Status and future scope of plant-based green hydrogels in biomedical engineering. *Appl. Mater. Today* **16**, 213–246 (2019).
96. Ciolacu, D., *et al*. New cellulose-lignin hydrogels and their application in controlled release of polyphenols. *Mater. Sci. Eng. C* **32**, 452–463 (2012).
97. Wang, X., *et al.* Ultrasonic-assisted synthesis of sodium lignosulfonate-grafted poly(acrylic acid-: Co -poly(vinyl pyrrolidone)) hydrogel for drug delivery. *RSC Adv.* **6**, 35550–35558 (2016).
98. Diao, B., *et al*. Biomass-based thermogelling copolymers consisting of lignin and grafted poly(N-isopropylacrylamide), poly(ethylene glycol), and poly(propylene glycol). *RSC Adv.* **4**, 42996–43003 (2014).
99. Zhang, X., *et al*. Controlled preparation of corncob lignin nanoparticles and their size-dependent antioxidant properties: Toward high value utilization of lignin. *ACS Sustain. Chem. Eng.* **7**, 17166–17174 (2019).
100. Ju, T., *et al*. Continuous production of lignin nanoparticles using a microchannel reactor and its application in UV-shielding films. *RSC Adv.* **9**, 24915–24921 (2019).
101. Li, S. X., *et al.* Preparation of organic acid lignin submicrometer particle as a natural broad-spectrum photo-protection agent. *Int. J. Biol. Macromol.* **132**, 836–843 (2019).
102. Richter, A. P., *et al.* An environmentally benign antimicrobial nanoparticle based on a silver-infused lignin core. *Nat. Nanotechnol.* **10**, 817–823 (2015).
103. Sipponen, M. H., *et al*. All-lignin approach to prepare cationic colloidal lignin particles: stabilization of durable Pickering emulsions. *Green Chem.* **19**, 5831–5840 (2017).
104. Qian, Y., *et al*. CO2-responsive diethylaminoethyl-modified lignin nanoparticles and their application as

surfactants for CO2/N2-switchable Pickering emulsions. *Green Chem.* **16**, 4963–4968 (2014).
105. Dai, L., *et al*. Lignin nanoparticle as a novel green carrier for the efficient delivery of resveratrol. *ACS Sustain. Chem. Eng.* **5**, 8241–8249 (2017).
106. Zhou, Y., *et al.* Preparation of targeted lignin–based hollow nanoparticles for the delivery of doxorubicin. *Nanomaterials* **9**, 188 (2019).
107. Alqahtani, M. S., *et al*. Novel lignin nanoparticles for oral drug delivery. *J. Mater. Chem. B* **7**, 4461–4473 (2019).
108. Ten, E. *et al.,* Lignin nanotubes as vehicles for gene delivery into human cells. *Biomacromolecules* **15**, 327–338 (2014).
109. Salami, M. A., *et al.* Electrospun polycaprolactone/lignin-based nanocomposite as a novel tissue scaffold for biomedical applications. *J. Med. Signals Sens.* **7**, 228–238 (2017).
110. Quraishi, S. *et al.* Novel non-cytotoxic alginate–lignin hybrid aerogels as scaffolds for tissue engineering. *J. Supercrit. Fluids* **105**, 1–8 (2015).
111. Espinoza-Acosta, J., *et al*. Antioxidant, antimicrobial, and antimutagenic properties of technical lignins and their applications. *BioResources* **11**, 5452–5481 (2016).
112. Gülçin, İ. Antioxidant activity of food constituents: an overview. *Arch. Toxicol.* **86**, 345–391 (2012).
113. Sindhi, V. *et al.* Potential applications of antioxidants – A review. *J. Pharm. Res.* **7**, 828–835 (2013).
114. Dizhbite, T., *et al*. Characterization of the radical scavenging activity of lignins - Natural antioxidants. *Bioresour. Technol.* **95**, 309–317 (2004).
115. Arshanitsa, A., *et al.* Fractionation of technical lignins as a tool for improvement of their antioxidant properties. in *Journal of Analytical and Applied Pyrolysis* **103**, 78–85 (Elsevier B.V., 2013).
116. Buranov, A. U., Ross, K. A. & Mazza, G. Isolation and characterization of lignins extracted from flax shives using pressurized aqueous ethanol. *Bioresour. Technol.* **101**, 7446–7455 (2010).
117. Lee, E., Song, Y. & Lee, S. Crosslinking of lignin/poly(vinyl alcohol) nanocomposite fiber webs and their antimicrobial and ultraviolet-protective properties. *Text. Res. J.* **89**, 3–12 (2019).
118. Barsberg, S., Elder, T. & Felby, C. Lignin−quinone interactions: Implications for optical properties of lignin. *Chem. Mater.* **15**, 649–655 (2003).
119. Zimniewska, M., *et al.* Functionalization of natural fibres textiles by improvement of nanoparticles fixation on their surface. *J. Fiber Bioeng. Informatics* **5**, 321–339 (2012).
120. Qian, Y., Qiu, X. & Zhu, S. Lignin: A nature-inspired sun blocker for broadspectrum Sunscreens. *Green Chem.* **17**, 320–324 (2015).
121. Zemek, J., *et al*. Antibiotic properties of lignin components. *Folia Microbiol. (Praha).* **24**, 483–486 (1979).
122. Dong, X., *et al.* Antimicrobial and antioxidant activities of lignin from residue of corn stover to ethanol production. *Ind. Crops Prod.* **34**, 1629–1634 (2011).
123. Colman, B. P., *et al.* Low Concentrations of silver nanoparticles in biosolids cause adverse ecosystem responses under realistic field scenario. *PLoS One* **8**, e57189 (2013).
124. Yang, Y., *et al.* An overview of pickering emulsions: Solid-particle materials, classification, morphology, and applications. *Front. Pharmacol.* **8**, 287 (2017).
125. Monégier du Sorbier, Q., Aimable, A. & Pagnoux, C. Influence of the electrostatic interactions in a Pickering emulsion polymerization for the synthesis of silica-polystyrene hybrid nanoparticles. *J. Colloid Interface Sci.* **448**, 306–314 (2015).
126. Bai, L., *et al.* Adsorption and assembly of cellulosic and lignin colloids at oil/water interfaces. *Langmuir* **35**, 571–588 (2019).
127. Dai, L., *et al.* Lignin-based nanoparticles stabilized Pickering emulsion for stability improvement and thermal-controlled release of *trans*-resveratrol. *ACS Sustain. Chem. Eng.* **7**, 13497–13504 (2019).
128. Witzler, M., *et al.* Lignin-derived biomaterials for drug release and tissue engineering. *Molecules* **23**, (2018).
129. Sipponen, M. H., *et al*. Lignin for nano- and microscaled carrier systems: Applications, trends, and challenges. *ChemSusChem* **12**, 2039–2054 (2019).
130. Mitra, A. K., *et al.* Novel delivery approaches for cancer therapeutics. *J. Control. Release* **219**, 248–268 (2015).
131. Piktel, E., *et al.* Recent insights in nanotechnology-based drugs and formulations designed for effective anti-cancer therapy. *J. Nanobiotechnol.* **14**, 39 (2016).
132. Shewach, D. S. & Kuchta, R. D. Introduction to cancer chemotherapeutics. *Chem. Rev.* **109**, 2859–2861 (2009).
133. Hanahan, D. & Weinberg, R. A. Hallmarks of cancer: the next generation. *Cell* **144**, 646–674 (2011).
134. Zhang, R. X., *et al*. Nanomedicine of synergistic drug combinations for cancer therapy - Strategies and perspectives. *J. Control. Release* **240**, 489–503 (2016).
135. Figueiredo, P., *et al*. Chapter 1 - The Emerging Role of Multifunctional Theranostic Materials in Cancer Nanomedicine. in *Handbook of Nanomaterials for Cancer Theranostics* (ed. Conde, J.) 1–31 (Elsevier, 2018).
136. Choi, K. Y., *et al*. Theranostic nanoplatforms for simultaneous cancer imaging and therapy: current approaches and future perspectives. *Nanoscale* **4**, 330–342 (2012).
137. Sumer, B. & Gao, J. Theranostic nanomedicine for cancer. *Nanomedicine (Lond.)* **3**, 137–140 (2008).
138. Anselmo, A. C. & Mitragotri, S. Nanoparticles in the clinic. *Bioeng. Transl. Med.* **1**, 10–29 (2016).
139. Anselmo, A. C. & Mitragotri, S. Nanoparticles in the clinic: An update. *Bioeng. Transl. Med.* **4**, (2019).
140. Ernsting, M. J., *et al*. Factors controlling the pharmacokinetics, biodistribution and intratumoral penetration of nanoparticles. *J. Control. Release* **172**, 782–794 (2013).

141. Bertrand, N. & Leroux, J.-C. The journey of a drug-carrier in the body: An anatomo-physiological perspective. *J. Control. Release* **161**, 152–163 (2012).
142. Lammers, T., *et al*. Drug targeting to tumors: Principles, pitfalls and (pre-) clinical progress. *J. Control. Release* **161**, 175–187 (2012).
143. Mahon, E., *et al*. Designing the nanoparticle–biomolecule interface for “targeting and therapeutic delivery”. *J. Control. Release* **161**, 164–174 (2012).
144. Nichols, J. W. & Bae, Y. H. Odyssey of a cancer nanoparticle: from injection site to site of action. *Nano Today* **7**, 606–618 (2012).
145. Rosenblum, D., *et al*. Progress and challenges towards targeted delivery of cancer therapeutics. *Nat. Commun.* **9**, 1410 (2018).
146. Garrastazu Pereira, G., *et al*. Loco-regional administration of nanomedicines for the treatment of lung cancer. *Drug Deliv.* **23**, 2881–2896 (2016).
147. Goins, B., Phillips, W. T. & Bao, A. Strategies for improving the intratumoral distribution of liposomal drugs in cancer therapy. *Expert Opin. Drug Deliv.* **13**, 873–889 (2016).
148. Xie, H., *et al*. Effect of intratumoral administration on biodistribution of 64Cu-labeled nanoshells. *Int. J. Nanomedicine* **7**, 2227–2238 (2012).
149. Maeda, H. Toward a full understanding of the EPR effect in primary and metastatic tumors as well as issues related to its heterogeneity. *Adv. Drug Deliv. Rev.* **91**, 3–6 (2015).
150. Hare, J. I., *et al.* Challenges and strategies in anti-cancer nanomedicine development: An industry perspective. *Adv. Drug Deliv. Rev.* **108**, 25–38 (2017).
151. Dakwar, G. R., *et al.* Nanomedicine-based intraperitoneal therapy for the treatment of peritoneal carcinomatosis — Mission possible? *Adv. Drug Deliv. Rev.* **108**, 13–24 (2017).
152. McMullen, J. R. W., *et al*. Peritoneal carcinomatosis: limits of diagnosis and the case for liquid biopsy. *Oncotarget* **8**, 43481–43490 (2017).
153. Chen, Z., *et al.* Cancer cell membrane-biomimetic nanoparticles for homologous-targeting dual-modal imaging and photothermal therapy. *ACS Nano* **10**, 10049–10057 (2016).
154. Sun, X., *et al*. Remotely controlled red blood cell carriers for cancer targeting and near-infrared light-triggered drug release in combined photothermal–chemotherapy. *Adv. Funct. Mater.* **25**, 2386–2394 (2015).
155. Fontana, F., *et al.* Production of pure drug nanocrystals and nano co-crystals by confinement methods. *Adv. Drug Deliv. Rev.* **131**, 3–21 (2018).
156. Blanco, E., Shen, H. & Ferrari, M. Principles of nanoparticle design for overcoming biological barriers to drug delivery. *Nat. Biotechnol.* **33**, 941–951 (2015).
157. Soo Choi, H., *et al.* Renal clearance of quantum dots. *Nat. Biotechnol.* **25**, 1165–1170 (2007).
158. Zhang, Y. N., *et al*. Nanoparticle–liver interactions: Cellular uptake and hepatobiliary elimination. *J. Control. Release* **240**, 332–348 (2016).
159. Jain, R. K. & Stylianopoulos, T. Delivering nanomedicine to solid tumors. *Nat. Rev. Clin. Oncol.* **7**, 653–664 (2010).
160. Petros, R. A. & Desimone, J. M. Strategies in the design of nanoparticles for therapeutic applications. *Nat. Rev. Drug Discov.* **9**, 615–627 (2010).
161. Zhao, J. & Stenzel, M. H. Entry of nanoparticles into cells: The importance of nanoparticle properties. *Polym. Chem.* **9**, 259–272 (2018).
162. Foroozandeh, P. & Aziz, A. A. Insight into cellular uptake and intracellular trafficking of nanoparticles. *Nanoscale Res. Lett.* **13**, (2018).
163. Kahraman, E., Güngör, S. & Özsoy, Y. Potential enhancement and targeting strategies of polymeric and lipid-based nanocarriers in dermal drug delivery. *Ther. Deliv.* **8**, 967–985 (2017).
164. Mahapatro, A. & Singh, D. K. Biodegradable nanoparticles are excellent vehicle for site directed in-vivo delivery of drugs and vaccines. *J. Nanobiotechnol.* **9**, 55 (2011).
165. Danhier, F., *et al.* PLGA-based nanoparticles: an overview of biomedical applications. *J. Control. Release* **161**, 505–522 (2012).
166. Sarcan, E. T., Silindir-Gunay, M. & Ozer, A. Y. Theranostic polymeric nanoparticles for NIR imaging and photodynamic therapy. *Int. J. Pharm.* **551**, 329–338 (2018).
167. Bolhassani, A., *et al.* Polymeric nanoparticles: potent vectors for vaccine delivery targeting cancer and infectious diseases. *Hum. Vaccin. Immunother.* **10**, 321–332 (2014).
168. Elsabahy, M. & Wooley, K. L. Design of polymeric nanoparticles for biomedical delivery applications. *Chem. Soc. Rev.* **41**, 2545–2561 (2012).
169. Xing, H., Hwang, K. & Lu, Y. Recent developments of liposomes as nanocarriers for theranostic applications. *Theranostics* **6**, 1336–1352 (2016).
170. Yue, X. & Dai, Z. Liposomal nanotechnology for cancer theranostics. *Curr. Med. Chem.* **25**, 1397–1408 (2018).
171. Yingchoncharoen, P., Kalinowski, D. S. & Richardson, D. R. Lipid-based drug delivery systems in cancer therapy: What is available and what is yet to come. *Pharmacol. Rev.* **68**, 701–787 (2016).
172. Miller, A. D. Lipid-based nanoparticles in cancer diagnosis and therapy . *J. Drug Deliv.* **2013**, 9 (2013).
173. Rahikkala, A., *et al.* Mesoporous silica nanoparticles for targeted and stimuli-responsive delivery of chemotherapeutics: A review. *Adv. Biosyst.* **2**, 1800020 (2018).
174. Li, W. *et al.* Tailoring porous silicon for biomedical applications: From drug delivery to cancer immunotherapy. *Adv. Mater.* **30**, 1703740 (2018).
175. Shahbazi, M. A., *et al.* The mechanisms of surface chemistry effects of mesoporous silicon nanoparticles

on immunotoxicity and biocompatibility. *Biomaterials* **34**, 7776–7789 (2013).
176. Shahbazi, M. A., *et al.* Surface chemistry dependent immunostimulative potential of porous silicon nanoplatforms. *Biomaterials* **35**, 9224–9235 (2014).
177. Santos, H. A., *et al.* Mesoporous materials as controlled drug delivery formulations. *J. Drug Deliv. Sci. Technol.* **21**, 139–155 (2011).
178. Almeida, J. P. M., Figueroa, E. R. & Drezek, R. A. Gold nanoparticle mediated cancer immunotherapy. *Nanomedicine: NBM* **10**, 503–514 (2014).
179. Almeida, J. P. M., *et al*. In vivo gold nanoparticle delivery of peptide vaccine induces anti-tumor immune response in prophylactic and therapeutic tumor models. *Small* **11**, 1453–1459 (2015).
180. Singh, P., *et al.* Gold nanoparticles in diagnostics and therapeutics for human cancer. *Int. J. Mol. Sci.* **19**, (2018).
181. Vallabani, N. V. S. & Singh, S. Recent advances and future prospects of iron oxide nanoparticles in biomedicine and diagnostics. *3 Biotech.* **8**, (2018).
182. Palanisamy, S. & Wang, Y. M. Superparamagnetic iron oxide nanoparticulate system: Synthesis, targeting, drug delivery and therapy in cancer. *Dalton Trans.* **48**, 9490–9515 (2019).
183. Dulińska-Litewka, J., *et al.* Superparamagnetic iron oxide nanoparticles-current and prospective medical applications. *Materials* **12**, (2019).
184. Singh, P., *et al.* Organic functionalisation and characterisation of single-walled carbon nanotubes. *Chem. Soc. Rev.* **38**, 2214–2230 (2009).
185. Georgakilas, V., *et al.* Functionalization of graphene: Covalent and non-covalent approach. *Chem. Rev.* **112**, 6156–6214 (2012).
186. Son, K. H., Hong, J. H. & Lee, J. W. Carbon nanotubes as cancer therapeutic carriers and mediators. *Int. J. Nanomed.* **11**, 5163–5185 (2016).
187. Fang, R. H., *et al.* Cancer cell membrane-coated nanoparticles for anticancer vaccination and drug delivery. *Nano Lett.* **14**, 2181–2188 (2014).
188. Cheung, A. S., *et al*. Adjuvant-loaded subcellular vesicles derived from disrupted cancer cells for cancer vaccination. *Small* **12**, 2321–2333 (2016).
189. Fontana, F., *et al.* Multistaged nanovaccines based on porous silicon@acetalated dextran@cancer cell membrane for cancer immunotherapy. *Adv. Mater.* **29**, 1603239 (2017).
190. Fröhlich, E. The role of surface charge in cellular uptake and cytotoxicity of medical nanoparticles. *Int. J. Nanomed.* **7**, 5577–5591 (2012).
191. Nel, A. E., *et al.* Understanding biophysicochemical interactions at the nano-bio interface. *Nat. Mater.* **8**, 543–557 (2009).
192. Champion, J. A. & Mitragotri, S. Role of target geometry in phagocytosis. *Proc. Natl. Acad. Sci. U.S.A.* **103**, 4930–4934 (2006).
193. Toy, R., *et al*. Shaping cancer nanomedicine: The effect of particle shape on the in vivo journey of nanoparticles. *Nanomedicine* **9**, 121–134 (2014).
194. Gentile, F., *et al.* The effect of shape on the margination dynamics of non-neutrally buoyant particles in two-dimensional shear flows. *J. Biomech.* **41**, 2312–2318 (2008).
195. Huang, X., *et al*. The effect of the shape of mesoporous silica nanoparticles on cellular uptake and cell function. *Biomaterials* **31**, 438–448 (2010).
196. Chen, H., Langer, R. & Edwards, D. A. A film tension theory of phagocytosis. *J. Colloid Interface Sci.* **190**, 118–133 (1997).
197. Gustafson, H. H., *et al*. Nanoparticle uptake: The phagocyte problem. *Nano Today* **10**, 487–510 (2015).
198. Jokerst, J. V., *et al*. Nanoparticle PEGylation for imaging and therapy. *Nanomedicine* **6**, 715–728 (2011).
199. Guo, P., *et al.* Nanoparticle elasticity directs tumor uptake. *Nat. Commun.* **9**, (2018).
200. Zhang, L., *et al.* Microfluidic synthesis of hybrid nanoparticles with controlled lipid layers: Understanding flexibility-regulated cell–nanoparticle interaction. *ACS Nano* **9**, 9912–9921 (2015).
201. Banquy, X., *et al.* Effect of mechanical properties of hydrogel nanoparticles on macrophage cell uptake. *Soft. Matter.* **5**, 3984–3991 (2009).
202. Wang, S., Huang, P. & Chen, X. Stimuli-responsive programmed specific targeting in nanomedicine. *ACS Nano* **10**, 2991–2994 (2016).
203. Danhier, F., Feron, O. & Préat, V. To exploit the tumor microenvironment: Passive and active tumor targeting of nanocarriers for anti-cancer drug delivery. *J. Control. Release* **148**, 135–146 (2010).
204. Cagliani, R., Gatto, F. & Bardi, G. Protein adsorption: A feasible method for nanoparticle functionalization? *Materials* **12**, (2019).
205. Cedervall, T., *et al.* Understanding the nanoparticle-protein corona using methods to quntify exchange rates and affinities of proteins for nanoparticles. *Proc. Natl. Acad. Sci. U.S.A.* **104**, 2050–2055 (2007).
206. Bangham, A. D., Pethica, B. A. & Seaman, G. V. The charged groups at the interface of some blood cells. *Biochem. J.* **69**, 12–19 (1958).
207. Vroman, L. Effect of adsorbed proteins on the wettability of hydrophilic and hydrophobic solids. *Nature* **196**, 476–477 (1962).
208. Hadjidemetriou, M. & Kostarelos, K. Evolution of the nanoparticle corona. *Nat. Nanotechnol.* **12**, 288–290 (2017).
209. Milani, S., *et al*. Reversible versus irreversible binding of transferrin to polystyrene nanoparticles: Soft and hard corona. *ACS Nano* **6**, 2532–2541 (2012).
210. Barui, A. K., *et al*. Cancer-targeted nanomedicine: Overcoming the barrier of the protein corona. *Adv. Ther.*

1900124 (2019).
211. Owens, D. E. & Peppas, N. A. Opsonization, biodistribution, and pharmacokinetics of polymeric nanoparticles. *Int. J. Pharm.* **307**, 93–102 (2006).
212. Vu, V. P., *et al.* Immunoglobulin deposition on biomolecule corona determines complement opsonization efficiency of preclinical and clinical nanoparticles. *Nat. Nanotechnol.* **14**, 260–268 (2019).
213. Absolom, D. R. [13] Opsonins and dysopsonins: An overview. *Methods Enzymol.* **132**, 281–318 (1986).
214. Nguyen, V. H. & Lee, B. J. Protein corona: A new approach for nanomedicine design. *Int. J. Nanomed.* **12**, 3137–3151 (2017).
215. Gref, R., *et al.* The controlled intravenous delivery of drugs using PEG-coated sterically stabilized nanospheres. *Adv. Drug Deliv. Rev.* **64**, 316–326 (2012).
216. Gaucher, G., *et al*. Effect of poly(*N*-vinyl-pyrrolidone)-block-poly(D,L-lactide) as coating agent on the opsonization, phagocytosis, and pharmacokinetics of biodegradable nanoparticles. *Biomacromolecules* **10**, 408–416 (2009).
217. Schöttler, S., *et al.* Protein adsorption is required for stealth effect of poly(ethylene glycol)- and poly(phosphoester)-coated nanocarriers. *Nat. Nanotechnol.* **11**, 372–377 (2016).
218. Butcher, N. J., Mortimer, G. M. & Minchin, R. F. Drug delivery: Unravelling the stealth effect. *Nat. Nanotechnol.* **11**, 310–311 (2016).
219. Suk, J. S., *et al*. PEGylation as a strategy for improving nanoparticle-based drug and gene delivery. *Adv. Drug Deliv. Rev.* **99**, 28–51 (2016).
220. Miteva, M., *et al.* Tuning PEGylation of mixed micelles to overcome intracellular and systemic siRNA delivery barriers. *Biomaterials* **38**, 97–107 (2015).
221. Gref, R., *et al.* 'Stealth' corona-core nanoparticles surface modified by polyethylene glycol (PEG): Influences of the corona (PEG chain length and surface density) and of the core composition on phagocytic uptake and plasma protein adsorption. *Colloids Surfaces B* **18**, 301–313 (2000).
222. Riley, R. S., *et al*. Delivery technologies for cancer immunotherapy. *Nat. Rev. Drug Discov.* **18**, 175–196 (2019).
223. Matsumura, Y. & Maeda, H. A New concept for macromolecular therapeutics in cancer chemotherapy: Mechanism of tumoritropic accumulation of proteins and the antitumor agent smancs. *Cancer Res.* **46**, 6387–6392 (1986).
224. Golombek, S. K., *et al.* Tumor targeting via EPR: Strategies to enhance patient responses. *Adv. Drug Deliv. Rev.* **130**, 17–38 (2018).
225. Iyer, A. K., *et al*. Exploiting the enhanced permeability and retention effect for tumor targeting. *Drug Discov. Today* **11**, 812–818 (2006).
226. Prabhakar, U., *et al.* Challenges and key considerations of the enhanced permeability and retention effect for nanomedicine drug delivery in oncology. *Cancer Res.* **73**, 2412–2417 (2013).
227. Nakamura, Y., *et al*. Nanodrug delivery: Is the enhanced permeability and retention effect sufficient for curing cancer? *Bioconjug. Chem.* **27**, 2225–2238 (2016).
228. Mout, R., *et al*. Surface functionalization of nanoparticles for nanomedicine. *Chem.l Soc. Rev.* **41**, 2539–2544 (2012).
229. Weissleder, R., *et al*. Cell-specific targeting of nanoparticles by multivalent attachment of small molecules. *Nat. Biotechnol.* **23**, 1418–1423 (2005).
230. Navya, P. N., *et al.* Current trends and challenges in cancer management and therapy using designer nanomaterials. *Nano Converg.* **6**, (2019).
231. Ruoslahti, E. Peptides as targeting elements and tissue penetration devices for nanoparticles. *Adv. Mater.* **24**, 3747–3756 (2012).
232. Friedman, A., Claypool, S. & Liu, R. The smart targeting of nanoparticles. *Curr. Pharm. Des.* **19**, 6315–6329 (2013).
233. Deutscher, S. L. Phage display in molecular imaging and diagnosis of cancer. *Chem. Rev.* **110**, 3196–3211 (2010).
234. Saw, P. E. & Song, E. W. Phage display screening of therapeutic peptide for cancer targeting and therapy. *Protein Cell* **10**, 787–807 (2019).
235. Ruoslahti, E., Bhatia, S. N. & Sailor, M. J. Targeting of drugs and nanoparticles to tumors. *J. Cell Biol.* **188**, 759–768 (2010).
236. Wu, C. H., *et al*. Advancement and applications of peptide phage display technology in biomedical science. *J. Biomed. Sci.* **23**, (2016).
237. Teesalu, T., Sugahara, K. N. & Ruoslahti, E. Tumor-penetrating peptides. *Front. Oncol.* **3**, (2013).
238. Werle, M. & Bernkop-Schnürch, A. Strategies to improve plasma half life time of peptide and protein drugs. *Amino Acids* **30**, 351–367 (2006).
239. Figueiredo, P., *et al.* Angiopep2-functionalized polymersomes for targeted doxorubicin delivery to glioblastoma cells. *Int. J. Pharm.* **511**, 794–803 (2016).
240. Wannasarit, S., *et al.* A virus-mimicking pH-responsive acetalated dextran-based membrane-active polymeric nanoparticle for intracellular delivery of antitumor therapeutics. *Adv. Funct. Mater.* **29**, 1905352 (2019).
241. Alkilany, A. M., *et al.* Ligand density on nanoparticles: A parameter with critical impact on nanomedicine. *Adv. Drug Deliv. Rev.* **143**, 22–36 (2019).
242. Yu, J., Chu, X. & Hou, Y. Stimuli-responsive cancer therapy based on nanoparticles. *Chem. Commun.* **50**, 11614–11630 (2014).

243. Mura, S., Nicolas, J. & Couvreur, P. Stimuli-responsive nanocarriers for drug delivery. *Nat. Mater.* **12**, 991–1003 (2013).
244. Li, L., Yang, W. W. & Xu, D. G. Stimuli-responsive nanoscale drug delivery systems for cancer therapy. *J. Drug Target.* **27**, 423–433 (2019).
245. Du, J., Lane, L. A. & Nie, S. Stimuli-responsive nanoparticles for targeting the tumor microenvironment. *J. Control. Release* **219**, 205–214 (2015).
246. Herranz-Blanco, B., *et al.* pH-Switch nanoprecipitation of polymeric nanoparticles for multimodal cancer targeting and intracellular triggered delivery of doxorubicin. *Adv. Healthc. Mater.* **5**, 1904–1916 (2016).
247. Kocak, G., Tuncer, C. & Bütün, V. pH-Responsive polymers. *Polym. Chem.* **8**, 144–176 (2017).
248. Shahbazi, M. A., *et al.* Intracellular responsive dual delivery by endosomolytic polyplexes carrying DNA anchored porous silicon nanoparticles. *J. Control. Release* **249**, 111–122 (2017).
249. Coll, C., *et al.* Enzyme-mediated controlled release systems by anchoring peptide sequences on mesoporous silica supports. *Angew. Chemie Int. Ed.* **50**, 2138–2140 (2011).
250. Harris, T. J., *et al.* Protease-triggered unveiling of bioactive nanoparticles. *Small* **4**, 1307–1312 (2008).
251. Sánchez-Moreno, P., *et al*. Thermo-sensitive nanomaterials: Recent advance in synthesis and biomedical applications. *Nanomaterials* **8**, (2018).
252. Li, X. & Su, X. Multifunctional smart hydrogels: Potential in tissue engineering and cancer therapy. *J. Mater. Chem. B* **6**, 4714–4730 (2018).
253. Estelrich, J., *et al*. Iron oxide nanoparticles for magnetically-guided and magnetically-responsive drug delivery. *Int. J. Mol. Sci.* **16**, 8070–8101 (2015).
254. Kralj, S., *et al*. Design and fabrication of magnetically responsive nanocarriers for drug delivery. *Curr. Med. Chem.* **24**, 454–469 (2016).
255. Ji, J., *et al.* Light-activatable assembled nanoparticles to improve tumor penetration and eradicate metastasis in triple negative breast cancer. *Adv. Funct. Mater.* **28**, 1801738 (2018).
256. Lou, J., Zhang, L. & Zheng, G. Advancing cancer immunotherapies with nanotechnology. *Adv. Ther.* **2**, 1800128 (2019).
257. Fontana, F., *et al*. Immunostimulation and immunosuppression: Nanotechnology on the brink. *Small Methods* **2**, 1700347 (2018).
258. Fontana, F., Liu, D., Hirvonen, J. & Santos, H. A. Delivery of therapeutics with nanoparticles: what's new in cancer immunotherapy? *Wiley Interdiscip. Rev. Nanomed. Nanobiotechnol.* **9**, e1421 (2017).
259. Goldberg, M. S. Improving cancer immunotherapy through nanotechnology. *Nat. Rev. Cancer* **19**, 587–602 (2019).
260. Bauleth-Ramos, T., *et al.* Nutlin-3a and cytokine co-loaded spermine-modified acetalated dextran nanoparticles for cancer chemo-immunotherapy. *Adv. Funct. Mater.* **27**, 1703303 (2017).
261. Fusciello, M., *et al.* Artificially cloaked viral nanovaccine for cancer immunotherapy. *Nat. Commun.* **10**, 5747 (2019).
262. McAllister, S. S. & Weinberg, R. A. The tumour-induced systemic environment as a critical regulator of cancer progression and metastasis. *Nat. Cell Biol.* **16**, 717–727 (2014).
263. Poh, A. R. & Ernst, M. Targeting macrophages in cancer: From bench to bedside. *Front.Oncol.* **8**, (2018).
264. Franklin, R. A., *et al.* The cellular and molecular origin of tumor-associated macrophages. *Science* **344**, 921–925 (2014).
265. Guerriero, J. L. Macrophages: The road less traveled, changing anticancer therapy. *Trends Mol. Med.* **24**, 472–489 (2018).
266. Mantovani, A., *et al*. Tumour-associated macrophages as treatment targets in oncology. *Nat. Rev. Clin. Oncol.* **14**, 399–416 (2017).
267. DeNardo, D. G. & Ruffell, B. Macrophages as regulators of tumour immunity and immunotherapy. *Nat. Rev. Immunol.* **19**, 369–382 (2019).
268. Murray, P. J., *et al.* Macrophage activation and polarization: Nomenclature and experimental guidelines. *Immunity* **41**, 14–20 (2014).
269. Allavena, P., *et al*. The inflammatory micro-environment in tumor progression: The role of tumor-associated macrophages. *Crit. Rev. Oncol. Hematol.* **66**, 1–9 (2008).
270. Chen, Y., *et al.* Tumor-associated macrophages: An accomplice in solid tumor progression. *J. Biomed. Sci.* **26**, (2019).
271. Zheng, X., *et al.* Redirecting tumor-associated macrophages to become tumoricidal effectors as a novel strategy for cancer therapy. *Oncotarget* **8**, 48436–48452 (2017).
272. Yang, L. & Zhang, Y. Tumor-associated macrophages, potential targets for cancer treatment. *Biomark. Res.* **5**, (2017).
273. He, W., *et al*. Drug delivery to macrophages: A review of targeting drugs and drug carriers to macrophages for inflammatory diseases. *Adv. Drug Deliv. Rev.* (2019).
274. Jeong, J., Suh, Y. & Jung, K. Context drives diversification of monocytes and neutrophils in orchestrating the tumor microenvironment. *Front. Immunol.* **10**, 1817 (2019).
275. Ries, C. H., *et al.* Targeting tumor-associated macrophages with anti-CSF-1R antibody reveals a strategy for cancer therapy. *Cancer Cell* **25**, 846–859 (2014).
276. Pyonteck, S. M., *et al.* CSF-1R inhibition alters macrophage polarization and blocks glioma progression. *Nat. Med.* **19**, 1264–1272 (2013).
277. Qian, B. Z., *et al.* CCL2 recruits inflammatory monocytes to facilitate breast-tumour metastasis. *Nature* **475**, 222–225 (2011).

278. Shahbazi, M.-A., *et al.* Targeted reinforcement of macrophage reprogramming toward M2 polarization by IL-4-loaded hyaluronic acid particles. *ACS Omega* **3**, 18444–18455 (2018).
279. Ovais, M., Guo, M. & Chen, C. Tailoring nanomaterials for targeting tumor-associated macrophages. *Adv. Mater.* **31**, 1808303 (2019).
280. Si, J., *et al*. Macrophages as active nanocarriers for targeted early and adjuvant cancer chemotherapy. *Small* **12**, 5108–5119 (2016).
281. Loberg, R. D., *et al.* Targeting CCL2 with systemic delivery of neutralizing antibodies induces prostate cancer tumor regression in vivo. *Cancer Res.* **67**, 9417–9424 (2007).
282. Nywening, T. M., *et al.* Targeting tumour-associated macrophages with CCR2 inhibition in combination with FOLFIRINOX in patients with borderline resectable and locally advanced pancreatic cancer: A single-centre, open-label, dose-finding, non-randomised, phase 1b trial. *Lancet Oncol.* **17**, 651–662 (2016).
283. Zhan, X., *et al.* Targeted depletion of tumour-associated macrophages by an alendronate-glucomannan conjugate for cancer immunotherapy. *Biomaterials* **35**, 10046–10057 (2014).
284. Germano, G., *et al.* Role of macrophage targeting in the antitumor activity of trabectedin. *Cancer Cell* **23**, 249–262 (2013).
285. Papadopoulos, K. P., *et al.* First-in-human study of AMG 820, a monoclonal anti-colony-stimulating factor 1 receptor antibody, in patients with advanced solid tumors. *Clin. Cancer Res.* **23**, 5703–5710 (2017).
286. Von Tresckow, B., *et al.* An open-label, multicenter, phase I/II study of JNJ-40346527, a CSF-1R inhibitor, in patients with relapsed or refractory Hodgkin lymphoma. *Clin. Cancer Res.* **21**, 1843–1850 (2015).
287. Gholamin, S., *et al.* Disrupting the CD47-SIRPα anti-phagocytic axis by a humanized anti-CD47 antibody is an efficacious treatment for malignant pediatric brain tumors. *Sci. Transl. Med.* **9**, (2017).
288. Georgoudaki, A. M., *et al.* Reprogramming tumor-associated macrophages by antibody targeting inhibits cancer progression and metastasis. *Cell Rep.* **15**, 2000–2011 (2016).
289. Vonderheide, R. H., *et al.* Clinical activity and immune modulation in cancer patients treated with CP-870,893, a novel CD40 agonist monoclonal antibody. *J. Clin. Oncol.* **25**, 876–883 (2007).
290. Rodell, C. B., *et al.* TLR7/8-agonist-loaded nanoparticles promote the polarization of tumour-associated macrophages to enhance cancer immunotherapy. *Nat. Biomed. Eng.* **2**, 578–588 (2018).
291. Smith, D. A., *et al.* Antitumor activity and safety of combination therapy with the Toll-like receptor 9 agonist IMO-2055, erlotinib, and bevacizumab in advanced or metastatic non-small cell lung cancer patients who have progressed following chemotherapy. *Cancer Immunol. Immunother.* **63**, 787–796 (2014).
292. Yang, Q. & Pan, X. Correlation between lignin physicochemical properties and inhibition to enzymatic hydrolysis of cellulose. *Biotechnol. Bioeng.* **113**, 1213–1224 (2016).
293. Almeida, P. V., *et al.* Amine-modified hyaluronic acid-functionalized porous silicon nanoparticles for targeting breast cancer tumors. *Nanoscale* **6**, 10377–10387 (2014).
294. Shrestha, N., *et al.* Chitosan-modified porous silicon microparticles for enhanced permeability of insulin across intestinal cell monolayers. *Biomaterials* **35**, 7172–7179 (2014).
295. Ying, W., *et al*. Investigation of macrophage polarization using bone marrow derived macrophages. *J. Vis. Exp.* **76**, e50323 (2013).
296. Corporation, P. *RealTime-Glo™ MT Cell Viability Assay Instructions for Use of Products G9711, G9712 and G9713*.
297. Aslan, B., *et al*. Nanotechnology in cancer therapy. *J. Drug Target.* **21**, 904–913 (2013).
298. Gaumet, M., *et al*. Nanoparticles for drug delivery: The need for precision in reporting particle size parameters. *Eur. J. Pharm. Biopharm.* **69**, 1–9 (2008).
299. Shete, P. B., *et al*. Water dispersible oleic acid-coated Fe_3O_4 nanoparticles for biomedical applications. *J. Magn. Magn. Mater.* **377**, 406–410 (2015).
300. Wahajuddin & Arora, S. Superparamagnetic iron oxide nanoparticles: Magnetic nanoplatforms as drug carriers. *Int. J. Nanomed.* **7**, 3445–3471 (2012).
301. Tang, X. L., *et al.* Paclitaxel modified Fe_3O_4 loaded albumin nanoparticles as drug delivery vehicles by self-assembly. *RSC Adv.* **6**, 43284–43292 (2016).
302. Kavaz, D., *et al*. Bleomycin loaded magnetic chitosan nanoparticles as multifunctional nanocarriers. *J. Bioact. Compat. Polym.* **25**, 305–318 (2010).
303. Kandasamy, G. & Maity, D. Recent advances in superparamagnetic iron oxide nanoparticles (SPIONs) for in vitro and in vivo cancer nanotheranostics. *Int. J. Pharm.* **496**, 191–218 (2015).
304. Albanese, A., Tang, P. S. & Chan, W. C. W. The effect of nanoparticle size, shape, and surface chemistry on biological systems. *Annu. Rev. Biomed. Eng.* **14**, 1–16 (2012).
305. Milla, P., Dosio, F. & Cattel, L. PEGylation of proteins and liposomes: a powerful and flexible strategy to improve the drug delivery. *Curr. Drug Metab.* **13**, 105–119 (2012).
306. Verma, A. & Stellacci, F. Effect of surface properties on nanoparticle-cell interactions. *Small* **6**, 12–21 (2010).
307. Santos, H. A. *et al.* In vitro cytotoxicity of porous silicon microparticles: Effect of the particle concentration, surface chemistry and size. *Acta Biomater.* **6**, 2721–2731 (2010).
308. Manke, A., Wang, L. & Rojanasakul, Y. Mechanisms of nanoparticle-induced oxidative stress and toxicity. *BioMed Res. Int.* **2013**, 942916 (2013).
309. Wu, H., *et al*. Reactive oxygen species-related activities of nano-iron metal and nano-iron oxides. *J. Food Drug Anal.* **22**, 86–94 (2014).
310. Huang, G., *et al.* Superparamagnetic iron oxide nanoparticles: Amplifying ROS stress to improve anticancer drug efficacy. *Theranostics* **3**, 116–126 (2013).
311. Khanna, P., *et al*. Nanotoxicity: An interplay of oxidative stress, inflammation and cell death. *Nanomaterials*

5, 1163–1180 (2015).
312. Fu, P. P., *et al*. Mechanisms of nanotoxicity: Generation of reactive oxygen species. *J. Food Drug Anal.* **22**, 64–75 (2014).
313. Bennet, D. & Kim, S. Polymer nanoparticles for smart drug delivery. in *Application of Nanotechnology in Drug Delivery* (InTech, 2014).
314. Liu, C., *et al*. Chemical modification of cellulose with succinic anhydride in ionic liquid with or without catalysts. in *Ionic Liquids: Applications and Perspectives* (InTech, 2011).
315. Lee, E. S., *et al*. Poly(L-histidine)-PEG block copolymer micelles and pH-induced destabilization. *J. Control. Release* **90**, 363–374 (2003).
316. Regberg, J., Srimanee, A. & Langel, Ü. Applications of cell-penetrating peptides for tumor targeting and future cancer therapies. *Pharmaceuticals* **5**, 991–1007 (2012).
317. Barth, A. Infrared spectroscopy of proteins. *Biochim. Biophys. Acta Bioenergetics* **1767**, 1073–1101 (2007).
318. Kumar, V., *et al*. Biofunctional magnetic nanotube probe for recognition and separation of specific bacteria from a mixed culture. *RSC Adv.* **3**, 14634–14641 (2013).
319. Nawrotek, K., *et al*. Chitosan-based hydrogel implants enriched with calcium ions intended for peripheral nervous tissue regeneration. *Carbohydr. Polym.* **136**, 764–771 (2016).
320. Kiriazis, A., *et al.* Tricyclic benzo[*cd*]azulenes selectively inhibit activities of Pim kinases andrestrict growth of Epstein-Barr Virus-transformed cells. *PLoS One* **8**, (2013).
321. Shah, N., *et al.* Potential roles for the PIM1 kinase in human cancer - A molecular and therapeutic appraisal. *Eur. J. Cancer* **44**, 2144–2151 (2008).
322. Brault, L., *et al.* Pim serine/threonine kinases in the pathogenesis and therapy of hematologic malignancies and solid cancers. *Haematologica* **95**, 1004–1015 (2010).
323. Justus, C. R., Dong, L. & Yang, L. V. Acidic tumor microenvironment and pH-sensing G protein-coupled receptors. *Front. Physiol.* **4**, 354 (2013).
324. Singh, R. & Lillard, J. W. Nanoparticle-based targeted drug delivery. *Exp. Mol. Pathol.* **86**, 215–223 (2009).
325. Ravindran, S., *et al*. Acidic domain in dentin phosphophoryn facilitates cellular uptake: implications in targeted protein delivery. *J. Biol. Chem.* **288**, 16098-109 (2013).
326. DeRuiter, J. *Principles of Drug Action*. (2005).
327. Zhu, M., *et al.* Physicochemical properties determine nanomaterial cellular uptake, transport, and fate. *Acc. Chem. Res.* **46**, 622–631 (2013).
328. Simón-Gracia, L., Hunt, H. & Teesalu, T. Peritoneal carcinomatosis targeting with tumor homing peptides. *Molecules* **23**, 1190 (2018).
329. Guarnieri, D., *et al*. Effect of silica nanoparticles with variable size and surface functionalization on human endothelial cell viability and angiogenic activity. *J. Nanoparticle Res.* **16**, 2229 (2014).
330. Behzadi, S., *et al.* Flat cell culturing surface may cause misinterpretation of cellular uptake of nanoparticles. *Adv. Biosyst.* **2**, 1800046 (2018).
331. Breslin, S. & O'Driscoll, L. Three-dimensional cell culture: the missing link in drug discovery. *Drug Discov. Today* **18**, 240–249 (2013).
332. Ravi, M., *et al*. 3D Cell culture systems: Advantages and applications. *J. Cell. Physiol.* **230**, 16–26 (2015).
333. Cho, E. C., Zhang, Q. & Xia, Y. The effect of sedimentation and diffusion on cellular uptake of gold nanoparticles. *Nat. Nanotechnol.* **6**, 385–391 (2011).
334. Sugahara, K. N., *et al.* Coadministration of a tumor-penetrating peptide enhances the efficacy of cancer drugs. *Science* **328**, 1031–1035 (2010).
335. Bianchini, G., *et al*. Triple-negative breast cancer: challenges and opportunities of a heterogeneous disease. *Nat. Rev. Clin. Oncol.* **13**, 674–690 (2016).
336. Yuan, Z. Y., *et al*. High infiltration of tumor-associated macrophages in triple-negative breast cancer is associated with a higher risk of distant metastasis. *Onco. Targets. Ther.* **7**, 1475–1480 (2014).
337. Campbell, M. J., *et al.* Proliferating macrophages associated with high grade, hormone receptor negative breast cancer and poor clinical outcome. *Breast Cancer Res. Treat.* **128**, 703–711 (2011).
338. Volodko, N., *et al.* Low infiltration of tumor-associated macrophages in high c-Myb-expressing breast tumors. *Sci. Rep.* **9**, 11634 (2019).
339. Malorni, L., *et al.* Clinical and biologic features of triple-negative breast cancers in a large cohort of patients with long-term follow-up. *Breast Cancer Res. Treat.* **136**, 795–804 (2012).
340. Scodeller, P., *et al.* Precision targeting of tumor macrophages with a CD206 binding peptide. *Sci. Rep.* **7**, 14655 (2017).
341. Asciutto, E. K., *et al.* Phage-display-derived peptide binds to human CD206 and modeling reveals a new binding site on the receptor. *J. Phys. Chem. B* **123**, 1973–1982 (2019).
342. Pellegrini, F. & Budman, D. R. Review: Tubulin function, action of antitubulin drugs, and new drug development. *Cancer Invest.* **23**, 264–273 (2005).
343. Roy, A., *et al*. A highly tumor-targeted nanoparticle of podophyllotoxin penetrated tumor core and regressed multidrug resistant tumors. *Biomaterials* **52**, 335–346 (2015).
344. Galstyan, A., *et al.* Blood–brain barrier permeable nano immunoconjugates induce local immune responses for glioma therapy. *Nat. Commun.* **10**, 3850 (2019).
345. Peranzoni, E., *et al.* Macrophages impede CD8 T cells from reaching tumor cells and limit the efficacy of anti–PD-1 treatment. *Proc. Natl. Acad. Sci. U.S.A.* **115**, E4041–E4050 (2018).
346. Cassetta, L. & Pollard, J. W. Targeting macrophages: therapeutic approaches in cancer. *Nat. Rev. Drug Discov.* **17**, 887–904 (2018).

347. Noy, R. & Pollard, J. W. Tumor-associated macrophages: From mechanisms to therapy. *Immunity* **41**, 49–61 (2014).
348. Gun, S. Y., *et al*. Targeting immune cells for cancer therapy. *Redox Biol.* **25**, (2019).
349. Pockros, P. J., *et al.* Oral resiquimod in chronic HCV infection: Safety and efficacy in 2 placebo-controlled, double-blind phase IIa studies. *J. Hepatol.* **47**, 174–182 (2007).